Search for CP violation with MORA : commissioning of the setups and first experiments

Sacha Daumas Tschopp

Normandie Université

UNIVERSITÉ CAEN NORMANDIE

THÈSE

Pour obtenir le diplôme de doctorat

Spécialité **PHYSIQUE**

Préparée au sein de l'**Université de Caen Normandie**

Search for CP violation with MORA: commissioning of the setups and first experiments

Présentée et soutenue par

SACHA DAUMAS TSCHOPP

Thèse soutenue le 14/12/2023

devant le jury composé de :

M. NATHAL SEVERIJNS	Professeur - LEUVEN - KATHOLIEKE UNIVERSITEIT	Rapporteur du jury
MME PAULINE ASCHER	Chargé de recherche - Centre d'Etudes Nucléaires de Bordeaux	Membre du jury
M. PIERRE DELAHAYE	Chargé de recherche HDR - 14 GANIL de CAEN	Membre du jury
M. LEENDERT HAYEN	Docteur - ENSICAEN	Membre du jury
M. BERTRAM BLANK	Directeur de recherche au CNRS - UNIVERSITE BORDEAUX 1 SCIENCES ET TECHNOLOGIE	Président du jury
M. ETIENNE LIENARD	Professeur des universités - Université de Caen Normandie	Directeur de thèse

Thèse dirigée par **ETIENNE LIENARD** (Laboratoire de physique corpusculaire (Caen))

ED 591 PSIME

lpc caen
laboratoire de physique corpusculaire

Contents

List of Figures

Remerciements

Aujourd'hui je suis arrivé au terme de ce long périple et c'est presque irréel de le voir s'achever. J'ai effectué tous mes stages au sein du LPC Caen et j'ai bien pris mes marques. Je redoute l'instant où il me faudra laisser ma place, près de la porte du bureau D17. Il y a beaucoup de personnes que j'aimerais remercier et je suis sûr que je vais en oublier dans le processus donc d'avance, pardon !

Tout d'abord, je tiens à remercier les personnes qui m'ont encadrées durant ma thèse que ce soit de près ou de loin. Je tiens à remercier mon directeur de thèse, Étienne, qui m'a toujours soutenu et, même au vue de ses responsabilités grandissantes, a toujours pris le temps de m'expliquer calmement et avec beaucoup de pédagogie des concepts qui m'étaient inconnus ou incompris. Je souhaite remercier également Gilles Quéméner qui m'a énormément accompagné dans le processus de rédaction et de soutenance. Ta porte était toujours ouverte et pour ton calme et ta gentillesse : Merci ! Enfin, je remercie Leendert Hayen qui, bien qu'arrivé dans une troisième année bien entamée, m'a également accompagné et a apporté la lumière sur pas mal de concepts du MS restés jusqu'à lors très obscurs. Je tiens à remercier également Pierre Delahaye qui, non seulement m'a fait l'honneur d'être dans mon jury de thèse mais avec lequel on a partagé plein de bons souvenirs entre les différentes réu d'analyses et les séjours à JYFL où on finissait complètement éreintés. Je tiens aussi à remercier Xavier qui m'a donné de très bons conseils sur les simu SIMION et les différentes analyses des données de MORA.

Je remercie, bien sûr, Nathal Severijns, Bertram Blank, Pauline Ascher, Pierre Delahaye, Leendert Hayen d'avoir non seulement participer à mon jury de thèse mais également d'avoir accepté de prendre le temps de lire mon manuscrit. Je les remercie également de leurs retours constructifs afin d'améliorer la qualité de ce dernier.

Je remercie également quelques doctorants et amis ici comme: Loïc, Vincent, Alexis, Marius, Erwan et Paul pour les bons moments passés ensemble ! Évidemment je ne pas ne pas mentionner le Docteur Tom Génard, mon éternel camarade de binôme avec qui on a traversé ensemble l'ombre et la flamme que représentait ce parcours universitaire. Merci infiniment de ton soutien au quotidien Tom !

Le LPC Caen a une ambiance unique et chaleureuse qui, je l'ai appris, ne semble étrangement pas être le cas des autres labos sur le campus 2 (cc le CRISMAT). Pour cela je tiens à remercier Gilles Ban et Étienne qui respectivement m'ont accueilli et ont su proposer des évènements renforçant la cohésion du labo. En parlant de cela, un merci à la "Dream Team"

pour l'organisation des différents BBQ et fameux repas de Noël ! Je remercie également Freddy avec qui j'ai partagé mon bureau pendant trois ans. Merci de m'avoir accueilli et nos discussions me manqueront !

MORA n'aurait sûrement pas vu le jour sans les efforts des équipes techniques du labo donc merci à vous, Christophe, Jérôme, Jean-François, Philippe et Yvan.

Enfin, je tiens à remercier plus spécialement ma famille et amis proches notamment les "bébous" du discord qui ont su toujours me soutenir tout au long de ce parcours.

Chapter 1

Résumé en Français

1.1 Motivations

Aux origines des temps, une quantité égale de matière et d'anti-matière a été créee. Alors que ces quantités auraient dû s'annihiler l'une avec l'autre, nous sommes actuellement l'exemple vivant attestant que cela ne s'est pas produit de cette façon. Depuis la découverte de l'anti-matière, la question du déséquilibre matière/anti-matière a intrigué les physiciens. Cette question a eu une piste d'explication en 1967 lorsqu'Andrei Sakharov a théorisé que pour justifier cette asymétrie, trois conditions étaient à respecter:

- Une violation du nombre baryonique.
- Une brisure de symétrie de Charge (C) et de symétrie combinée de Charge et de Parité.
- Un écart de l'équilibre thermodynamique.

Tout d'abord, intéressons nous au deuxième point. Les points un et trois seront traités en même temps.

Dans la nature, il existe des symétries qui stipulent grossièrement, que les particules doivent se comporter de la même façon avant ou après l'application d'une transformation, c'est-à-dire même masse, temps de vie, etc. Dans le cas des transformations les plus courantes comme les translations ou rotations dans l'espace, cela semble évident. Une particule devrait se comporter de la même façon en tout point de l'espace. Toutefois, pour les transformations dites discrètes, c'est-à-dire des transformations qui ne peuvent pas se décomposer en N contributions de transformations infiniment petites, l'exercice est moins intuitif. On s'intéresse aux trois exemple de symétrie discrètes les plus connues, les transformations C, P et T.

L'invariance sous symétrie de charge (C) stipule que toute particule se comporte de manière exactement identique que son anti-particule. L'invariance sous symétrie d'inversion de coordonnées (P) stipule qu'une inversion des coordonnées de l'espace laisse les particules inchangées. Enfin, une invariance par reversement du temps (T), dit que lorsqu'on "passe le film" à l'envers, les propriétés des particules restent identiques.

Ces trois symétries sont liées par un théorème : le théorème CPT. Ce dernier énonce qu'une brisure d'une ou d'une paire de symétrie implique que les opérations restantes doivent être brisées également. Ainsi, et cet exemple n'est pas anodin, une brisure de CP est équivalent à une brisure de T.

Par conséquent, pour expliquer l'asymétrie matière/antimatière les symétries C et CP doivent être brisées. C puisque si C est brisée l'interaction responsable de la production de plus de baryons que d'anti-baryons n'est plus compensée par cette transformation. Maintenant, si P n'est pas brisée la projection du spin sur la direction de l'impulsion sera inversée, ce qui mène à un équilibrage des baryons gauchers et des anti-baryons droitiers. C'est pourquoi, la combinaison des symétries CP doit être brisée.

Le nombre baryonique est définit comme suit:

$$B = \frac{1}{3}(n_q - n_{\bar{q}}) \tag{1.1}$$

avec n_q et $n_{\bar{q}}$, le nombre de quarks et d'antiquarks respectivement. Dans les premiers temps de l'univers, lorsque tout était à l'équilibre thermodynamique, le nombre baryonique était égal à zéro. La violation du nombre baryonique intervient pour justifier le fait que l'univers n'est pas entièrement rempli de gammas. Toutefois, des interactions en dehors de l'équilibre thermodynamique implique la fin de la réciprocité entre un état initial et un état final.

Ainsi, trouver des interactions violant T, donc CP, peuvent être reliées à cette asymétrie matière/anti-matière. Ce type d'interaction peut être trouvé dans le taux de désintégration beta:

$$\begin{aligned} w(<\vec{J}>|E_e,\Omega_e,\Omega_\nu)dE_e d\Omega_e d\Omega_\nu = \frac{F(\pm Z,E_e)}{(2\pi)^5} p_e E_e (E_0-E_e)^2 dE_e d\Omega_e d\Omega_\nu \\ \times \frac{1}{2}\xi\left[1 + a\frac{\vec{p_e}\vec{p_\nu}}{E_e E_\nu} + b\frac{m}{E_e} + \frac{<\vec{J}>}{J}.\left(A_\beta\frac{\vec{p_e}}{E_e} + B_\nu\frac{\vec{p_\nu}}{E_\nu} + D.\frac{\vec{p_e}\times\vec{p_\nu}}{E_{eE_\nu}}\right)\right] \end{aligned} \tag{1.2}$$

E_e, p_e et Ω_e sont les énergies totales, l'impulsion, et les coordonnées angulaires des particules beta, alors que E_ν, p_ν, et Ω_ν sont les équivalent pour les neutrinos. F$(\pm Z, E_e)$ est la fonction de Fermi qui contient les corrections Coulombienne dominantes, et $<\vec{J}>$ est la polarisation du noyau père avec J comme spin. ξ est défini tel que :

$$\xi = |M_F|^2(|C_S|^2 + |C_V|^2 + |C_S^{'}|^2 + |C_V^{'}|^2) + |M_{GT}|^2(|C_T|^2 + |C_A|^2 + |C_T^{'}|^2 + |C_A^{'}|^2) \tag{1.3}$$

avec $|M_F|$ et $|M_{GT}|$ les éléments de matrices des transitions Fermi et Gamow-Teller et $C_i^{(')}$ les différentes constantes de couplage correspondantes aux différentes natures mathématiques des interactions. Enfin, a, b, A, B, et D sont des paramètres de corrélations entre différentes grandeurs. En s'intéressant à D, on peut voir que cette constante est corrélée au spin $\vec{J}$ et les différentes impulsions des produits de désintégrations beta. Puisque T change le signe de ces grandeurs là, une valeur de D non nulle brise la symétrie T, cela brise également la symétrie CP selon le théorème CPT, faisant de D un bon candidat pour sonder une Nouvelle Physique (NP).

MORA s'inscrit donc dans l'héritage de la lignée d'expérience historique cherchant à sonder les nouveaux horizons de la physique moderne. Cette expérience repose sur un piège de Paul 3D dans lequel les ions radioactifs émetteurs beta y sont piégés. Autour du piège, une couronne de détecteurs est placée. La raison étant que d'après la formule eq. 1.2, on peut voir que la corrélation D est maximale dans un plan perpendiculaire au spin des noyaux pères. Il est donc capital de maîtriser cette direction, ce qui est réalisé très efficacement en

peuplant les niveaux hyperfins des ions radioactifs grâce à un laser Ti:Sa. Ce laser, polarisé circulairement, permet d'orienter la direction du spin dans la direction du faisceau. En changeant le signe de la polarisation, ce qui se traduit expérimentalement par l'ajout ou non d'une lame demi-onde, on peut donc inverser ou non la direction du spin toujours selon la direction du faisceau. Les produits de décroissances des ions, alors piégés, sont détectés par les détecteurs β et d'ions de recul (RIDE). Une première étape de preuve de principe consiste à mesurer le degré de polarisation P du nuage d'ions piégés, puisque D peut être défini comme suit :

$$\frac{N_{coinc}^{+45^\circ} + N_{coinc}^{+135^\circ} - N_{coinc}^{-45^\circ} - N_{coinc}^{-135^\circ}}{N_{coinc}^{+45^\circ} + N_{coinc}^{+135^\circ} + N_{coinc}^{-45^\circ} + N_{coinc}^{-135^\circ}} = \delta.D.P, \tag{1.4}$$

avec δ une constante qui dépend de l'angle solide de détection et des paramètres de désintégrations, D est le paramètre de triple-corrélation et enfin P est le paramètre de polarisation du nuage. D'une manière analogue à la formule précédente P peut se définir comme une asymétrie du nombre de coups mesuré tel que:

$$\frac{N_{\beta+}^{\uparrow} - N_{\beta+}^{\downarrow}}{N_{\beta+}^{\uparrow} + N_{\beta+}^{\downarrow}} \; \alpha \; A_\beta \; . \; P \tag{1.5}$$

avec la flèche symbolisant la direction du spin, soit parallèle soit anti-parallèle à l'axe du faisceau et A_β est le paramètre d'asymétrie beta connu pour le ^{23}Mg comme étant $A_\beta(^{23}\text{Mg})$ = -0.5541(20). La mesure de P est réalisée à l'aide de détecteurs annulaires[1] silicium placés de part et d'autre du piège, derrière les lentilles.

1.2 Mise en service de l'expérience MORA

La mise en service, ou "commissioning", de MORA s'est réalisée en deux temps.

La première phase de cette mise en service a été effectué au sein du Laboratoire de Physique Corpusculaire de Caen. Cela a consisté en l'étude de la ligne d'injection de MORA ainsi que des premiers tests de piégeage. La ligne a été testé à l'aide d'une source à ionisation de surface stable de ^{23}Na. Cette source était couplée à un RFQ cooler buncher, ou RFQCB, afin de reproduire le comportement du faisceau dans les conditions réelles de l'expérience. Ce RFQCB consiste à quatre cylindre métalliques couplés en tension oscillante deux-à-deux. Ce faisant, les ions sont émis de manière continue de la source et ils s'accumulent dans le piège linéaire radio-fréquence. Le paquet d'ions est alors envoyé dans la ligne à 2 kV puis plus tard à 1.5 kV. La ligne comporte plusieurs éléments permettant de ralentir le faisceau (see Fig. 1.1). Cela consiste en deux cavités pulsées ("pulse drift tubes", PDT) consistant en deux cylindres creux dont la tension appliquée passe d'une haute tension positive qui permet de ralentir les ions avant leur entrée dans la cavité, puis lorsque les ions se trouvent à l'intérieur du PDT, la tension est négative, faisant que, lorsque les ions sortent du PDT, ils sont ralentis une deuxième fois et refocalisés grâce à l'application de cette tension négative.

[1] Afin de laisser passer les faisceaux (ions et laser) jusqu'au piège.

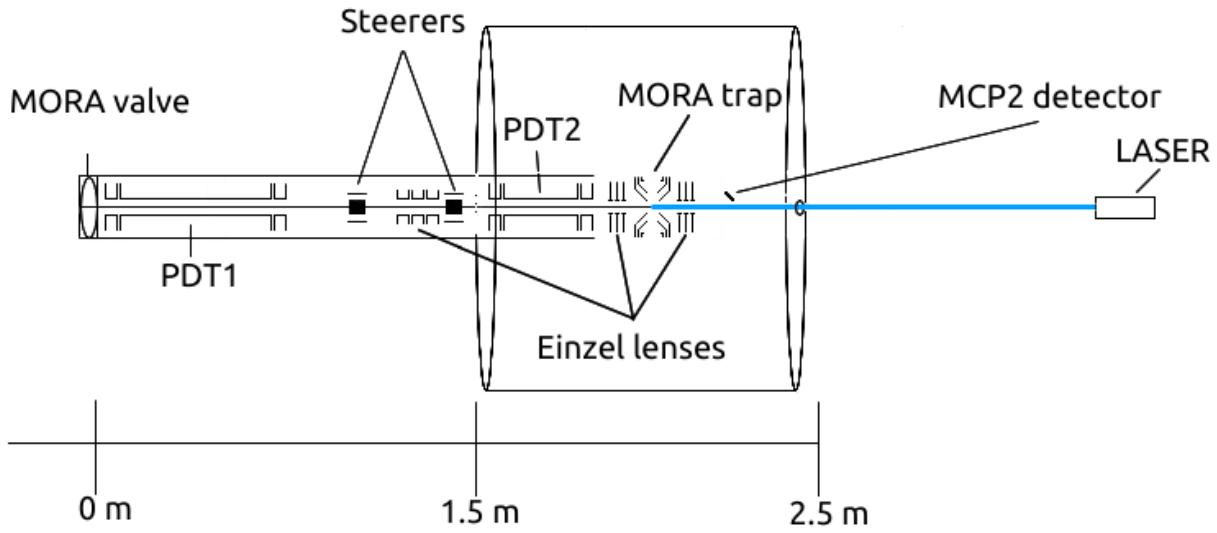

Figure 1.1 – Schéma de la ligne de MORA. Les détecteurs ne sont pas affichés.

Dans le cadre de la mise en service au LPCC le PDT1 était utilisé comme simple lentille car les ions émis avaient la bonne énergie à ce niveau de la ligne. Le reste des éléments de ligne sont des lentilles de Einzel et des déflecteurs permettant respectivement de refocaliser et de corriger la trajectoire XY du faisceau. Juste avant le piège se trouve le PDT2 dont le fonctionnement vient d'être présenté. Enfin, le piégeage se fait en trois temps:

- L'injection : les ions en sortie du PDT2 ont encore une énergie cinétique d'environ 100 eV. Cela implique qu'il faut les ralentir une dernière fois et cette étape est réalisée grâce à l'électrode R4 du piège (voir Fig. 1.2). Une tension est appliquée sur cette dernière afin que les ions aient une énergie cinétique de l'ordre de 0 eV.

- Le piégeage : une fois l'injection réalisée, une tension dite radio-fréquence est alors appliquée sur les électrodes R1 et R2. Cette tension va osciller parcourant deux extremum de tension, un positif et un négatif. Ce dispositif repose sur le principe de faire alterner une direction de fuite des ions. Cette dernière existe puisqu'un piégeage tridimensionnel statique est impossible. Il existe toujours une direction, un axe le long duquel le puits de potentiel n'est pas assuré. On obtient alors une forme de potentiel du type "selle de cheval" (voir Fig. 1.3). Ainsi, en alternant cette forme de potentiel, on fait alterner cette direction de fuite suffisamment rapidement pour que les ions piégés au centre ne puissent pas s'échapper. Toutefois, n'importe quelle tension ne suffit pas pour réussir à piéger les ions. En effet en fonction de la masse et de la charge de ces derniers mais aussi de la tension appliquée, le nuage peut se retrouver dans une zone d'instabilité provoquant ainsi la perte du nuage. Ces zones sont définies par des paramètres appelés les paramètres de Mathieu. En traçant l'un en fonction de l'autre, on se retrouve avec des zones particulières marquant les zones de stabilité ou jeu de paramètres de Mathieu pour lesquels un piégeage peut s'avérer possible.

- L'extraction : l'extraction des ions dans le piège est réalisée en appliquant une tension sur l'électrode R3, une fois que le piégeage est stoppé. Une tension importante (1000 V) est appliquée, poussant les ions vers une lentille de Einzel puis vers un détecteur à micro-canaux (MCP) qui permet de les compter.

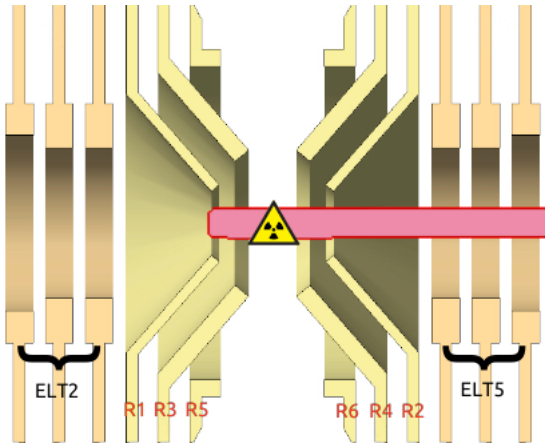

Figure 1.2 – Schéma en coupe du piège selon l'axe du faisceau. Les électrodes sont labellées allant de R1 à R6. Le piège, quant à lui, est encadré par deux lentilles de Einzel permettant une focalisation avant et après piégeage. Le cylindre rouge symbolise l'ensemble des sources radioactives que l'on peut insérer à loisir afin de réaliser des calibrations de détecteurs en dehors des périodes de faisceaux.

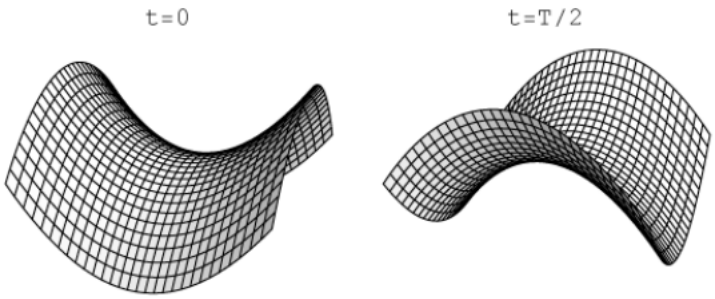

Figure 1.3 – Forme de "selle de cheval" du potentiel appliqué par un piège de Paul 3D.

Le commissioning réalisé au LPCC a été facilité par la réalisation de simulations SIMION. En effet, SIMION offre un environnement dédié à la conception de simulation de faisceaux d'ions chargés de basses énergies. Ainsi, en reconstruisant la ligne d'injection et le piège de MORA, elles ont permis de commencer les tests de piégeage avec succès. Des tests de dispersion en énergie ont également été réalisés dans le but de sonder l'énergie des ions après le ralentissement du PDT2. Ces tests sont faisable grâce à une grille devant la MCP sur laquelle une tension est appliquée. En faisant varier cette tension, le nombre d'ions collecté en aval sur la MCP va également varier et ainsi, intuitivement, plus la tension appliquée sur cette grille est importante plus le nombre d'ions collectés chute. En traçant ces deux variables on peut déterminer leur énergie moyenne. Des tests d'efficacité de transmission et de piégeage ont également été effectué afin de connaître les efficacités de transmission et de piégeage.

Le dispositif expérimental a été transporté en décembre 2021 et en Janvier 2022 à Jyväskylä en Finlande. Une fois installé, des tests sensiblement similaires à ceux réalisés au LPC Caen, ont été réalisés. Toutefois, contrairement à la mise en service faite au LPC, plusieurs type de sources stables ont été utilisées:

- Une source à ionisation laser : un palet de sel a été placé dans la ligne d'IGISOL, proche de l'entrée de MORA sur un dispositif rotatif. Un laser disposé à l'extérieur de la ligne vient éclairer le palet de sel. Comme celui tourne, le laser n'endommage pas l'échantillon rapidement.

- Une source à ionisation de surface : Cette source est la source utilisée lors du premier commissioning et placée en amont du RFQCB d'IGISOL. Celui-ci est beaucoup plus complexe que celui décrit précédemment. Il ralentit les ions grâce à une succession d'électrodes. Une fois que ces derniers sont sur le point de repartir dans le sens inverse, ils sont piégés par un piège de Paul 2D puis mis en paquet par un "minibuncher" dont le fonctionnement repose sur une succession d'ouvertures et de fermetures de portes de potentiel avant d'être éjectés en paquet dans la ligne.

- Une source à décharge : sûrement la source stable utilisée qui s'est avérée la plus efficace. Cette source à étincelle repose sur un principe physique simple mais redoutable ment efficace : la loi de Paschen. Cette dernière stipule qu'un arc électrique peut se former entre deux électrodes lorsqu'elles sont soumises à une certaine tension, le tout baignant dans un gaz. Bien sûr, en fonction de la nature du gaz et de la distance entre les deux électrodes, cette tension de claquage ne va pas avoir la même valeur. C'est pourquoi, une tension radio-fréquence est appliquée sur les électrodes laissant pour seul paramètre libre, la pression de gaz (ici de l'hélium).
  Les électrodes consistent à des échantillons de métaux purs donc dans notre cas du ^{23}Na et du titane. Toutefois, l'inconvénient de cette source est que l'échantillon utilisé était très rapidement endommagé et nécessitait un remplacement quasi-quotidien.

Ces tests ont précédé les premiers temps de faisceau radioactif de ^{23}Mg. En tout et pour tout, trois tests en ligne ont été effectués en 2022. Les deux premiers, ceux de février et de mai, ont été caractérisés par une forte contamination de ^{23}Na (de l'ordre de 2000 contaminants pour 1 noyau d'intérêt). Différents problèmes techniques ont permis d'affiner le dispositif pour que ce dernier soit suffisamment robuste pour acquérir correctement des données. Ainsi durant le temps de faisceau de novembre, près de 30h de données ont été prises avec l'utilisation du faisceau laser. Au total cela donne 10h pour chaque polarisation laser (σ-,σ+ et sans laser).

1.3 Analyse des premières données

Après la campagne de prise de données de novembre 2022, la mesure du degré de polarisation P s'est trouvée potentiellement réalisable grâce à la quantité de données exploitables. Afin de pourvoir accéder à cette observable, deux méthodes sont possibles :

- Les deux détecteurs Silicium sont utilisés pour une configuration de laser donnée. Ici,

soit σ^+ ou σ^-. L'asymétrie est telle que :

$$P \sim \frac{\text{Nb de coups détecteur 1} - \text{Nb de coups détecteur 2}}{\text{Nb de coups détecteur 1} + \text{Nb de coups détecteur 2}} \tag{1.6}$$

- Un détecteur Silicium pour deux configurations de laser différentes. L'asymétrie est déterminée de la manière suivante :

$$P \sim \frac{\text{Nb de coups détecteur } \sigma^+ - \text{Nb de coups détecteur } \sigma^-}{\text{Nb de coups détecteur } \sigma^+ + \text{Nb de coups détecteur } \sigma^-} \tag{1.7}$$

Sur un cycle de 3 s, 2 s sont attribués au piégeage en lui-même à la suite de quoi les ions sont extraits du piège. La dernière seconde est dédiée à la mesure de l'environnement radioactif. C'est-à-dire mesurer la contribution des ions "non-piégés". En complément de cela, des fichiers dédiés à la prise de mesure de bruit de fond électronique ont été acquis conformément aux différentes configurations laser.

Ainsi, nous sommes désormais en mesure de supprimer toute forme de bruit, que ce soit électronique ou radioactif des données résultant des ions piégés. Le premier est beaucoup plus simple à traiter puisque il suffit simplement de soustraire les spectres un à un. Le second, en revanche, est plus complexe. En effet, il doit également être purifié du bruit électronique mais la difficulté majeure réside dans le fait que les ions non-piégés se désintègrent durant les deux secondes de piégeage. Cela induit de reconstruire la contribution radioactives des évènements non-piégés durant le piégeage (see Fig. 1.4). Pour ce faire, on effectue un ajustement à l'aide d'une fonction exponentielle décroissante de la forme $y(t) = Ae^{\lambda t}$ où la constante de désintégration λ est arbitrairement fixée telle que $\lambda = \frac{ln(2)}{T_{1/2}(^{23}\text{Mg})}$ avec $T_{1/2}(^{23}\text{Mg})$ est la demi-vie du ^{23}Mg ayant pour valeur 11.317 s[2]. On remplit un histogramme avec la distribution de la fonction exponentielle reconstruite puis on soustrait cet histogramme aux données piégées obtenant ainsi les données nettoyées du bruit de fond. Les données provenant de chaque canal du même détecteur sont sommées donnant ainsi le nombre de coups total correspondant d'une configuration laser.

Ces données sont résumées dans le tableau. 1.1

On peut conclure de cette analyse que, d'après les données récoltées en novembre 2023, aucun signe de polarisation du nuage n'est visible puisque cette dernière ce trouve complétement dominée par ses incertitudes statistiques. La contamination en ^{23}Na est trop importante, et les données sont entièrement dominées par les ions non piégés.

1.4 Étude des détecteurs Phoswich

Les détecteurs phoswich font partie des trois types de détecteurs utilisés dans MORA. Ils consistent en deux scintillateurs plastiques de caractéristiques différentes telles que l'épaisseur (mince et épaisse) ainsi que le temps de réponse (rapide et lent). Ces deux scintillateurs sont collés mécaniquement et joints à un photo-multiplicateur. L'utilité de deux scintillateurs plastiques permet la discrimination entre les types de particule détectées. En effet, les gammas sont détectés principalement dans le scintillateur le plus épais puisque la probabilité d'interaction est négligeable dans le scintillateur mince. Les betas quant à eux sont

[2]Selon le site web https://www.nndc.bnl.gov/

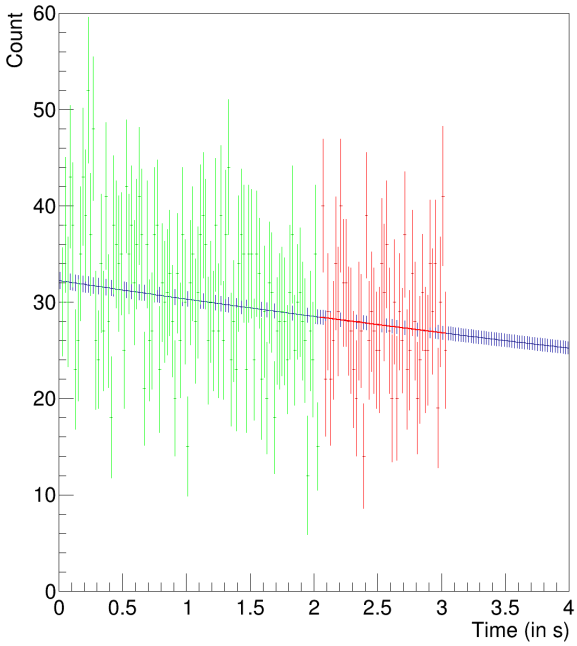

Figure 1.4 – Cette figure montre les deux contributions des différents signaux. En vert, cela correspond aux données des ions piégés et en rouge aux données "offtrap". La fonction exponentielle, ici visible en bleue, est reconstruite à partir du paramètre libre obtenu grâce à l'ajustement réalisé également visible en rouge.

Configurations	***Si 1***	***Si 2***	***Asymmetry***
2 Detectors With Half-Plate	89.22 ± 85.49	23.91 ± 125.18	-0.58 ± 1.55
2 Detectors Without Half-Plate	27.65 ± 94.48	181.99 ± 129.99	-0.74 ± 0.95
2 Detectors Without laser	-82.85 ± 73.69	-116.60 ± 111.35	-0.17 ± 0.68
Configurations	$\sigma+$	σ-	***Asymmetry***
Si 1	27.65 ± 94.48	89.22 ± 85.49	-0.53 ± 1.23
Si 2	180.00 ± 129.99	23.91 ± 125.18	0.77 ± 1.10

Table 1.1 – Ce tableau comporte deux parties. La première résume le nombre total de coup en fonction de la configuration σ^+ (ici "without half-plate") et σ^- (ici "with half-plate"). La deuxième partie de ce tableau présente pour une configuration de détecteurs, donc ici détecteur 1 ou 2, le nombre de coup total pour chaque configuration laser.

détectés dans les deux, néanmoins les betas retro-diffusés eux ne sont détectés que dans le scintillateur mince ne laissent aucun signal dans le scintillateur épais.

Du fait de ces différent scintillateurs, on peut séparer les charges provenant de ces derniers. C'est possible grâce à leurs différents temps de réponse. Ainsi, une charge lente, Q_{slow}, et rapide, Q_{fast}, existent ainsi que la charge totale, Q_{tot}, la somme des deux. Cependant, ces charges sont corrélées l'une avec l'autre puisque le signal lent à une contribution dans le signal rapide et inversement. C'est la raison pour laquelle la première étape de toute analyse de données récoltées par ces détecteurs consiste à décorréler ces données.

Après une étape de calibration à l'aide d'une source de ^{207}Bi, une étude plus poussée à l'aide de simulations réalisées avec GEANT4 a été effectuée. Une réplique du dispositif expérimental de calibration (différent de la chambre à vide de MORA) a été créee. Toutefois, les spectres simulés sont pur de toute dégradation expérimentales (la propagation de la lumière et le signal crée par le PM ne sont pas simulés) et c'est pourquoi, nous devons dans un premier temps, dégrader ces spectres. Ainsi, différentes valeurs de calibration et aussi de facteur de dégradation de spectre sont testés dans la même boucle algorithmique. Un test de χ^2/NdF est réalisé en superposant les deux spectres pour chaque jeu de paramètres. Un élément important du dispositif à simuler est le support de source (Aluminium) qui reproduit la majeure partie des événements entre les pics principaux. Lorsque l'accord est proche de 1, il apparaît toutefois qu'une différence majeure d'amplitude existe sur le pic à 481,86 keV.

La raison de cette différence singulière a été explorée par plusieurs pistes de réflexion :

- Une différence de rapport d'embranchement : deux simulations ont été comparées sur le rapport de l'intensité de deux pics (données GEANT4 et données LNHB). Une partie de la différence d'amplitude peut être expliquée de cette manière.
- Une différence d'épaisseur : une hypothèse était que l'épaisseur du scintillateur mince différait de celle simulée (0.50 mm). C'est pourquoi plusieurs valeurs ont été testées commençant allant de 0.3 mm à 0.53 mm. Cette dernière se trouve être dans l'acceptance d'erreur de mesure initiale du scintillateur.
- Une dégradation spectrale incorrecte: cette hypothèse stipulait que la dégradation du spectre simulé n'était pas réalisée correctement. C'est pourquoi plusieurs facteurs de dégradation ont été testés puis comparé au spectre expérimental.

Cette étude bien qu'explorant plusieurs pistes prometteuses n'a pas su totalement expliquer l'origine de la différence d'amplitude des deux spectres.

1.5 Conclusion

MORA s'inscrit dans la lignée des expériences de précision à basse énergie visant à mesurer le paramètre de triple-corrélation D. Ce paramètre, corrélé avec le spin du noyau père et des différentes énergies et impulsions beta et des neutrinos, est supposé être nul selon le Modèle Standard. Une valeur non-nulle de D indiquerait une brisure de symétrie T et donc de CP selon le théorème CPT. Cette brisure de symétrie est l'une des trois conditions définies en 1967 par A.Sakharov renseignant sur l'asymétrie matière anti-matière lors de la baryogénèse.

MORA cherche donc d'améliorer la sensibilité de D abaissant ainsi cette valeur jusqu'à 10^{-5}. Pour ce faire, un dispositif de piégeage est couplé à un système de détection disposé en couronne afin d'assurer une corrélation maximale de D. Le piège également fonctionne de pair avec un laser qui peuple les niveaux hyperfins des noyaux piégés assurant ainsi l'alignement des spins des noyaux piégés selon l'axe du faisceau. Le ^{23}Mg sera le premier étudié avec ce dispositif.

Cette expérience est récente dans le paysage expérimental et j'ai contribué, dans le cadre

de ma thèse, au fonctionnement de MORA en réalisant des travaux de simulation SIMION ainsi que la manipulation d'ions à basse énergie. Le déménagement de MORA en Finlande à également permis des tester ce dispositif dans un environnement plus complexe que celui du LPC Caen, faisant intervenir des appareils complexes de manipulation ionique tels que le quadrupole radio-fréquence pour le refroidissement et la mise en paquet d'ions ou RFQ-CB. Plusieurs sources de calibration de nature différente ont pu être testée avec chacune leur spécificité. Trois temps de faisceaux dédiés ont été utilisé dont deux servant au perfectionnement de la mise en service de la ligne et du piège. Le dernier temps de faisceau de novembre dernier a permis d'acquérir des données exploitables pour les premières mesures de degré de polarisation P. L'analyse a montré qu'aucune polarisation n'a été observée. Plusieurs facteurs peuvent expliquer cette raison, toutefois le haut facteur de contamination du faisceau radioactif en ^{23}Na stable induisant une très faible statistique exploitable reste le problème majeur à régler. Des pistes visant à réduire la présence de contamination ont été testée en mai 2023. Cela consistait à couvrir la cible de ^{24}Mg avec une couche de BaO. Cette couche protectrice avait pour but d'empêcher les ions de sodium de quitter la source puisque qu'on suspectait que la source en contenait en son sein et que l'énergie dégagée par la réaction entre le faisceau de proton et cette dernière puisse éjecter les sodium prisonniers. Néanmoins, il semblerait qu'aucune amélioration n'ait été observée. Des pistes de réflexion utilisant du CF_4 ou du SF_6 permettrait de former des composés moléculaires à base de Magnésium permettant, ainsi, de purifier le faisceau en sélectionnant une masse plus importante lors de la sélection faite par l'aimant.

Enfin, plusieurs études réalisées sur les détecteurs phoswich ont permis d'avoir une meilleure compréhension des données simulées qui avaient pour but de perfectionner la calibration des détecteurs. La cause d'une différence d'amplitude entre les spectres simulés et expérimentaux a été recherché et n'est pour l'heure pas encore comprise parfaitement. Des tests sur l'épaisseur du scintillateur mince, des rapports d'embranchements des électrons de la source d'étalonnage de ^{207}Bi ou encore les facteurs de résolutions en énergie des détecteurs ont permis de débroussailler le terrain, toutefois, ils nécessitent de réaliser des études plus fines et plus spécifiques pour chaque détecteurs.

Chapter 2

Introduction

In nuclear physics, the study of beta decay stands as a cornerstone that offers profound insights into the fundamental interaction that rules our world. Beta decay processes are characterised by the transformation of a proton into a neutron and vice versa. While this transformation seems to be rather straightforward to understand, it has puzzled many physicists over the years leading to great discoveries such as the discovery of the neutrinos to the anti-matter itself.

Since its theorising, antimatter has always puzzled physicists because of its imbalance regarding our world of matter. The experimental discovery of a violation of a fundamental symmetry, the parity also known as the space inversion has led to the formulation of three conditions, known as the Sakharov conditions, that could explain the matter-antimatter imbalance. One of them, the C (charge symmetry) and CP (charge and parity) violation has defined the motivation for the MORA experiment.

Motivated by the observation of the so-called triple correlation parameter D, which has been fully theorised along the rest of the correlation constants by J.D. Jackson et. al. in 1957[JTW57], the MORA experiment tends to enhance the sensitivity of such measurement. Indeed, a non-zero value of D is symptomatic of a time reversal symmetry violation, and according to the CPT theorem, developed in the first chapter of this thesis, it is equivalent to a CP violation.
Therefore, by raising the sensitivity on D, the MORA experiment aims to improve our knowledge of the limits of the Standard Model and eventually, discover new physics beyond.

This thesis presents the experimental works done on the MORA experiment starting from the commissioning of the early stage to the first analysed data. In the pages that follow, we will delve into the theoretical background of beta decay presenting the triple correlation parameter. The first chapter ends with a presentation of the state of the art of the D measurements and a general description of the MORA experiment concludes the chapter giving the keys to understand the choices made for it.

In the second chapter, a presentation of the concepts of electromagnetic trapping using Paul's traps is given. The development of the Mathieu equations leads to a stable trapping process. This is linked directly to the properties of the MORA trap. At the end of this chapter, a table resuming the characteristics of the MORA trap is given.

The next chapter is dedicated to the commissioning of the MORA Trap and its injection line.

The commissioning of the set-up, first done in LPC Caen, is detailed including tests of the injection line with a stable source, the first trapping of the experiment and a comparison with some simulations. In the second part of the chapter, the commissioning, done within the JYFL laboratory, is presented with, in particular, several tests with different stable sources, energy dispersion tests and, finally comparison of simulations. Finally, the different values of transmission and efficiencies are detailed for each beam time done within at the IGISOL facility.

The fourth chapter presents the analysis of the first set of data taken in November 2022. A detailed study of the background removal has been done. This is a critical step because two different kinds of background are polluting the data. The chapter ends with a table resuming the results of the beam-time.

The last chapter is dedicated to a detailed study of the phoswich detectors. Charges are correlated due to different time responses of the plastic scintillators. This correlation needs to be solved to proceed further. GEANT4 simulations are also presented. They were conducted to better understand the device and the effects of the detector environment on its response function, to improve the calibration in energy.

Finally, a conclusion of this work is given, reminding first its main results and exploring several leads of improvements.

Chapter 3

Context

3.1 Theory of the Standard Model

Finalized in the mid-70s, the Standard Model (SM) aims to describe the fundamental interactions and the different elementary particles by the exchange of mediator bosons. It succeeds in gathering the theory of Glashow, Weinberg and Salam [SGW79] of the electroweak interaction with quantum chromodynamics (QCD). The successive experimental discoveries of the top-quark, the tau neutrino, and the Higgs boson gave credit to the SM that already defined with accuracy the three of the four fundamental interactions (see 3.1.2).

The following development is based on the references in [Lié10],[Sev04], [Fab15] and [Mui65].

3.1.1 Particles

Bosons

The mediators of fundamental interactions[1] are bosons, particles characterised by an integer spin.

- The strong interaction is driven with the help of 8 massless gluons (see Sec. 3.1.2.1) which carry the colour charge.
- The weak interaction (see Sec. 3.2), is driven by two kinds of particles: The $W^{\pm}$ which are electrically charged, and the Z boson which is neutral. Those are massive bosons, where the masses can be found in Table 3.1.
- The electromagnetic interaction is driven by photons that are massless particles.

3.1.1.1 Fermions

Particles with half-integer spin are called fermions. They are elemental bricks of matter and are subdivided into two categories: quarks and leptons described below.

[1] The graviton, the hypothetical boson responsible for the gravitational force.

Name		*Mass* (GeV/c^2)	*Transmitted interactions*	*Charge*		
				Strong	*Weak*	*EM*
Photon	γ	0	EM	no	no	no
Boson W	$W^{\pm}$	80.4	Weak	no	Yes	Yes
Boson Z	Z	90.2	Weak	no	Yes	no
Gluon	g	0	Strong	Yes	no	no
Higgs Boson	h	125	None	no	Yes	no

Table 3.1 – Summary of the bosons that carry the fundamental interactions, except gravity.

Quarks

The quarks [Gel64] are base components of the baryon particles, such as protons and neutrons, and mesons, such as the pion. They are gathered in 3 families.

Quarks have an intrinsic charge, isospin, and colour. This last notion refers to the strong

Generation	*Flavor*	*Mass*	*Q (charge)*
1	up (u)	$2.3^{+0.7}_{-0.5}$ MeV	+2/3
	down (d)	$4.8^{+0.5}_{-0.3}$ MeV	-1/3
2	charm (c)	1.275 ± 0.025 GeV	+2/3
	strange (s)	95 ± 5 MeV	-1/3
3	top (t)	$173.07 \pm 0.52 \pm 0.72$ GeV	+2/3
	bottom (b)	4.18 ± 0.03 GeV	-1/3

Table 3.2 – Quark properties detailed in [Fab15].

interaction that will be developed later (see Sec. 3.1.2.1). To this day, quarks have not been seen experimentally as a single structure but instead, they gather in structures. If a quark and an anti-quark are binding together, they are forming *Mesons* such as kaons ($K^0 = d\bar{s}$ or $\bar{K^0} = \bar{d}s$) for example. Baryons are regrouping any particles whose inner structure is made of an odd number of quarks (minimum of 3), although the most known form is nucleons which are composed of three quarks, *uud* for the protons and *udd* for the neutrons, structures made of 5 quarks, called pentaquarks [Col+], also exist. A higher structure of an odd number of quarks has not been observed yet, however, the tetra-quark, a four-quark structure, has been detected [col20].

Leptons

They are divided into different categories: electronic, muonic, and tauonic.

- **Electronic:** Electrons (e-) and Electron neutrinos (ν_e)
- **Muonic:** Muons (μ) Muon neutrinos (ν_μ)
- **Tauonic:** Tau (τ) and Tauon neutrinos (ν_τ)

Electrons, muons, and taus have a charge q=-1 and are massive particles. They, with the neutrinos, are elementary particles that, like quarks, do not have a known inner structure[2].

[2] At least, not yet discovered.

Generations	***Leptons***	***Mass (MeV)***
Electronic	$e^{\pm}$	0.511
	ν_e	$< 7.3\times10^{-3}$
Muonic	μ	105.66
	ν_μ	< 0.27
Tauonic	τ	1784.1
	ν_τ	< 35

Table 3.3 – Mass of leptons coming from [BJH95].

For each charged lepton, a neutral neutrino is associated. The leptonic neutrinos have a small mass compared to the other leptons and are only interacting through weak interaction since they do not have neither a charge nor a colour, with very low cross-sections making them especially difficult to detect.

Each lepton has an anti-particle associated with the same mass and opposite charge. For the neutrinos, it is slightly different since a theory [MM06], established in 1937, stipulates that they are their own antiparticle, called a Majorana particle. Described as massless particles in the Standard Model, experimental discovery seems to point out that neutrinos do have a masses as oscillations between neutrino states have been observed as described in [GM08] which is only possible if at least one type of neutrino has a non-zero mass. This is an interesting topic since it can lead to New Physics (NP), forcing the SM to be reworked in a more inclusive theory of particle physics. Finally, neutrino oscillations have motivated some of the largest collaborations in the world such as SuperKamiokande [Akh+99] or the DUNE experiment [Abi+20].

To resume, the fundamental particle and bosons are gathered in table. 3.4.

Generations	***Particle***	***Mass (MeV)***	***Q (Charge)***
Electronic	$e^{\pm}$	0.511	$\pm$ 1
	ν_e	$< 7.3\times10^{-3}$	0
Muonic	μ	105.66	-1
	ν_μ	< 0.27	0
Tauonic	τ	1784.1	-1
	ν_τ	< 35	0
1	up (u)	$2.3^{+0.7}_{-0.5}$ MeV	+2/3
	down (d)	$4.8^{+0.5}_{-0.3}$ MeV	-1/3
2	charm (c)	1.275 $\pm$ 0.025 GeV	+2/3
	strange (s)	95 $\pm$ 5 MeV	-1/3
3	top (t)	173.07$\pm$0.52$\pm$0.72 GeV	+2/3
	bottom (b)	4.18 $\pm$ 0.03 GeV	-1/3
N/A	Gluons	0	0
	Photons	0	0
	$W^{\pm}$	80.385$\pm$ 0.015 Gev	$\pm$1
	Z^0	91.188 $\pm$ 0.002 GeV	0

Table 3.4 – Table resuming fermions and leptons generations.

3.1.2 Interactions

There are four known fundamental interactions: the strong interaction, the weak interaction, the electromagnetic interaction and the gravitational interaction. In this section, we will briefly present these interactions before concentrating on the weak interaction. The presentation of the gravitational interaction will be very brief, given its strength in the subatomic medium. This interaction is different from the others in that it is not yet included in the description of the SM. This question leads to certain theories aimed at the "theory of everything", where all the interactions are linked to each other at the quantum level. The dream shared by all physicists would be to have a model that describes them all, thus resolving all modern questions with an elegant model of "everything".

However, before we reach this pinnacle of humankind, let's continue our journey through the fundamental interactions.

3.1.2.1 The strong interaction

The strong interaction applies to hadrons, *i.e.* particles made of quarks, at a very short range. Regarding the configuration of the atomic nucleus, *i.e.*, positively charged protons confined with some neutrons at a very close range (10^{-15} m), this interaction has to be attractive and effective at a very close range in order to counter-balance the Colombian repulsion. Moreover, the strong interaction is independent of the electric charge which means it does not distinguish between protons and neutrons.

The gauge theory describing the strong interaction has been named accordingly "Quantum ChromoDynamics (QCD)" and was published in 1973 by Fritzsch, Leutwyler, and Gell-Mann [FGL73]. In this theory, a new charge was introduced called "colour" three in number: Red (R), Blue (B), and Green (G) with the associated anti-colours: $\bar{\mathrm{R}}, \bar{\mathrm{B}}$ and, $\bar{\mathrm{G}}$. The gluons carry one colour and one anti-colour, meaning that when particles exchange gluons, a flow of colour is created between them. Similarly to the electric charge, the colour number must be conserved. Thus, if we consider a blue quark, it cannot get rid of its colour by emitting a blue gluon since it will imply that the quark will be colourless, which does not exist. However, if the quark is emitting a blue-antigreen gluon, the colour number is conserved if the outgoing quark is green. The strong interaction is, thus, mediated by massless gluons which are gauge bosons and they carry one colour and one anti-colour such as:

$$\mathrm{R\bar{R}},\ \mathrm{R\bar{B}},\ \mathrm{R\bar{G}},\ \mathrm{B\bar{R}},\ \mathrm{B\bar{B}},\ \mathrm{B\bar{G}},\ \mathrm{G\bar{R}},\ \mathrm{G\bar{B}},\ \mathrm{G\bar{G}}$$

Any particle that carries the colour and its anti-colours or the three colours or anti-colour at once is considered colourless and has a colour charge of zero. Finally, since the gluon is colour-charged it can interact with itself, which is not the case for photons in electromagnetism. This phenomenology is even more different since the strong interaction intensity increases with the distance making the deconfinement of a single quark impossible. However, due to the asymptotic freedom [Dav74] property of the strong interaction, the quark confinement can be broken at high energies.

3.1.2.2 The electromagnetic interaction

Among all interactions, the electromagnetic one is certainly the most known after the gravitational one. This force is driven by the photons which interact with any charged particle. Classical electromagnetism was described by Maxwell at the end of the 19th century with the help of four equations:

$$\vec{\nabla} \cdot \vec{E} = \frac{\rho}{\epsilon_0} \quad ; \quad \vec{\nabla} \times \vec{E} = -\frac{\partial \vec{B}}{\partial t} \tag{3.1}$$

$$\vec{\nabla} \cdot \vec{B} = 0 \quad ; \quad \vec{\nabla} \times \vec{B} = \mu_0(\vec{j} + \epsilon_0 \frac{\partial \vec{E}}{\partial t}) \tag{3.2}$$

with $\vec{E}$ and $\vec{B}$ the electric and magnetic fields, ρ the charge density and $\vec{j}$, the current density. Nowadays, it is precisely described at a quantum scale by the Quantum ElectroDynamics theory (QED). This interaction leads to either attractive force between opposite charges or repulsive charges between the same charges. Moreover, when a charged particle is subject to acceleration, it spreads an electromagnetic wave through space. The particles interact with the EM fields by exchanging quanta, i.e. photons. At first order, the strength of EM, given by the fine structure constant, is $\sim 10^{-2}$ less than the strong interaction.

3.1.2.3 The gravitational interaction

This interaction is very well described at a macroscopic level and is particularly efficient in explaining orbital mechanics. It has an infinite range, but the strength is extremely weak

compared to the other interactions. At a quantum scale, it is negligible compared to the strong interaction (factor of $\sim 10^{-39}$).

This interaction is surely the most known, however, lately[3] [Ein22] the theory of special and general relativity was introduced by Albert Einstein and has changed the paradigm of modern physics. This theory has completely reshuffled modern physics allowing later, the emergence of theories such as black holes and transforming modern society with the development of satellites for example.

Finally, unlike other interactions, the gravitational force has not yet been linked to any successful quantum theory, and this remains one of the major issues of theoretical physics.

3.2 Weak interaction

The weak interaction is involved in the radioactive β decay. It has an even shorter range than the strong force ($\sim 10^{-18}$ m) and thus acts only over microscopic distances and it is weaker ($\sim 10^{-5}$). Moreover, contrary to the strong interaction, the weak interaction applies between all particles and contrary to other interactions, it does not create a bound state such as atomic nuclei for the strong, molecular state for the EM and planets and stars for gravity.

The first theory of weak interaction was established by E.Fermi in 1934 [FER34] where neutrinos were introduced. The most common example which illustrates the beta decays is a neutron's decay:

$$n \longrightarrow p + e^- + \bar{\nu_e} \tag{3.3}$$

where a neutron decays into a proton, an electron, and an anti-neutrino. This decay can occur to a free neutron due to the fact that the mass of a neutron is higher than the combined proton and electron masses. The free neutron has a lifetime of around 15 min and its value is currently being debated because of the significant differences between τ_{trap}, the lifetime observed in trap experiments, and τ_{beam}, the lifetime observed in beam experiments as shown in Fig. 1 in [Ber09]. A decay mode called "neutron dark-decay" [FG18] could explain this difference, but has not yet been proven experimentally [Jou+23].
There is also the corresponding equation above but with a neutrino such as:

$$n + \nu_e \longrightarrow p + e^- \tag{3.4}$$

Fermi, then, constructed his theory by making an analogy with electromagnetic radiation. This one is proportional to the electric current four-vector as described in [Mui65].

The resulting Hamiltonian describing the beta disintegration can be built as a local interaction with four fermions mixing both the leptonic and hadronic currents. It has, furthermore, to be invariant over a proper Lorentz transformation and can be expressed as in [Lié10]:

$$H = \sum_{i=S,V,T,A,P} \int \vec{dr}[\bar{\psi_p}(x)O_i\psi_n(x)][C_i\bar{\psi_e}(x)O_i\psi_\nu(x) + C_i'\bar{\psi_e}(x)O_i\gamma^5\psi_\nu(x)] + h.c. \tag{3.5}$$

[3] One century ago.

with i taking the different letters S,V,T,A, and P meaning respectively Scalar, Vector[4], Tensor, Axial vector[5] and Pseudoscalar[6]. O_i are operators expressed in terms of Dirac matrices or γ-matrices (see table. 3.5). C_i and C_i' are coupling constants that indicate the intensities of the interactions and can be complex. This Hamiltonian is invariant under proper Lorentz transformation but not under specific improper Lorentz transformations such as space-reflection (see Sec. 3.2.1.2.2) or charge conjugation (see Sec. 3.2.1.2.1) for example. The conditions imposed on the Hamiltonian to be invariant under broken symmetries are explored in the following subsections. Finally, as each fundamental interaction, the weak interaction is expressed via intermediate vector bosons, called $W^{\pm}$ and Z^0 experimentally discovered in 1982 [Arn+83]. The $W^{\pm}$ mediates the charged weak current and interactions while the Z^0 mediates the neutral weak ones.

i	O_i
S	1
V	γ^μ
T	$\sigma^{\mu\nu}$
A	$i\gamma^\mu\gamma^5$
P	γ^5

Table 3.5 – Table describing the value taken by O_i depending on which interaction is involved (see Sec. 3.3(d) of [Mui65]).

The Dirac gamma matrices listed in table3.5 obey the following relations:

$$\begin{aligned} \gamma^5 &= i\gamma^0\gamma^1\gamma^2\gamma^3 \\ \sigma^{\mu\nu} &= i(\gamma^\mu\gamma^\nu - \gamma^\nu\gamma^\mu)/2 \\ \gamma^\mu &= (\gamma^0, \vec{\gamma}) \\ \gamma^0 = \begin{pmatrix} I & 0 \\ 0 & -I \end{pmatrix}; &\gamma^i \begin{pmatrix} 0 & \sigma_i \\ -\sigma_i & 0 \end{pmatrix} \end{aligned} \tag{3.6}$$

with $i = 1, 2, 3$, σ_i the Pauli matrices, and I the identity matrix.

3.2.1 C, P and, T symmetries

This part will approach the notion of symmetries in order to be able to understand the follow-up development. The symmetries are deeply connected to the conservation laws in physics. This notion was first introduced by Emmy Noether with her known theorem [Noe71] which stipulates that for every continuous symmetry of a Lagrangian, there is a quantity that is conserved by its dynamics. In other words, if the lagrangian of a system does not

[4] A vector quantity will change sign when rotated over 180° but the sign will remain the same when rotated over 360°.

[5] An axial-vector quantity will change of sign just like the vector quantities but will not change the sign in case of an inversion of coordinates. For example, any object resulting from a cross-product of two vectors will be an axial vector. The angular momentum is a typical notion of an axial vector.

[6] A pseudo-scalar quantity behaves like a scalar but it will flip the sign when inverting the space coordinate. The helicity is a pseudo-scalar quantity since the momentum will be flipped whereas the spin direction is not.

change under transformation, it implies that there exists a quantity that is conserved. In physics, there are two kinds of symmetries: discrete and continuous.

3.2.1.1 Continuous symmetries

The continuous transformations can be made by applying successively an infinitesimal transformation operator. Space-time symmetries are typical continuous symmetries and, concerning the space parts, this regroups rotation and translation in space.

Space translation:
To a system placed at the $\vec{r}$ position, any translation in space made to this system gives a new position such as $\vec{r} \longrightarrow \vec{r} + d\vec{r}$. A system invariant under space translation means that the system is conserving a quantity regardless of which space translation has been carried out. A typical example of this conserved quantity under space translation is momentum.

Space rotation:
This illustrates the same principle as described above but with rotation. A typical example of this conserved quantity under space rotation is angular momentum.

Time translation:
This is the analogue of the space translation symmetry. A translation in time is made to a system at a time t meaning the system is now at a time $t + dt$, thus conserving a quantity if invariant under time translation. A typical example is the conservation of energy in such translation.
The discrete symmetries C, P, and T play an important role in the framework of weak interaction studies.

3.2.1.2 Discrete symmetries

Contrary to the continuous symmetry above, discrete symmetries, also called improper symmetries can not be described by a succession of infinite small transformations. The discrete symmetries have the original properties to transform a system to the exact same state by applying twice an operator. The major discrete symmetries are charge conjugation, parity and, time reversal and are developed below.

3.2.1.2.1 Charge

The charge conjugation, referred to as C, is the operation of interchanging a particle with its anti-particle. It is, of course, only conserved if the particle and anti-particle possess the same properties meaning a collision between a proton and a neutron or a collision between an anti-proton and an anti-neutron should behave the same. Applied to the general Hamiltonian

described in eq.3.5, the charge transformation gives [Lié10]:

$$\begin{aligned} H^C &= \sum_i \int d\vec{r}[\bar{\psi_n}(x)O_i\psi_p(x)][C_i\bar{\psi_\nu}(x)O_i\psi_e(x) + C_i^{'}\bar{\psi_\nu}(x)\gamma^5 O_i\psi_e(x)] + h.c.^C \\ H^C &= \sum_i \int d\vec{r}[\bar{\psi_n}(x)O_i\psi_p(x)][C_i\bar{\psi_\nu}(x)O_i\psi_e(x) + C_i^{'}\bar{\psi_\nu}(x)\gamma^5 O_i\psi_e(x)] + \\ &\quad [\bar{\psi_p}(x)O_i\psi_n(x)][C_i^*\bar{\psi_e}(x)O_i\psi_\nu(x) - C_i^{'*}\bar{\psi_e}(x)O_i\gamma^5\psi_\nu(x)] \end{aligned} \tag{3.7}$$

Where $h.c.^C$ is the hermitian conjugate under the Charge transformation. There is thus, invariance under C if $C_i = C_i^*$ and $C_i^{'} = -C_i^{'*}$ meaning that C_i constants are real and $C_i^{'}$ are imaginary. If these conditions are fulfilled, the Hamiltonian in eq. 3.7 will be equal to the one described in eq. 3.5.

3.2.1.2.2 Parity

The parity transformation reverses the coordinates of a particle such as:

$$P\psi(\vec{r}) = \psi(-\vec{r}) \tag{3.8}$$

and

$$\begin{array}{rccc} \text{Time} & \text{t} & \longrightarrow & \text{t} \\ \text{Space} & \vec{x} & \longrightarrow & \text{-}\vec{x} \\ \text{Momentum} & \vec{p} & \longrightarrow & \text{-}\vec{p} \\ \text{Energy} & \text{E} & \longrightarrow & \text{E} \end{array}$$

As described in [Sev04], if the system stays invariant after the P transformation, it means that the probability density remains invariant, and since it is given by the square of the wave function, it leads to:

$$\psi(\vec{r})\psi(\vec{r}) = \psi(\vec{-r})\psi(\vec{-r}) \tag{3.9}$$

meaning,

$$\psi(\vec{r})) = \pm\psi(-\vec{r}) \tag{3.10}$$

hence,

$$P\psi(\vec{r}) = \pm\psi(\vec{r}) \tag{3.11}$$

This comes from the fact the Parity operator does not change the density probability, so if the system has to be invariant under P transformation then the wave function can either remain the same such as $P\psi = +\psi$, or may change sign such as $P\psi = -\psi$. In the former case, it is said to be an even parity state whereas in the latter state, it is said this is an odd parity state. Applied to the general Hamiltonian described in eq. 3.5, the parity transformation gives[Lié10]:

$$H^P = \sum_i \int d\vec{r}[\bar{\psi_p}(x^{'})O_i\psi_n(x^{'})][C_i\bar{\psi_e}(x^{'})O_i\psi_\nu(x^{'}) - C_i^{'}\bar{\psi_e}(x^{'})O_i\gamma^5\psi_\nu(x^{'})] + h.c.^P \tag{3.12}$$

The negative sign comes from the fact that[Lié10]:

$$\begin{gathered}\psi(x) \longrightarrow \psi^{'}(x^{'}) = \gamma^0\psi(x^{'}) \\ \text{and} \\ \bar{\psi}(x) \longrightarrow \bar{\psi}^{'}(x^{'}) = \bar{\psi}(x^{'})\gamma^0\end{gathered} \tag{3.13}$$

So,

$$\bar{\psi_e}(x)O_i\gamma^5\psi_\nu(x) \longrightarrow \bar{\psi_e}(x^{'})\gamma^0O_i\gamma^5\gamma^0\psi_\nu(x^{'}) = -\bar{\psi_e}(x^{'})\gamma^0O_i\gamma^0\gamma^5\psi_\nu(x^{'}), \tag{3.14}$$

The Eq. 3.14 can be explained by the anticommuting rule for γ matrices described as[Lié10]:

$$\begin{gathered}\gamma^\mu\gamma^\nu + \gamma^\nu\gamma^\mu = 2g^{\mu\nu} \\ \text{where} \quad g^{\mu\nu} = 1 \quad \text{if} \quad \mu = \nu = 0 \\ g^{\mu\nu} = -1 \quad \text{if} \quad \mu = \nu \neq 0 \\ g^{\mu\nu} = 0 \quad \text{if} \quad \mu \neq \nu\end{gathered} \tag{3.15}$$

where μ and ν can be equal to 0,1,2,3 or 5. Here, since the exponent of the gamma matrices are not similar $\gamma^5\gamma^0 = -\gamma^0\gamma^5$.

For this Hamiltonian to be invariant under P transformation, either C_i or $C_i^{'}$ have to be zero.

3.2.1.2.3 Time reversal

Last but not least, the time reversal operation leads to the reverse of the "film" of any physical system inducing the following changes:

$$\begin{array}{rccc}\text{Time} & \text{t} & \longrightarrow & \text{-t} \\ \text{Space} & \vec{x} & \longrightarrow & \vec{x} \\ \text{Momentum} & \vec{p} & \longrightarrow & \text{-}\vec{p} \\ \text{Energy} & \text{E} & \longrightarrow & \text{E}\end{array}$$

Symmetry under this transformation involves the physical system possessing the same properties as either a forward sequence of events or a backward one. This transformation is a bit difficult to handle. To illustrate that, we can take a look at the commutation relation between the position and the momentum:

$$[x_i, p_j] = i\hbar\delta_{ij} \tag{3.16}$$

By taking into account the T transformation, it gives:

$$[x_i, -p_j] = -i\hbar\delta_{ij} \tag{3.17}$$

This is an obvious example of non-invariance under a transformation. This issue can be solved if T does reverse the order of the operators[7]. This solution was first introduced by Wigner in 1932 [Wig32], and in 1951 by Schwinger [Sch51] with a different approach. The

[7]It is also called an anti-linear transformation.

idea behind this development is to employ an operator T, that once applied to a vector $|\psi\rangle$ transforms it to its dual $\langle\psi_T|$. T is thus acting as an anti-unitary transformation on a single operator and reverses the order of the operators, giving:

$$\begin{aligned} T\hat{x}T^{+} &= \hat{x} = \hat{x_T} \\ T\hat{p}T^{+} &= -\hat{p} = \hat{p_T} \end{aligned} \tag{3.18}$$

where $\hat{p}$ and $\hat{x}$ are respectively the momentum and position operators. We can then apply the last relation to Eq. 3.16, which leads to:

$$T[x_i, p_j]T^{+} = [p_{iT}, x_{iT}] = [-p_j, x_i] = [x_i, p_j] = i\hbar\delta_{ij} \tag{3.19}$$

Applied to the general Hamiltonian described in Eq.3.5, the time-reversal transformation gives [Lié10]:

$$H^T = \sum_i \int d\vec{r}[\bar{\psi_n}(x'')O_i^T\psi_p(x'')][C_i\bar{\psi_\nu}(x'')O_i^T\psi_e(x'') + C_i'\bar{\psi_\nu}(x'')(O_i\gamma^5)^T\psi_e(x'')] + h.c.^T \tag{3.20}$$

leading to the following form due to eq. 3.14:

$$H^T = \sum_i \int d\vec{r}[\bar{\psi_n}(x'')O_i\psi_p(x'')][C_i\bar{\psi_\nu}(x'')O_i\psi_e(x'') - C_i'\bar{\psi_\nu}(x'')\gamma^5O_i\psi_e(x'')] + h.c.^T \tag{3.21}$$

Finally, the Hamiltonian will be invariant under T transformation if $C_i = C_i^*$ and $C_i' = C_i'^*$, meaning that the coupling constants have to be real.

Given all the conditions of invariance, it results that the invariance under a discrete operation is automatically invariant under the product of the other two remaining ones, even though the individual transformations of this pair may not be non-invariant. This is known as the CPT theorem.

CPT theorem:

We have known since the '60s that the weak interaction violates both parity and charge conjugation as shown in [Wu+57]. Moreover, we also know that it violates the combined CP-symmetry [Chr+64]. However, the fact that under CPT transformation, meaning particle are becoming their anti-particles going backwards in time starting from their opposite coordinates, should resemble the original process seems reasonable.

This CPT theorem also involves several things regarding the previous statement especially that particles should have the same mass and lifetime as their anti-particle. By the same process, a violation of symmetry or a pair of symmetries involves the fact that the remaining operations should be broken to ensure exact symmetry under CPT. Finally, this theorem forms a requirement of every Quantum Field Theory (QFT).

3.2.2 Hamiltonian of the SM

By taking into account all the invariances of the discrete symmetries detailed above, some constraints are imposed on the coupling constants.

- $C_T^{'} = C_S^{'} = 0$ and $C_A/C_V < 0$ are fixed by the V-A theory.
- C_i and $C_i^{'}$ are real due to time reversal invariance.
- $C_i^{'} = C_i$ due to maximum violation of Parity.

The V-A theory comes from the fact that, experimentally, the scalar and tensor currents are small leading to a theory in which $C_T = C_S = 0$ and $C_A/C_V < 0$. S and V interactions lead to the Fermi transition whereas A and T lead to the Gamow-Teller transitions, whereas C_P are neglected for a non-relativistic description of nucleons. The latter statement involves that the matrix element for transitions from an initial state to a final state can only be described by Vector and Axial-Vector currents. Furthermore, they both are associated with different types of transitions, such as Gamow-Teller transitions for Axial-Vector, since it allow a spin change, and Fermi transitions for Vector couplings since they do not provide a spin change. The second constraint says that in the absence of time reversal violation, these coupling constants are real. Then, the maximal violation of parity, which has been explored experimentally by the Wu experiment, developed in the following section, imposes the third constraint. Finally, from the general Hamiltonian of the beta decay described in 3.5, we end up with the Hamiltonian of the beta decay in the framework of the Standard Model:

$$H_{MS} = \int d\vec{r}[\bar{\psi_p}(x)\gamma^\mu(C_V + C_A\gamma^5)\psi_n(x)][\bar{\psi_e}(x)\gamma^\mu(1-\gamma^5)\psi_\nu(x)] + h.c. \tag{3.22}$$

3.2.3 The Wu experiment

In the 50s, the idea that all interactions are invariant under spatial inversion was widely accepted. However, one problem remained unexplained. Also known as the τ-θ puzzle, this problem consisted in the fact that τ and θ mesons were originally thought of as two distinct particles, disintegrating by weak interactions into pions (π), such as:

$$\begin{aligned} \tau &\longrightarrow \pi^+\pi^+\pi^-, \\ \theta &\longrightarrow \pi^\pm\pi^0 \end{aligned} \tag{3.23}$$

However, since the pion has a spin-parity of 0^-, the θ meson must have a spin-parity of $0,^+1,^-2^+$ etc, if the decay was to maintain parity. The spin-parity of the τ meson was determined and it appears to be 0^- meaning that τ and θ appeared to be different particles. However, experimentally, it appeared that the lifetime and mass of both τ and θ mesons were equal according to the error bars.

At the end of the '50s, Lee and Yang were suggesting that the τ and θ were just different decay modes of the same particle, called the K mesons, with the assumption of non-conservation of that parity in weak interactions. Later after this statement, they proposed

a number of experiments that aimed to probe potential parity violation processes [LY56] in the weak interaction. They stated that in the beta decay of oriented nuclei, an asymmetry of counts regarding the direction of polarisation would immediately indicate that there is a parity violation.

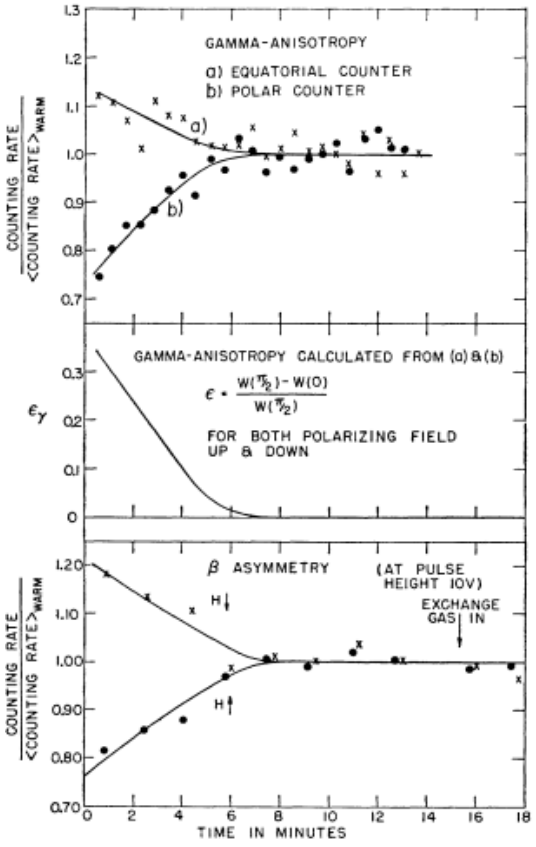

Figure 3.1 – Gamma and beta asymmetry for different configurations of polarizing field versus the time for polarizing [Wu+57].

An experiment based on the same principle has then been conducted by Wu, Ambler, Hayward, Hoppes, and Hudson [Wu+57]. This experiment, published in 1957, is based on the oriented decay of the ^{60}Co. The radioactive sample is placed on a thin surface on top of a crystal of Cerium Magnesium nitrate. The radioactive sample is cooled, thanks to a cryostat to near 0 K temperature in order to prevent thermal motions from ruining the spin alignment. This latter notion is done thanks to high magnetic fields. The beta detector consists of an anthracene crystal and is placed just above the radioactive sample, meanwhile, the polarization is measured with the help of two NaI gamma scintillation counters. One is placed perpendicular to the radioactive layer at the equatorial plane and the other one is placed behind the sample, at 10 cm from the symmetry axis. The polarization is measured as the anisotropy of counts in the gamma detectors. This leads to a large beta asymmetry as shown in Fig. 3.1 coming from the original publication of the results. The asymmetry then fades away at around 6 minutes corresponding to the moment when the warm-up kicks in. The polarization then no longer exists. The sign of the asymmetry coefficient is found to be negative meaning the beta emission is favoured in the direction opposite of the nuclear

spin.

A confirmation of this effect has been done by not polarising the cobalt sample and no asymmetry has been seen. This experiment marks the first step of the symmetry violation experiments in nuclear beta decay.

3.2.4 Sakharov Conditions

The fact that we humans are living on a planet and observing the universe around us is possible by living in a world of matter. Since the discovery of antimatter, we can ask ourselves why, at the beginning of the universe, where *a priori* an equal quantity of matter and antimatter was produced, matter/antimatter were not annihilated. To answer that question, Andreï Sakharov proposed ten years after the Wu experiment, three conditions that are necessary to fulfil in order to explain the matter-antimatter imbalance in the universe [Sak91]. Even though those conditions are not necessarily detailed in this three-page original paper, especially the third one, we will try our best to make them understandable. These conditions are the following:

- A violation of the baryonic number
- A large C and CP violation
- Interactions out of thermal equilibrium

Here the first and the third points can be explained together, leading to explaining the second point first.

1. (see third point)
2. Then the C-symmetry (see Sec.3.2.1.2.1) must be violated to make sure the interaction producing more baryons than anti-baryons is not compensated by the charge symmetry. If the parity is not violated, the spin projection on the momentum direction will be inverted, leading to an equilibrium of left-handed baryons and right-handed anti-baryons. This is why the combination of C and P symmetries has to be broken.
3. This item focuses on the baryonic number, hence the following definition:
   The baryonic number which can be expressed as:

$$B = \frac{1}{3}(n_q - n_{\bar{q}}), \tag{3.24}$$

   with n_q the number of quarks and $n_{\bar{q}}$, the number of anti-quarks. In the early stages of the universe, where interactions were at equilibrium, one can say that the baryonic number was equal to zero. Thus a baryon number violation has to occur at some point, in order to not create a universe full of gammas.

   Then, the non-equilibrium part comes into play, as described in [Cli06] by considering a counter-example. By taking a hypothetical event **at** thermal equilibrium such as:

$$X \longrightarrow Y + B, \tag{3.25}$$

with X and Y respectively initial and final states with a B = 0 and with B representing the excess of baryon number produced, this process can be reverted at thermal equilibrium giving:

$$Y + B \longrightarrow X \tag{3.26}$$

Since no excess of baryonic number can arise from this hypothetical event, to observe a baryon excess this event has to happen away from thermal equilibrium.

3.2.5 Beta-decay correlations

The conditions outlined in the previous paragraph are the starting point of the search for new physics, i.e., physics beyond the standard model. For the following study, we will focus on CP-violation studies, meaning that, one has to find an observable that is sensitive to CP-violation. Within nuclear beta decay, one has to look to the expression developed by Jackson *et al.*[JTW57]. This expression comes from the Fermi golden rule which allows to directly calculate the decay probability per unit of time:

$$\lambda = \frac{2\pi}{\hbar}|V_{fi}|^2\frac{dN}{dE_0} \tag{3.27}$$

with V_{fi} the transition matrix element between the initial and final state and $\frac{dN}{dE_0}$ the density of accessible final states per unit of energy. The decay probability per unit of time for a given state of the daughter nucleus with a given electron momentum and angle gives according to [Lié10]:

$$d\lambda = \frac{2\pi}{\hbar}|V_{fi}|^2 d\left(\frac{dN}{dE_0}\right) = \frac{4\pi^2}{h}|V_{fi}|^2\left(\frac{2\pi V^2}{c^3h^6}p_e^2(E_0 - E_e)^2\sin(\theta)dp_e d\theta d\Omega_e\right) \tag{3.28}$$

$$d\lambda = \frac{8\pi^3 V^2}{c^3h^7}|V_{fi}|^2 p_e^2(E_0 - E_e)^2\sin(\theta)dp_e d\theta d\Omega_e \tag{3.29}$$

Finally, the angular correlations in β decay depend on the coupling constants C_i and C_i' due to the couplings of V,S,T and A interactions. Thus, the distribution of the electron and neutrino directions and the energy of allowed beta transitions for oriented nuclei is given by Eq. 3.30. Passing from the expression 3.29 to 3.30 is not a trivial step and relies upon the development of $|V_{fi}| =< f|H|i >$. This expression is constrained with some approximations such as the non-relativistic one[8] for example and we end up with the expected number of decays $N(p_e, \theta)$ with an electron with p_e for a neutrino angle of emission θ. This has been done in deep detail in [Lié10] in a specific case and thus will not be explored here. A complete investigation was proposed by Jackson et al.[JTW57], which led to the following expression:

[8] Only valid for nuclei or nucleons.

$$w(<\vec{J}>|E_e,\Omega_e,\Omega_\nu)dE_e d\Omega_e d\Omega_\nu = \frac{F(\pm Z,E_e)}{(2\pi)^5} p_e E_e (E_0-E_e)^2 dE_e d\Omega_e d\Omega_\nu \times \frac{1}{2}\xi\left[1 + a_{\beta\nu}\frac{\vec{p_e}\vec{p_\nu}}{E_e E_\nu} + b\frac{m}{E_e} + \frac{<\vec{J}>}{J}.\left(A_\beta\frac{\vec{p_e}}{E_e} + B_\nu\frac{\vec{p_\nu}}{E_\nu} + D.\frac{\vec{p_e}\times\vec{p_\nu}}{E_e E_\nu}\right)\right] \quad (3.30)$$

with E_e, p_e and Ω_e the total energy, the momentum, and the angular coordinate of the beta particle, whereas E_ν, p_ν, and Ω_ν are equivalent for the neutrinos. The F$(\pm Z, E_e)$ function is the Fermi function that contains the dominant Coulomb correction, and $<\vec{J}>$ is the nuclear polarisation of the parent nucleus with J the total angular momentum. E_0 is the total energy at the spectrum endpoint whereas ξ is defined just below (see Eq. 3.32). Finally, $a_{\beta\nu}$ the $\beta-\nu$ angular correlation, b the Fierz interference term, A_β the β asymmetry, B_ν the neutrino asymmetry, and D are coupling constants depending on pure Fermi and Gamow-Teller matrix elements but also on coupling constants $C_i^{(\prime)}$. Measuring those correlation parameters helps to constrain the coupling constants or to check violation of symmetries. Such measurements appear to be stringent tests of the SM itself.

That is why, with the MORA experiment, we aim to measure the D triple correlation parameter, the value of which is supposed to be zero according to the Standard Model. D is a very interesting parameter since by looking at the general expression for the nuclear beta rate "w", given by equation 3.30, one can see that the triple correlation is T-odd under time reversal transformation. Indeed, the sign flip of the momenta compensates itself due to the cross product, however, the sign flip of the parent nucleus spin contributes to the oddness of the expression.

Since $D \neq 0$ violates the T symmetry, it also violates the CP-symmetry according to the CPT theorem, making it a good candidate to probe New Physics. This will be developed in the following section.

3.2.6 D parameter

To be able to probe the D parameter, one has to know to what D is sensitive. This parameter has been described in [JTW57] and it can be expressed as:

$$D\xi = 2Im\{\delta_{J'J}|M_F||M_{GT}|\left(\frac{J}{J+1}\right)^{1/2}(C_S C_T^* - C_V C_A^* + C_S^{\prime} C_T^{\prime *} - C_V^{\prime} C_A^{\prime *})\}, \quad (3.31)$$

with:

$$\xi = |M_F|^2(|C_S|^2 + |C_V|^2 + |C_S^{\prime}|^2 + |C_V^{\prime}|^2) + |M_{GT}|^2(|C_T|^2 + |C_A|^2 + |C_T^{\prime}|^2 + |C_A^{\prime}|^2) \quad (3.32)$$

According to both Eq. 3.31 and Eq. 3.32, D is sensitive to both Fermi and Gamow-Teller matrix elements. This involves a constraint on the polarized nuclei used. Indeed, it implies the fact that the nuclear transition has to contain both types of transition and the typical candidates from such mixed transitions are mirror nuclei and neutrons.
D can then be reduced to the following form by neglecting the second order $|C_S|$ and $|C_T|$

terms and considering $C_A = C'_A$ and $C_V = C'_V$ [JTW57].

$$D \equiv -2Im(C_V C_A^*)\frac{|M_{GT}||M_F|}{C_V^2|M_F|^2 + C_A^2|M_{GT}|^2} \times \left(\frac{J}{J+1}\right)^{1/2} \tag{3.33}$$

$$D \equiv Im(C_V C_A^*)\frac{1}{|C_A||C_V|} \times \frac{-2\rho}{(1+\rho^2)}\left(\frac{J}{J+1}\right)^{1/2} \tag{3.34}$$

with $\rho = \frac{C_A M_{GT}}{C_V M_F}$. Two parts compose this expression. The first part, which contains the left part of the Eq. 3.34, is the one which is CP-violating. Indeed, as seen earlier, the time reversal invariance implies that the coupling constants are real and thus having a non-zero imaginary part would indicate a time reversal violation hence a CP violation. The rest of the expression, containing ρ and J is the sensitivity factor, also known as F(X)[9], which depends on the characteristics of the beta decay, leading to different values regrouped in the Table[10] 3.6.

Intuitively, one would seek the higher sensitivity factor, either positive or negative. Concerning MORA, two nuclei are chosen: the ^{23}Mg and ^{39}Ca. Even though both of these nuclei are the most sensitive, the hyperfine structure of these nuclei has to be accessible **and**, one has to able to produce these nuclei.

System	***Sensitivity factor***
n	0.43
^{19}Ne	-0.52
^{23}Mg	-0.65
^{35}Ar	0.41
^{39}Ca	0.71

Table 3.6 – Value coming from [Del20].

Another way to probe D stands on the fact that the Colombian interaction between the daughter nucleus and the beta particle mimics a parameter equivalent to D: D_{FSI} where the subscript FSI stands for "Final State Interactions". This factor, expressed in [CT67] is detailed in Eq. 3.35 considering two contributions:

- The recoil effect due to the electron scattering by the nuclear moment giving to D_{FSI} a contribution of the order of $\frac{Z\alpha E_e}{M}$;
- The recoil effect due to the structure of the beta decay interaction, the main of which contribution comes from the weak magnetism term on the conserved-vector-current hypothesis [FG58]. This leads to the following expression of $D_{FSI} \sim Z\alpha\frac{E_e}{M}.A(\mu_f - \mu_i)$;

Where Z is the atomic number of the daughter nucleus, α the fine structure constant, E_e the total energy of the electron, M the average mass between the daughter and mother nuclei and A is the atomic mass of the nuclei of interest. Finally μ_f and μ_i represent the

[9] Here X represents the chosen system: nucleus or neutron.
[10] This list is obviously not exhaustive.

nuclear magnetic moment of the daughter and mother nuclei respectively. This calculation generates a correlation D_{FSI} which depends on the electron momentum [Del20] as shown in 3.35.

$$D_{FSI}(\beta^{\mp}) = f_1(\beta^{\mp})\frac{p_e}{p_{max}} + f_2(\beta^{\mp})\frac{p_{max}}{p_e} \tag{3.35}$$

With $f_1(\beta^{\mp}, J) = a(\beta^{\mp})b(\beta^{\mp}, J)p_{max}$ and $f_2(\beta^{\mp}, J) = \frac{(m_e c^2)^2}{p_{max}}a(\beta^{\mp})c(\beta^{\mp}, J)$. The values of a, b and c are depending on the nuclear spin value.
For both ^{23}Mg and ^{39}Ca, our nuclei of interest for MORA, the nuclear spin value is 3/2, giving the final table:

System	***J***	$f_1(\beta^{\mp}, J) \times 10^{-4}$	$f_2(\beta^{\mp}, J) \times 10^{-5}$	$D_{FSI}(p_e = p_{max}) \times 10^{-4}$
n	1/2	0.11	0.23	0.13
^{19}Ne	1/2	2.30	1.70	2.50
^{23}Mg	3/2	1.80	0.96	1.90
^{39}Ca	3/2	-0.47	-0.24	-0.49

Table 3.7 – Values coming from [Del20].

Finally, measuring D in the ^{23}Mg decay with MORA would allow for the first time the test of the theoretical hypothesis, used to calculate D_{FSI}.

Theoretical predictions: In a recent article by Adam Falkowsky et al.[FR22], a review of different scenarios led to a value of D. Knowing that experimentally, the sensitivity limit has so far been measured at 10^{-4} (see 3.3), this review explores the sensitivity limits with different theoretical scenarios. In these CP-violating EFT-based scenarios, a shift ΔD of the D parameter away from the SM prediction is predicted to be $\Delta D \gtrsim 10^{-5}$ which starts to be conflicted with the already existing experimental data. Another approach has been made based on BSM scenario involving leptoquarks[11] leading to $\Delta D \lesssim 8 \times 10^{-6}$ for ^{23}Mg, which is way below the expected sensitivity aimed by MORA. This study ends with the perspective of probing D by looking at CP-conserving scalar and tensor current, since they are supposed to be null within the constraints of the SM. This leads to $\Delta D \sim 10^{-5}$ for ^{23}Mg. This level of precision has then to be reduced in the measurement of D in nuclear β decays.

In the following section, we will review former experiments aiming to probe CP-violating processes and historical experiments aiming to measure the triple correlation parameter.

3.3 State of the art of the D measurements

This section will review some of the low-energy experiments that tend to measure CP-violated interactions. Each will be shortly reviewed presenting the idea behind it and the main results. Finally, the MORA experiment will be presented.

[11] Leptoquarks are hypothetical bosons which interact with both leptons and quarks.

3.3.1 ^{19}Ne disintegration

The experiment described in [Hal+84] has been performed at the Princeton cyclotron. They have used an atomic beam of ^{19}Ne produced by a proton beam reaction on an SF_6 gaseous target. The main interest for such a target is first to produce the nucleus of interest but also to transport it to the next step of the polarized atomic beam production. The neon is then driven to the magnet chamber where the atoms are split in two nuclear magnetic substates, $m_j = \pm\frac{1}{2}$. The chosen state is selected with the help of a slit with 100% polarization. The nuclear spin is then aligned along the beam axis through the action of successive coils. The beam decays in a 20 cm long cylindrical cell with a 1 cm diameter.

Around this cell, four plastic scintillators detect the beta particles from the decay inside the cell as shown in Fig. 3.2. Meanwhile, the recoil ion ($^{19}F^-$) is accelerated along the cell

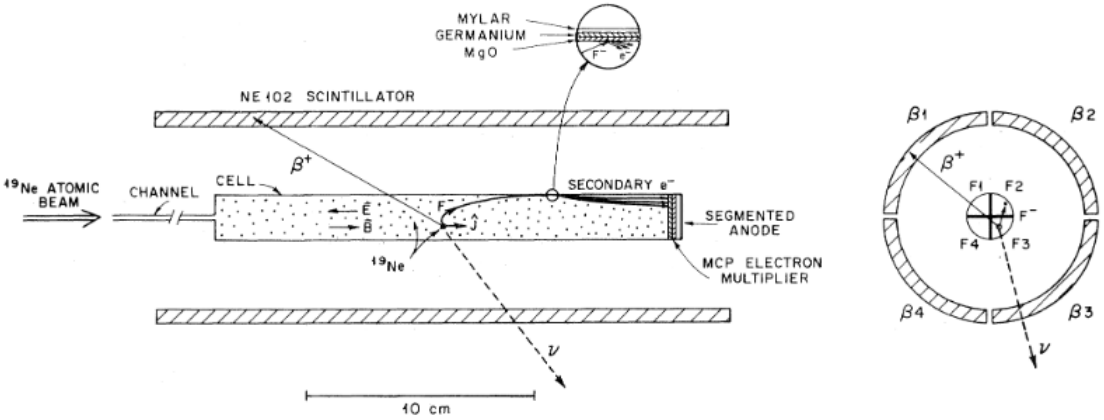

Figure 3.2 – Cross-section view of the experimental setup. The incoming polarised beam decays inside the cell. The figure on the right presents the detection set-up viewed from the z-axis.

with an electric field and hits the cell wall leading to the emission of secondary electrons. These electrons are gathered by an electron multiplier segment device which is separated into four parts. By detecting in coincidence the beta and the signal coming from the recoil ion, one can build an asymmetry such as:

$$R = \frac{N^{\uparrow}_{1,2}N^{\uparrow}_{2,3}N^{\uparrow}_{3,4}N^{\uparrow}_{4,1}N^{\downarrow}_{1,4}N^{\downarrow}_{2,1}N^{\downarrow}_{3,2}N^{\downarrow}_{4,3}}{N^{\downarrow}_{1,2}N^{\downarrow}_{2,3}N^{\downarrow}_{3,4}N^{\downarrow}_{4,1}N^{\uparrow}_{1,4}N^{\uparrow}_{2,1}N^{\uparrow}_{3,2}N^{\uparrow}_{4,3}}, \tag{3.36}$$

Where the arrow stands for the direction of the polarization, either parallel or antiparallel to the beam axis. $N_{i,j}$ refers to the number of beta-ion coincidences detected with a given polarization. Finally, the indexes i and j in the $N_{i,j}$ symbolize which detector has been hit, with i taking the index of the beta detector and j the recoil ions signal collectors. The D parameter can now be extracted from Eq. 3.36 by the following relation:

$$\Delta = \frac{1 - R^{1/8}}{1 + R^{1/8}} = DGWP, \tag{3.37}$$

where D is the triple correlation factor, G the average of the vector product $\vec{J}.\left(\frac{\vec{p_e}\times\vec{p_\nu}}{E_e E_\nu}\right)$ computed by a Monte-Carlo program, W represents a wash-out factor determined experi-

mentally[12], whereas P is the nuclear polarization. To conclude, by adding all the detector contributions, they have arrived at an estimation $D = (1. \pm 6.) \times 10^{-4}$.

3.3.2 TRINE

The TRINE experiment [Sol+04] consists of measuring the D parameter in the neutron decay. It has been carried out at the ILL cold neutron beam facility PF1. The detection set-up consists of four plastic scintillators ($560\times158\times8.5$ mm^3) that detect the electrons whereas the protons are detected by PIN diodes with a thin entrance window.

The detection process lies in the fact that the beam has two mirror planes ($x-z$ and $y-z$ for a beam along the z-axis). Thus, for each detector configuration, there exists every configuration due to the mirror reflections. Hence, the simplest case is just the detectors placed in an orthogonal position (protons detector face to face, same for the electron detector but with a 90° angle from the proton detector. D can then, be extracted from the events using Eq.3.38.

$$4P_z K_{D,z} D = \alpha^{00} - \alpha^{01} - \alpha^{10} + \alpha^{11} = \alpha_D, \tag{3.38}$$

with P_z the neutron polarization, $K_{D,z}$ a constant describing the sensitivity of the apparatus versus the D coefficient and α^{ij} quotient that can be written as $\alpha^{ij} = \frac{N^{ij}_{\uparrow} - N^{ij}_{\downarrow}}{N^{ij}_{\uparrow} + N^{ij}_{\downarrow}}$. Here N^{ij} describes the count rate of the detector combination $e^i p^j$ for a given spin direction. In total, it exists 16 cells that contain four detectors each. The neutron beam was polarized to P=0.974(26) with the help of a focusing super-mirror polarizer, the beam shape can be seen in Fig. 3.3. The direction of the neutron spin was flipped every 3 s by a resonance spin flipper. As a result, over 40 days of data have been taken, resulting in 3×10^7 events in total. Of this amount, 13.8×10^6 have been recorded in coincidence (between the proton and electron detector). This collection of data resulted in the determination of D as:

$$D = (-2.8 \pm 6.4^{stat} \pm 3.0^{syst}) \times 10^{-4}$$

Figure 3.3 – This figure, coming from the original paper, shows the beam shape along either the x or y-axis.

3.3.3 EMIT

The EMIT experiment [Mum+04] aimed to detect and measure in coincidence the so-called triple-correlation of the decay product of the polarized neutron decay. This measurement

[12]More details in [Hal+84]

was carried out at the NIST Center for Neutron Research (NCNR). The neutrons are polarized along the beam axis with the help of the spin flipper upstream of the detector area which is shown in Fig. 3.4. The spin alignment has an impact on the count rates due to

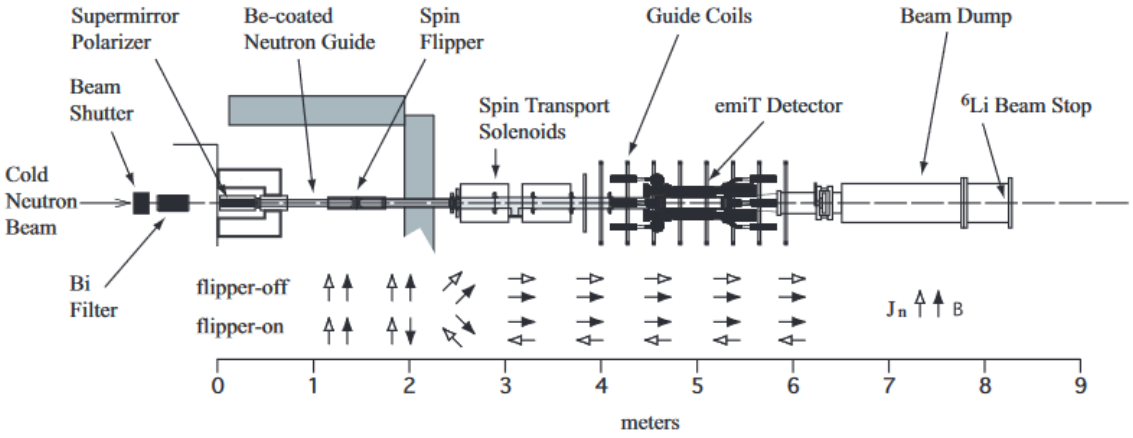

Figure 3.4 – Layout of the experiment line of the emiT experiment. As shown in the figure, the neutron spin is switching along the line, starting from the spin flipper. Depending on whether the spin flipper is running or not, the direction of the spin will be reversed.

the correlation of A, B, and D. To evaluate this neutron-spin dependent term, they have defined an asymmetry as:

$$w^{p_i e_j} = \frac{N_+^{p_i e_j} - N_-^{p_i e_j}}{N_+^{p_i e_j} + N_-^{p_i e_j}}, \tag{3.39}$$

with p_i representing the labels of the proton cells and e_j the electron detectors. The $\pm$, for its part, represents the spin-flipper states with neutrons either parallel or antiparallel to the magnetic field $\vec{B}$. The emiT experiment has dealt with systematic uncertainties, neutron transverse polarization in particular. This effect comes from a small misalignment of the magnetic field with respect to the detector axis. After correcting all the systematic effects,

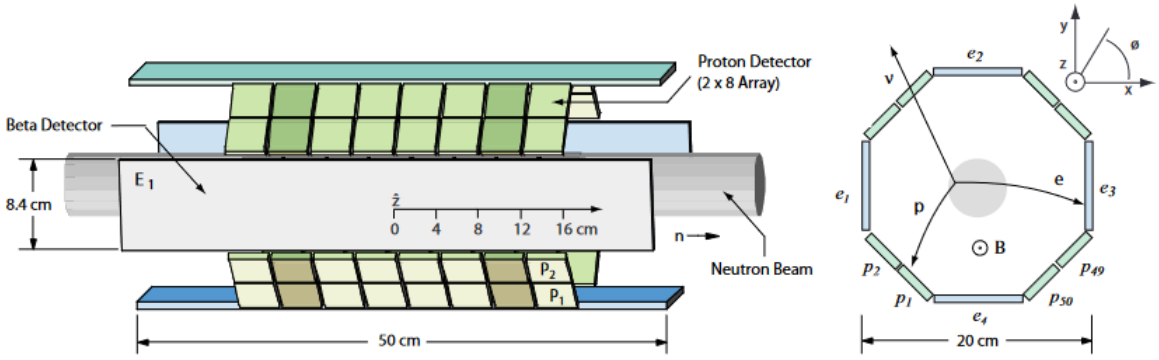

Figure 3.5 – The detection set-up of the emiT experiment. The left panel shows the proton detector which is made of 16 smaller cells each. The electron detector is placed between each proton detector and they measure 50 cm. The second panel shows the end view of the detectors with the magnetic field along the beam direction. The trajectories of the beta particles and the proton will be slightly curved which is greatly exaggerated in the picture.

they ended up with the most sensitive measurement of D in the nuclear beta decay of:

$$D = [-0.94 \pm 1.89(stat) \pm 0.97(sys)] \times 10^{-04} \tag{3.40}$$

This measurement has been done with an innovative detection set-up described in Fig.3.5 and where D has been determined by an asymmetry of counts in coincidence between beta particles and protons.

3.4 MORA

The MORA experiment [Del+19b] is the direct successor of the LPC Trap [Del+19a] experiment. As such, it takes part in the noble lineage of the precise measurement at low energy whose goal is to probe the Standard Model. Moreover, MORA aims to measure the so-called triple correlation D parameter, presented in Sec. 3.2.4. The experiment is a trap-based experiment, detailed in a dedicated section in Sec. 4.3. The trap is shown in Fig. 3.6a where one can distinguish it at the center of the picture.

The MORA apparatus has two parts: the injection line and the trap chamber. The commissioning of the experiment is detailed in the dedicated section 5. The experiment is based on the emiT experiment design (see Sec. 3.3.3), *i.e.* a different detector every 45°. The reason for that is related to the D correlation (see eq. 3.30): The scalar product between $\vec{J}$ and the cross-product of the momentum says that the correlation is maximum in a perpendicular plan according to the direction of $\vec{J}$. This imposes a constraint on the experimental detection system causing the detector to be arranged in this "crown" configuration.

The decays are recorded by the detectors (see 3.4.2) and one can build coincidences between the recoil ions and the beta in order to extract D from an asymmetry in the counting as described in Eq. 3.41, i.e.

$$\frac{N_{coinc}^{+45^\circ} + N_{coinc}^{+135^\circ} - N_{coinc}^{-45^\circ} - N_{coinc}^{-135^\circ}}{N_{coinc}^{+45^\circ} + N_{coinc}^{+135^\circ} - N_{coinc}^{-45^\circ} - N_{coinc}^{-135^\circ}} = \delta.D.P, \tag{3.41}$$

where δ represents the constant depending on the detection solid angle and decay parameters[13], D is the triple-correlation parameter and P is the polarisation parameter.

3.4.1 Polarization and magnetic field

The ion cloud is exposed to a laser beam in order to align the nuclear spin along the beam direction and this is discussed in Sec. 6.1.2. In order to populate those hyperfine sub-levels an external magnetic field is applied by Helmholtz coils placed outside the vacuum chamber. The magnetic field allows to maintain the cloud polarization, especially with a buffer gas configuration when successive collisions can depolarize the cloud.

[13] This parameter is known by Monte-Carlo simulations (see [Del+19b].

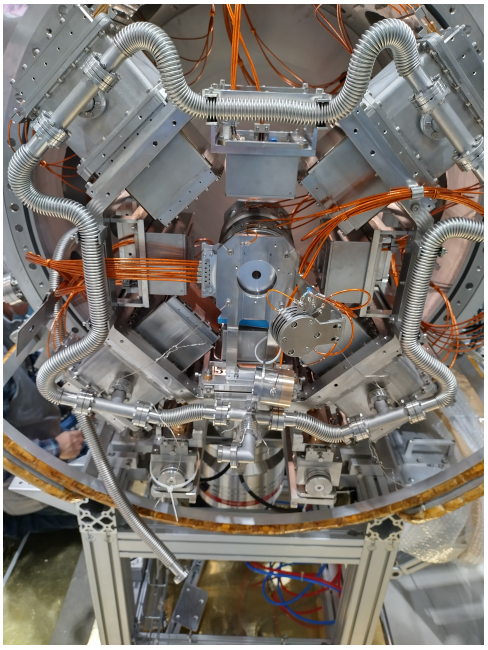

(a) The trap and detection system out of the chamber for cabling. One can see here the alternation of positions of the detectors. The RIDE are located at the cardinal positions while the phoswichs are located at the inter-cardinal positions. One can also note that a pumping circuit runs through the phoswiches. A primary vacuum is performed in the betas detectors to improve the chamber vacuum.

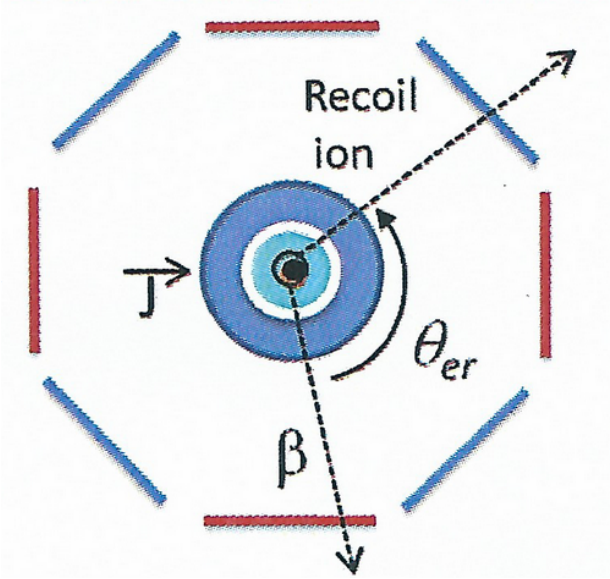

(b) Schematic view of the crown of detection. Beta detectors are shielded by a mylar sheet leading to be insensitive to the recoil ions.

Figure 3.6 – View of the trap and detector plan on the left and a schematic view on the right.

A diagnostic of the polarization degree can be performed by using this technique according to Eq. 3.42 in the next paragraph and also in the dedicated chapter (see Chap. 6). As mentioned previously, by knowing the polarization degree P one can access more directly the D parameter according to Eq. 3.41. Nevertheless, to be correctly polarized by the laser beam, the ions have to be properly confined and that is why we will use a Transparent Paul trap in the MORA experiment. The working principle of such a trap is discussed in Sec. 4.1.

3.4.2 Detectors

According to simulations, the results of which can be found in reference [Del+19b], the correlation D is maximum in a plane perpendicular to the spin direction. This same direction will be along the beam axis and so, the detectors are placed in a crown-shape configuration. The alternation between recoil ion detectors and beta detectors has been inspired by the EMIT experiment as mentioned, in Sec. 3.3.3.

Two kinds of detectors are used to measure D, one to detect the beta particle emitted, known as "phoswich" (see Chap. 7) and the other one is meant to detect, instead of neutrinos, the recoil ions, referred to as RIDE (Recoil Ion DEtectors). This is equivalent due to momentum conservation and, much more convenient polarising the cloud and so, orienting

it, we can detect coincidences between recoil ions and beta particles as described in the previous subsection. The laser apparatus will be described in Sec. 6.1.

Finally, an offline source can be inserted inside the trap with a mechanical system which can be seen in Fig. 3.7. This source is composed of an 8 mm stainless-steel octagon that can be removed or inserted mechanically from outside the chamber via a hand-wheel system. This system allows the source support "finger" to pass through the trap and the annular silicon detectors. The cylinder has one well containing a radioactive source every 45° for a source to face directly a silicon detector. This description is illustrated with the help of Fig. 3.7. On top of that, another well has been filled with a ^{90}Sr source at the tip of the cylinder, meaning this well is facing the Silicon detector which is closer to the entrance of the chamber.

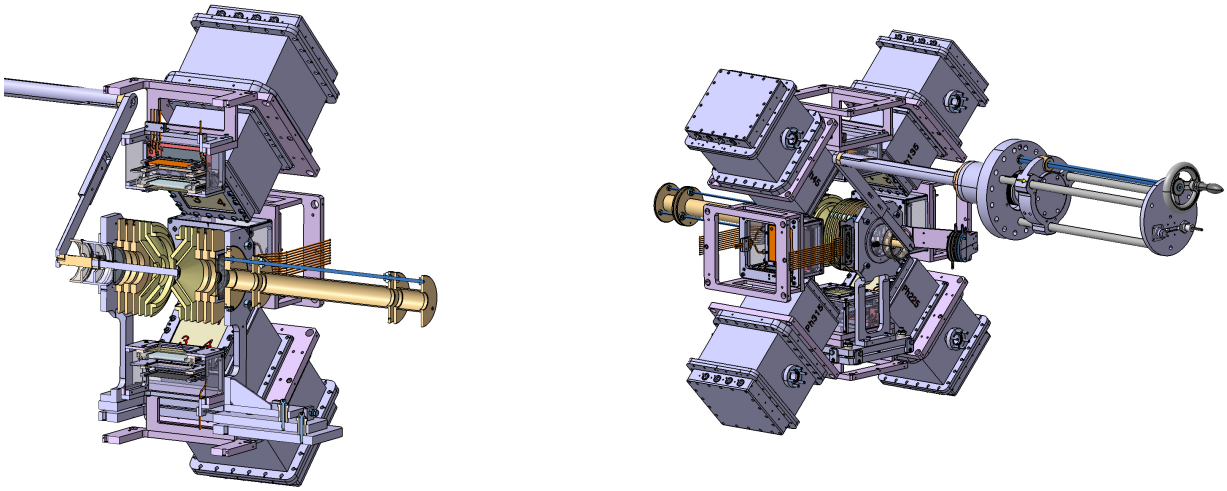

Figure 3.7 – Schematic cross section views of MORA chamber with the offline radioactive source finger inserted as seen from both sides.

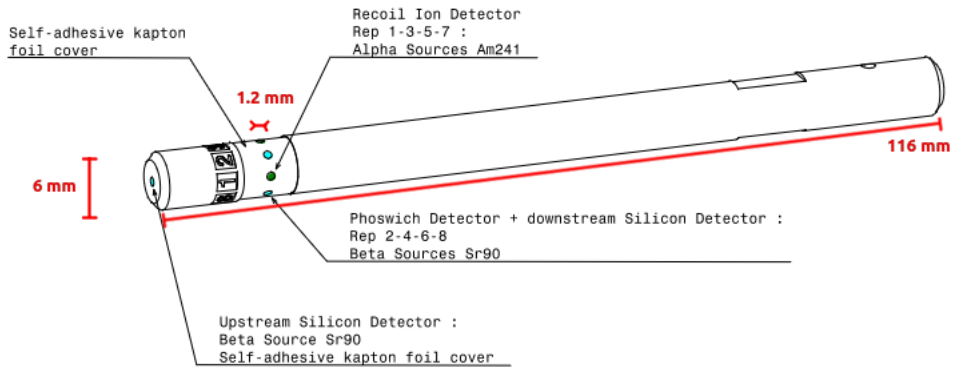

Figure 3.8 – Source finger detailed.

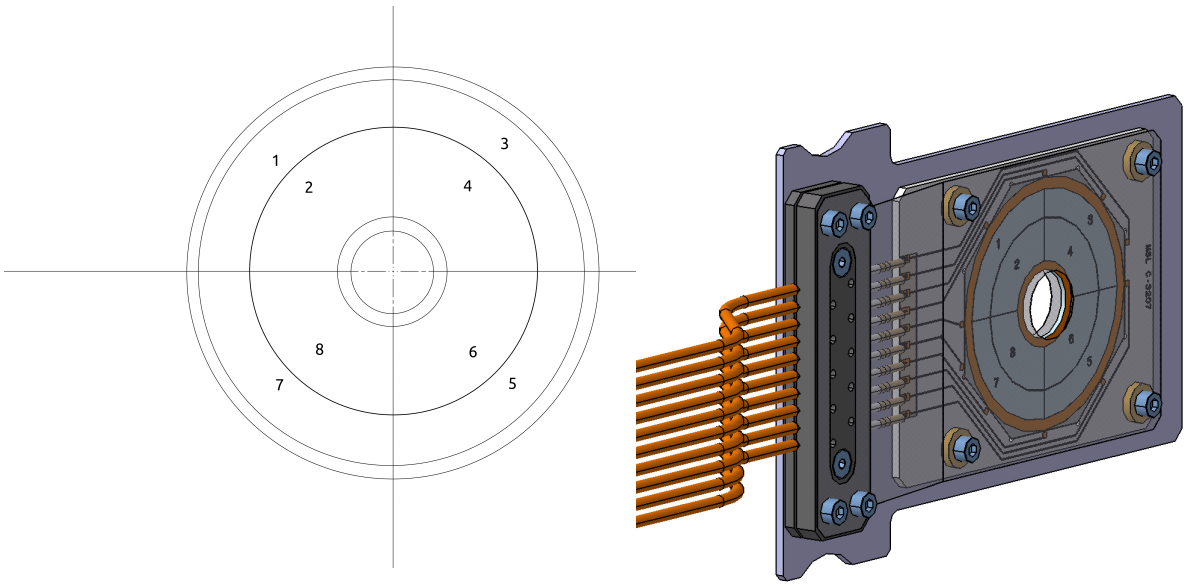

(a) Schematic view of the Si annular detector. The even sectors of the inside ring are the closest to the beam which can be noisier than the odd sectors.

(b) Representation of the Silicon detector wired.

Figure 3.9 – Scheme of the silicon detectors. They are placed on either side of the trap. Thanks to their annular properties, the beam can go through them without directly interacting with them.

Silicon detectors:

Placed along the beam axis, two silicon detectors aim to detect beta particles in order to measure the polarisation degree P (developed in the following dedicated section). After reverting the polarization by inserting or not the half-wave plate, the difference in counting between the two configurations gives:

$$\frac{N_{\beta+}^{\uparrow coinc} - N_{\beta+}^{\downarrow coinc}}{N_{\beta+}^{\uparrow coinc} + N_{\beta+}^{\downarrow coinc}} = (\alpha.A_\beta + \beta.B_\nu).\ P \tag{3.42}$$

where $N_{\beta+}^{\uparrow coinc}$ and $N_{\beta+}^{\downarrow coinc}$ are respectively the number of betas detected in coincidences with recoil ions and parallel to the polarization direction and number of betas detected in coincidences with recoil ions and anti-parallel to the polarization direction;
A_β being the beta asymmetry parameter, tabulated and known for ^{23}Mg: $-0.5541(20)$ [Sev+23] and $\beta.B_\nu$ the neutrino asymetry also known for he ^{23}Mg. A representation of the detector can be seen in Fig. 3.9.

Recoil Ion DEtectors (RIDEs):

The recoil ion detectors (see Fig. 3.11) are made of two micro-channel plates and a position-sensitive anode. The total active surface of the wafer is of dimension 48*48 mm^2, where each micro-channel has a diameter of 25 μm, with a 35 μm distance between adjacent channels. Each RIDE is composed of two MCPs, arranged in a chevron configuration (v-shape). This configuration allows the fact that each time an ion hits the front side of the MCP, it will trigger an electronic cascade which amplifies the signal by about 10^6 times

depending on the applied voltage. The MPCs are biased by a negative potential of 3900 V which is divided thanks to a divider bridge. This allows the MCPs to not suffer an excessive voltage (> to 2000 V) that could damage them. The electronic avalanche which leaves the MCP generates a positive signal on the backside of the MCP and a negative signal on the horizontal and vertical stripes of the position-sensitive anode. In total, five signals are coming from the RIDE detectors:

- One from the back of the MCP
- Four from the position-sensitive anode (one for each position up/left/down/right)

The position-sensitive anode was carefully calibrated [Goy23]. The calibration has been done with the help of a stainless-steel calibration mask where the pattern can be seen in Fig. 3.10. Once collected, the data from the detector are calibrated with the help of the ROOT analysis software. This operation is called "image reconstruction" and the idea of it is to make sure the mask's hole and the actual image correspond in terms of position. To do so, a first-order polynomial equation is applied to the data.

$$\bar{x}(mm) = a.\frac{Q_{right} - Q_{left}}{Q_{right} + Q_{left}} + b \tag{3.43}$$

$$\bar{y}(mm) = c \times \frac{Q_{top} - Q_{bottom}}{Q_{top} + Q_{bottom}} + d \tag{3.44}$$

Once the image is adjusted, one can perform a higher order polynomial correction described as:

$$\begin{aligned} X_c &= p_0 + p_1\bar{x} + p_2\bar{y} + p_3\bar{x}^2 + p_4\bar{y}^2 + p_5\bar{x}\bar{y} \\ Y_c &= q_0 + q_1\bar{x} + q_2\bar{y} + q_3\bar{x}^2 + q_4\bar{y}^2 + q_5\bar{x}\bar{y} \end{aligned} \tag{3.45}$$

with X_c and Y_c are the correction on the x and y axis respectively while p_i and q_i are coefficients.

Phoswich detectors:

The Phoswich detectors are made of two plastic scintillators of different thicknesses which are stuck together. They also have different time responses as shown in the dedicated section (see Chap. 7). Indeed:

- The thin scintillator is 0.5 mm and has a time response of 1.8 ns.
- The thick scintillator is 5 cm and has a time response of 285 ns.

The beta particles are detected in the two scintillators due to the energy loss in the material. For instance, a beta of 3 MeV, which is the maximal energy of the beta for the ^{23}Mg, it is stopped in 1.5 cm of plastic scintillator. These two scintillators are used for beta-gamma discrimination since the gamma particles are only detected by the thick scintillator (the probability of interaction in the thin scintillator is close to zero). Since the total charge is correlated with the two other charges a work of decorrelation has to be done which will be explained in detail in Chap. 7.

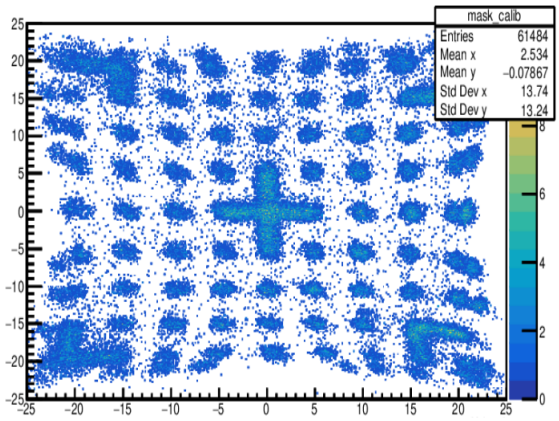

(a) Non-calibrated RIDE image constructed with four localisation charges coming from the position sensitive anode.

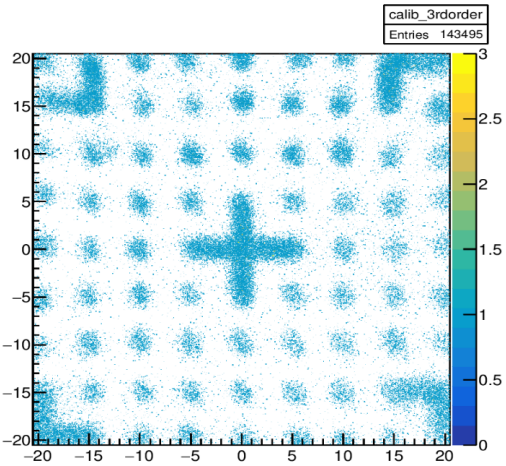

(b) Corrected RIDE image. This has been done with third-order correction.

Figure 3.10 – Calibration of the RIDE image, starting from Fig. 3.10a to Fig. 3.10b, both extracted to the upcoming article of the MORA experiment.

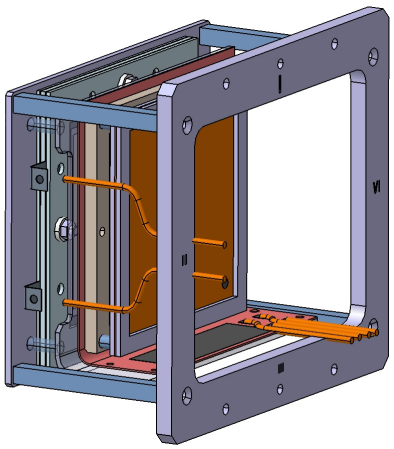

Figure 3.11 – Scheme of the RIDE detector where one can see the several layers of MCP and anode.

3.5 Conclusion

This section introduced the theoretical concepts to help understanding the context in which the MORA experiment takes place. Hence, the different kinds of particles and the fundamental interactions have been presented. The main model, the so-called Standard Model, has been explored including the symmetries. This constrains the general Hamiltonian of the beta decay to be invariant to some discrete symmetries. The Kaon's decay and later the Wu experiment have provided experimental proof of P-violation. This has led to the establishment of the three Sakharov conditions to explain the matter/antimatter asymmetry in the universe. One of them is a large CP violation and a non-zero value of the triple-correlation parameter D indicates a T-violation, so a CP-violation according to the CPT theorem. This parameter is thus really interesting and the state of the art of D-measurements has been described in the last part of this chapter. In this section, the measurement principle of the MORA experiment is introduced detailing the trap and detectors as well.

The next chapter will be very similar in structure but shorter. The presentation of theoretical notions used in trap-based experiments is done, leading to the example of the MORA trap itself. Finally, a table resuming the MORA trap properties is presented.

Chapter 4

The physics of trapping ions

This chapter aims to introduce theoretical concepts useful to understand the following chapters. Contrary to the previous chapter which is mainly focused on the physics of beta decay and the standard model, this one focuses more on the physics behind the experimental device. A complete introduction to Paul traps will be done, followed by a presentation of the ion polarization based on the reasoning in [MGW05] and [MV99], respectively. The last section deals with the presentation of the MORA experiment itself.

4.1 Paul traps

Invented in 1958 by Wolfgang Paul, the so-called Paul traps [PS53] distinguish themselves from the Penning trap [Deh68] thanks to their simple and elegant ease of use. Although the Paul trap and Penning trap share the common function of trapping charged particles with the help of electromagnetic fields, they differ in their principles. Indeed, Penning traps use static electric and magnetic fields whereas Paul traps only use radio-frequency (RF) electric fields in order to create a dynamical potential. The idea behind a three-dimensional Paul trap is rather simple. We want a minimum of potential energy at some region in the trap. The coulombian force, felt by the charged particles, will be applied toward the same region of minimal energy within the three directions of space. This can now be expressed as:

$$\vec{F} = -q\vec{\boldsymbol{\nabla}}V \tag{4.1}$$

where V is the potential energy and q the electric charge. Furthermore, according to the Laplace equation:

$$\nabla^2 V = \Delta V = 0 \tag{4.2}$$

giving a potential that can be expressed as:

$$V = V_0(Ax^2 + By^2 + Cz^2) \tag{4.3}$$

with V_0 a constant. The A, B, and C coefficients, however, have to satisfy the Laplace equation, *i.e* $A+B+C = 0$ meaning that a 3D trapping is impossible with static E fields. This leads to the following solutions:

- $A = -B$ for a linear Paul trap, also known as 2D Paul trap.

- $A = B, \quad C = -2B$ for an axisymmetric 3D Paul trap, which was originally called *Ionenkäfig* [POF58].

These solutions lead to the following form for the potential:

- $V = V_0(x^2 - y^2)$
- $V = V_0(x^2 + y^2 - 2z^2)$

The first case corresponds to trapping in a linear Paul trap (meaning that trapping is not possible along the z-axis), where the exit direction is along the y-axis. Since only two coordinates are involved, we can speak of radial confinement. The second case is obviously a 3D-trapping where the z-axis is the escape direction for the ion cloud.

A proper trapping is impossible, with an electro-static potential, because of the existence of an escape direction. The solution to solve this issue will be approached in the following subsections where both linear and 3D Paul traps will be presented.

4.1.1 2D or linear Paul Traps

For linear Paul traps such as a Radio Frequency Quadrupole trap, the typical potential created by the infinite hyperbolic electrode is defined as:

$$V(x, y) \; = \; \frac{V_0}{2}\left(\frac{x^2 - y^2}{2r_0^2}\right) \tag{4.4}$$

with r_0, the minimal distance from the center of the trap and the surface of the electrode, and V_0 the amplitude of the RF voltage. Since we are only limited by two directions, to be

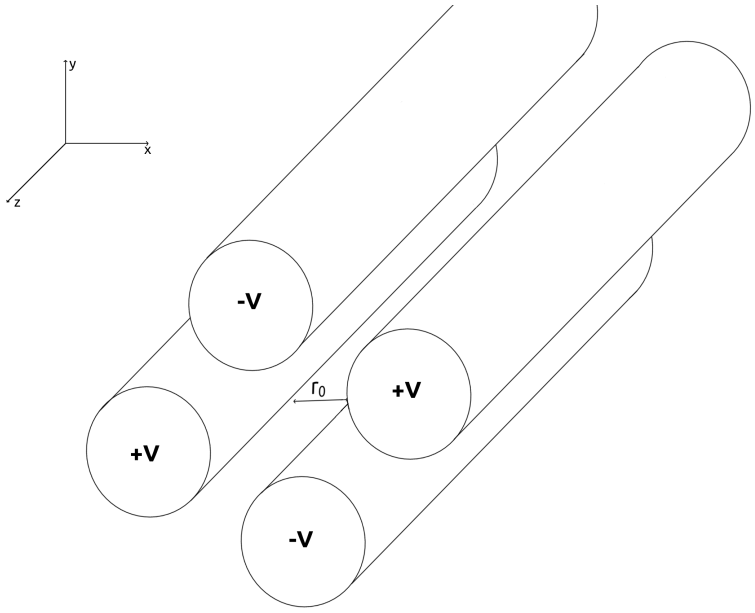

Figure 4.1 – Schematic cross-section of a linear Paul trap made of four rodes. This scheme has been inspired from [Mer07].

able to trap we have to add an oscillating term that will alternate the escape direction with time. The typical oscillating potential then looks like this:

$$V(x,y) = (U_0 - V_0 cos(\Omega t)) \left(\frac{x^2 - y^2}{2r_0^2} \right) \tag{4.5}$$

where U_0 is the amplitude of the static component, and $\Omega = 2\pi f_{RF}$ is the pulsation where f_{RF} is the RF frequency. The equations of motion in such a linear trap can be written as:

$$\begin{array}{rcl} m\frac{d^2x}{dt^2} & = & -q(U_0 - V_0 cos(\Omega t)\frac{x}{r_0^2} \\ m\frac{d^2y}{dt^2} & = & -q(U_0 - V_0 cos(\Omega t)\frac{y}{r_0^2} \end{array} \tag{4.6}$$

In order to simplify these equations of motion, we introduce the Mathieu parameters [MT89]:

$$a_r = \frac{4qU_0}{mr_0^2\Omega^2},\ q_r = \frac{2qV_0}{mr_0^2\Omega^2}. \tag{4.7}$$

These parameters can be used for creating constraints on the trapping process by plotting a_r in function of q_r. These so-called stability zones are detailed in the following section.

4.1.2 3D Paul Traps

For a 3D Paul traps, such as the MORA one, since another dimension is added, the mathematical formalism is a bit more complex. If we start from the Eq. 4.3, the solution for which each coefficient is zero is trivial and will not be considered. However, for 3D Paul trap, it leads to A + B = -C which gives the following form to Eq. 4.3:

$$V = V_0(x^2 + y^2 - 2z^2) = V_0(r^2 - 2z^2) \tag{4.8}$$

with $r^2 = x^2 + y^2$, the square of the radius in cylindrical coordinates. In 3D Paul traps, the potential looks like a saddle. It is characterized by the fact that whenever a coordinate is minimal (either r or z), the other is maximal, leading to privileged exit directions. Indeed, according to Earnshaw's theorem for a static potential, if a charged particle is placed on the spot where the field lines are diverging then no stable equilibrium and *de facto* no trapping can exist. A solution can still be established thanks to the radio-frequency (RF) potential. The alternation between the positive and negative values of the quadrupolar potential will rotate the direction of the saddle, inverting the escape direction as shown in Fig. 4.2. As a result, by applying the correct frequency and voltage amplitude, the ions will still make small oscillations but they will remain in the saddle origin. The typical quadrupolar potential can be written as:

$$V(x,y,z,t) = (U_0 + \ V_0 \ cos(\Omega t)) \ \frac{x^2 + y^2 - 2z^2}{2r_0^2} \tag{4.9}$$

The equations of motion in such a potential for an ion of mass m and charge e:

$$\frac{e}{m}\vec{E} = \frac{d^2\vec{r}}{dt^2} \tag{4.10}$$

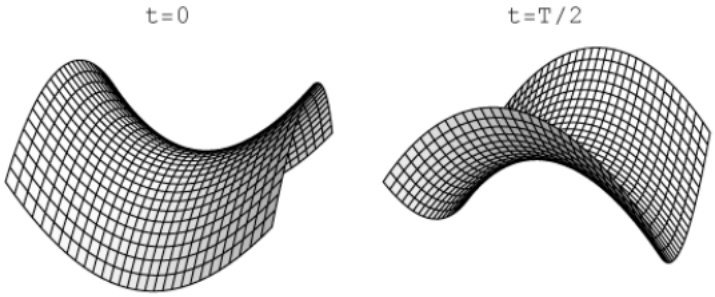

Figure 4.2 – Saddle shaped potential taken from Charged Particles Traps [MGW05] book. One can clearly see the alternation of the shapes as a function of time.

With Eq. 4.1, we can transform Eq. 4.9 to:

$$\frac{d^2\vec{r}}{dt^2} = \frac{e}{mr_0^2}[(U_0 + V_0 cos(\Omega t))(\vec{x} + \vec{y} - 2\vec{z})] \tag{4.11}$$

Changing t into $\tau = \frac{\Omega t}{2}$, $dt = \frac{2}{\Omega}d\tau$, allows simplifying the equation to:

$$\begin{aligned}
\tfrac{d^2x}{d\tau^2} \times \tfrac{\Omega^2}{4} - \tfrac{e}{mr_0^2}[(U_0 + V_0 cos(2\tau))]x &= 0 \text{ which becomes } \tfrac{d^2x}{d\tau^2} - \tfrac{4}{\Omega^2} \times \tfrac{e}{mr_0^2}[(U_0 + V_0 cos(2\tau))]x = 0 \\
\tfrac{d^2y}{d\tau^2} \times \tfrac{\Omega^2}{4} - \tfrac{e}{mr_0^2}[(U_0 + V_0 cos(2\tau))]y &= 0 \text{ which becomes } \tfrac{d^2y}{d\tau^2} - \tfrac{4}{\Omega^2} \times \tfrac{e}{mr_0^2}[(U_0 + V_0 cos(2\tau))]y = 0 \\
\tfrac{d^2z}{d\tau^2} \times \tfrac{\Omega^2}{4} + \tfrac{2e}{mr_0^2}[U_0 + V_0 cos(2\tau)]z &= 0 \text{ which becomes } \tfrac{d^2z}{d\tau^2} + \tfrac{4}{\Omega^2} \times \tfrac{2e}{mr_0^2}[U_0 + V_0 cos(2\tau)]z = 0
\end{aligned} \tag{4.12}$$

and introducing the Mathieu parameters:

$$a_x = a_y = -\frac{a_z}{2};\ a_z = \frac{8eU_0}{mr_0^2\Omega^2}, \tag{4.13}$$

$$q_x = q_y = \frac{q_z}{2};\ q_z = -\frac{4eV_0}{mr_0^2\Omega^2}, \tag{4.14}$$

the equations of motion can be written as:

$$\begin{aligned}
\tfrac{d^2x}{d\tau^2} - [a_x + 2q_x cos(2\tau)]x &= 0 \\
\tfrac{d^2y}{d\tau^2} - [a_y + 2q_y cos(2\tau)]y &= 0 \\
\tfrac{d^2z}{d\tau^2} + [a_z + 2q_z cos(2\tau)]z &= 0,
\end{aligned} \tag{4.15}$$

known as the Mathieu equations. The solutions of these equations have the form of:

$$k_1(\tau) = e^{\mu\tau}\phi(\tau), \quad k_2(\tau) = e^{-\mu\tau}\phi(-\tau), \tag{4.16}$$

where ϕ is a π-periodic function and μ the Lyapunov characteristic exponent, $\mu = \alpha + i\beta$ where α and β are functions of a and q while τ is a real variable. According to [MGW05], the value of μ and, by extension, the stability or not of the solutions depend only on the a and q parameters. This suggests that by plotting the $a - q$ plane, stable and unstable regions will arise. The condition where $\mu = in$ with n an integer, is satisfied by the values of (a, q) which are located on the characteristic curves a_n , b_n in the a-q plane, defining the boundaries between stable and unstable regions as shown in Fig. 4.3 .

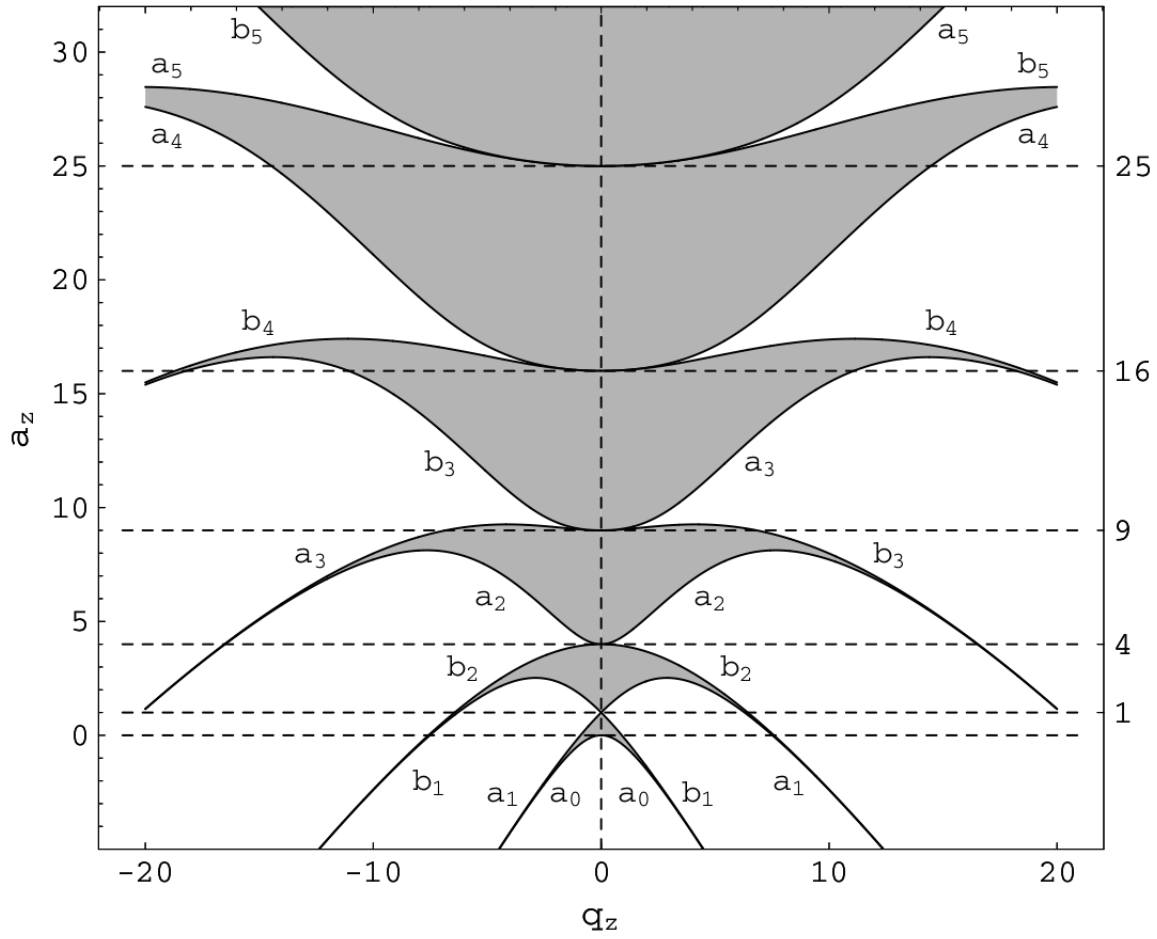

Figure 4.3 – Figure taken from [MGW05]. Stability diagram for the Mathieu's equation for the axial direction (z). The index under a and b represents n.

By adding the radial part for a proper 2D and 3D Paul trap, the diagram of the stability zones becomes Fig. 4.4 and Fig. 4.5 respectively. On both figures, the overlapping sections, here represented by the darker blue colour, are the stability on both radial and axial parts. Of course, for the 2D Paul trap it is slightly different since the overlapping parts represent stability on the radial part only. Since the axial and radial trajectories of the ions are now limited to these stability zones, they are thus exerting a strong constraint on the trap parameters which are found in the Mathieu parameters as the mass, charge, applied potential and distance between the electrode and the center of the trap.

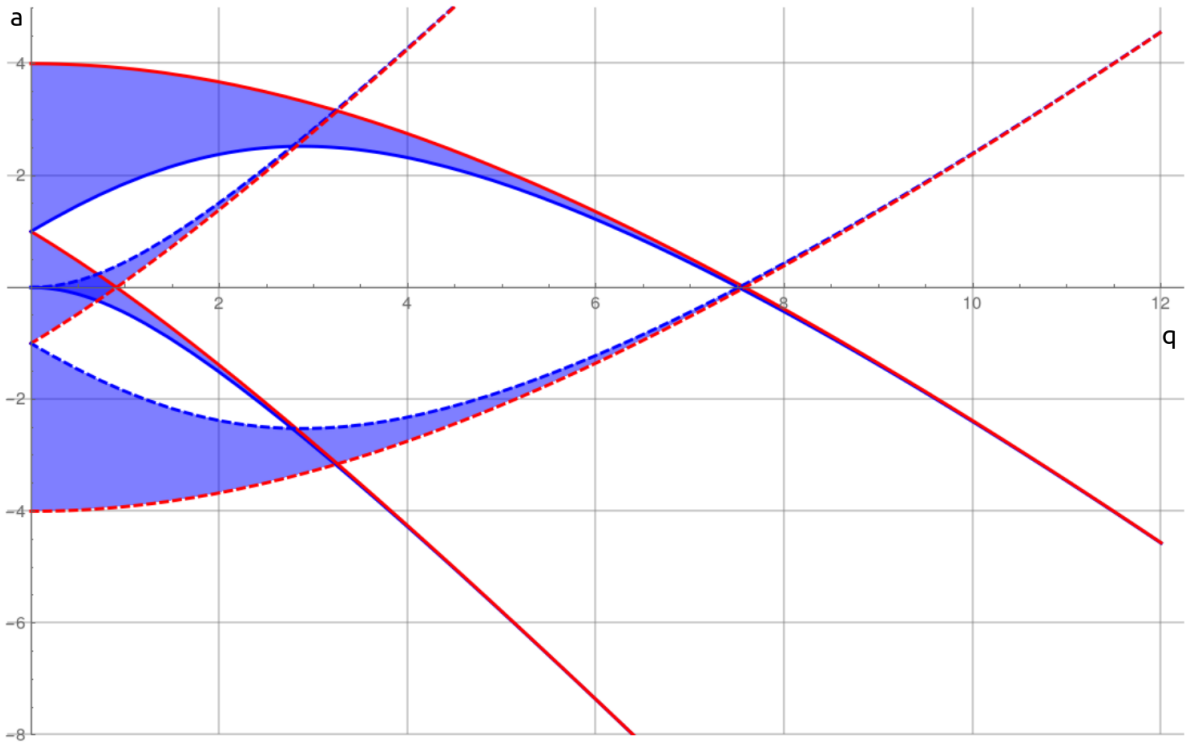

Figure 4.4 – Stability zones for a 2D Paul trap.

Of course, the stability zones are not magical spots where ions are guaranteed to be trapped. The experimental process involves other external parameters such as the trap capacity of the micro and macro-motions of the ion cloud that can bring ions out of the EM confinement.

We will assume a 3D Paul trap for the following. Experimentally, the most convenient zone to choose is the first one, near the origin. By using the notation where j = 1, 2, 3 and where $u_1 = u_x$, $u_2 = u_y$ and $u_3 = u_z$, The stable solutions of the Mathieu equations can be developed as an infinite series according to Floquet's theorem [Kuc93]:

$$u_j(\tau) = A_j \sum_{n=-\infty}^{\infty} c_{2n} cos[(\beta_j + 2n)\tau] + B_j \sum_{n=-\infty}^{\infty} c_{2n} sin[(\beta_j + 2n)\tau] = 0 \tag{4.17}$$

The c_{2n} and β_j can be expressed with both q and a parameters and they are not depending on the initial conditions. We can deduce that the characteristics of the ion motion are not dependent on the initial conditions, which means that the oscillation frequency is the same for all trapped ions and can be expressed as:

$$\omega_{j,n} = (\beta_j + 2n)\frac{\Omega}{2}; \omega_{j,0} = (\beta_j)\frac{\Omega}{2} \tag{4.18}$$

with $\omega_{j,0}$ the fundamental frequency. A typical example of ion trajectories is also shown in Fig. 4.6.

Typically for the experiment, we will stick to the first stability zone between [0; 0.908] along the q_z axis and $a_z = 0$. However, the number of trapped ions increases with the

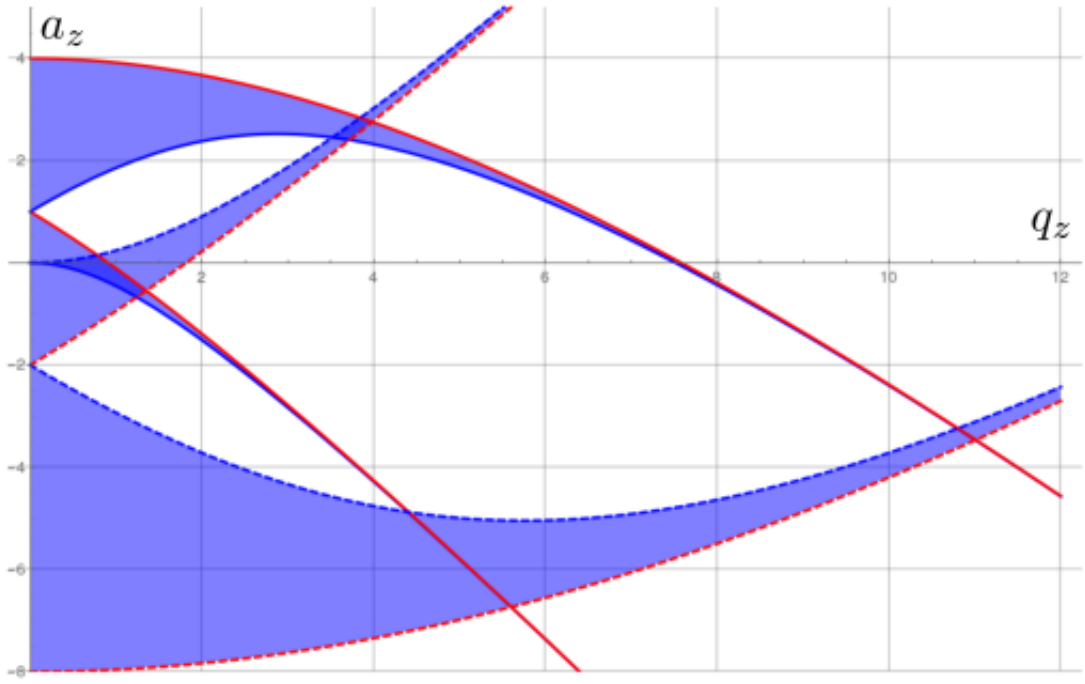

Figure 4.5 – Stability zones plotted by the MATHEMATICA framework for an ideal 3D Paul trap. The dark blue areas define the parameters for three-dimensional stability.

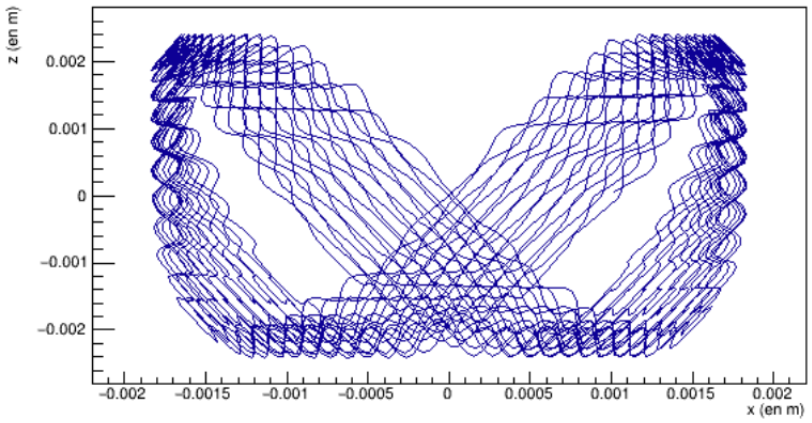

Figure 4.6 – Example of trajectory (Lissajous-like) of an ion A=6 and e = 1, in a simulated 3D Paul trap of r_0=12.5 mm and V_0 = 150 V.

applied potential well, to some extent, which is defined by the trap capacitance as described in Eq. 4.19 and in [Ben+20].

$$Q_{max} = \frac{1}{2}\pi\epsilon_0 q_z r_0 V_0, \tag{4.19}$$

where ϵ_0 is the vacuum permittivity. Increasing V_{RF} will also increase q_z, which will lead eventually to reach a greater q_z than the one allowed by the stability zone for a given frequency. That is why, during the whole commissioning and experiment, we have aimed to stay in the first stability zone corresponding to a null parameter a and a q_z in the interval

[0;0.908]. In the MORA experiment, the q_z parameter is around 0.5.

4.1.3 Micro and macromotion

In this part, we will discuss the different motions that ions have inside a non-ideal Paul trap. In the case of the first stability zone on which a and $q < 1$. The β parameter of eq. 4.18 is equal to:

$$\beta_j^2 = a_j + f_j(\beta_j) + f_j(-\beta_j); \text{ with } f_j(\beta_j) = \frac{q_j^2}{(2+\beta_j)^2 - a_j - \frac{q_j^2}{((4+\beta_j))^2 - a_j ....}} \tag{4.20}$$

which can be approximated to:

$$\beta \approx a + \frac{q^2}{2} \tag{4.21}$$

According to this approximation, the c_{2n} parameters will become very small as n is increasing. That is why we will limit the calculation to n = 1. We have then, $c_{-2n} = -\frac{q_j}{4} \times c_0$ and $c_{2n} = \frac{q_j}{4} \times c_0$. For $n = 1$, we also can rewrite the Eq. 4.17 as:

$$u_j(t) = G(1 - \frac{q_j}{2} cos(\Omega t)) cos(\omega_j t), \tag{4.22}$$

with G $= c_0\sqrt{A^2 + B^2}$ and $\omega_j = \beta_j \Omega/2$. ω_j can be considered as the frequency of the oscillator at a given Ω set on the electrode of the trap. A direct relation can be seen in 4.18, i.e. when Ω is increasing the frequency of oscillation is also rising. However, the amplitude of the oscillation will be reduced as Ω is rising. That is why two kinds of movements can be induced:

- The harmonic oscillation at frequency ω_j is called *macromotion* or *secular motion*.
- The movement caused by the applied A/C field at Ω frequency is called *micromotion*.

As shown in Fig. 4.6, the micromotion has a higher frequency but a much lower amplitude than the macromotion.

4.2 Buffer gas cooling

One technique developed to increase the trapping efficiency is to inject atomic gas inside the trap. It induces collisions between ions and the buffer gas atoms in order to equilibrate the ion temperature to the atom one. Some approximations can be made concerning the collisions according to [MGW05]. Indeed, at low energy, the collisions between the ions and the buffer gas atoms can be seen as a linear viscous force, proportional to the ion velocity that can be described as:

$$\vec{F} = f.\vec{v} \text{ where } \vec{v} = \frac{Q}{f}.\vec{E} \tag{4.23}$$

Because of their chemical neutrality, the buffer gas is typically chosen among the noble gases. The collisions between the ions and the buffer gas atoms will result in a change of direction of the ion momentum, energy, and stability inside the trap. Such redistributions will eventually kick out ions outside of the trap but on average, depending on the gas, it

will increase or decrease the mean energy of the ions and thus, the trapping efficiency. In an RF field, the evolution of ion kinetic energy due to collisions with the gas atoms depends on the relative mass of the ion and the buffer gas atom. It can be explained by the fact that the mass impacts the way the collision interrupts or not the micro-motion of the ions as described in [MD68]. Two cases are taken into account:

- If the mass of the buffer gas atom is heavier than the ion mass and assuming only pure elastic collisions will occur, the atom cloud can be seen as a fixed scattering center since it is not interacting with the RF field. As described in [MD68] a phenomenon called RF heating can occur in this case. This occurs when the ions are subject to non-periodic Coulombian forces, typically in the vicinity of another ion, as well as Coulombian forces from the RF field of the trap. This heating will induce perturbations in the trajectory of the macro and micro motions leading to an increase of the ion losses from the trap.

- If the mass of the buffer gas atom is lighter than the mass of the ions then the collisions can be approximated by a viscous force. As a result, the average kinetic energy will decrease with time. One can summarize the successive weak collisions, for $A_{ion} \gg A_{gas}$, as the frictional force such as $F = f\vec{v}$. The first demonstration can be found in [WSL04].

In order to increase the trapping efficiency of the experiment, a helium gas has been chosen to cool the ion cloud down. The gas is injected inside the vacuum chamber until it reaches a pressure equal to 1×10^{-5} mbar but several tests, more qualitative than the one presented below, have been done in order to get a better trapping efficiency (see Subsec. 5.3.2).

4.3 The MORA trap

The MORA trap is a key piece for the experiment. It has been simulated and optimized at LPC Caen [Ben+20], in order to get the most homogeneous field inside the trap. Compared to the older trap LPCTrap, also designed at LPC Caen, the MORA trap distinguishes itself by a greater axial angular acceptance about 27% larger and a trapping capacity 30% more important, passing from 1.56×10^6 to 2.20×10^6 ions trapped[1]. This optimization has been done by solving the Laplace equation, within the region of interest of the trap. Several methods exist for this purpose:

- The finite element method (FEM, see [Wika])

- The finite difference method (FDM, see [Wikb])

Here, this study has been done with a homemade C++ Laplace solver based on the boundary element method (BEM, see [Wikc]). This method is distinguished by the fact that it uses a 2D meshing contrary to both FEM and FDM which require a 3D meshing. Since BEM only requires meshing the surface of the system (here electrodes), it saves a lot of computing time and memory while increasing precision. Furthermore, this study has been conducted in

[1]These values take into account a scaling of LPCTRAP dimensions to fit the MORA trap dimensions.

order to minimize the contributions of higher harmonics of the potential inside the trap. As in reality, an ideal Paul trap does not exist, the contribution of harmonics of order higher than $n = 2$ is not null and thus, it is with the aim of minimizing these contributions of higher order terms that the study has been conducted.
Concerning the trap of the experiment, it is composed of two Einzel lenses and six electrodes, as shown in Fig. 4.7a. As a result, the trap is composed of six electrodes:

- R1 and R2 are the RF electrodes that create the radio-frequency quadrupole field. The amplitude of the field is provided by the power supply. Ideally the higher the voltage is, the better the trapping efficiency. It will indeed create a deeper potential well that will confine more ions inside the trap. However, after a certain value, the Mathieu parameter, q_z increases, degrading the trapping procedure.

- R3 and R4 are respectively the extraction and injection electrodes where the trapping procedure is presented in the following chapter.

- R5 and R6 aim to correct defaults in the electric field due to the higher order harmonics and also to screen the electric field between the trap itself and the detector located around.

A choice has been made concerning the shape of the inner electrodes in order to increase axial acceptance. Indeed, conical-shaped electrodes have been chosen for the MORA trap instead of the previous cylindrical-shaped ones for LPC Trap. In comparison to its predecessor, LPC Trap, MORA trap has an axial angular acceptance of $\Omega_A = 55.4°$ contrary to $\Omega_A = 43.6°$ for LPC Trap which is 27% larger. Concerning the radial acceptance Ω_R, LPC Trap is 6% larger than MORA trap, from $\Omega_R = 38°$ for LPC Trap and $\Omega_R = 35.9°$ for MORA. The following Fig. 4.7b illustrates the different acceptances. Finally, the characteristics of MORA trap are summarized in table. 4.1.

Properties	***Values***
Angular acceptance Ω_A	43.6°
Radial acceptance Ω_R	35.9°
r_0	19.24 mm
V_0	± 150 V
Ω_{RF}	2.07×10^6
R1/R2 Thickness (mm)	2.50
R3/R4 Thickness (mm)	4.53
R5/R6 Thickness (mm)	4.50
Maximum capacity	2.20×10^6

Table 4.1 – Characteristics of the MORA trap.

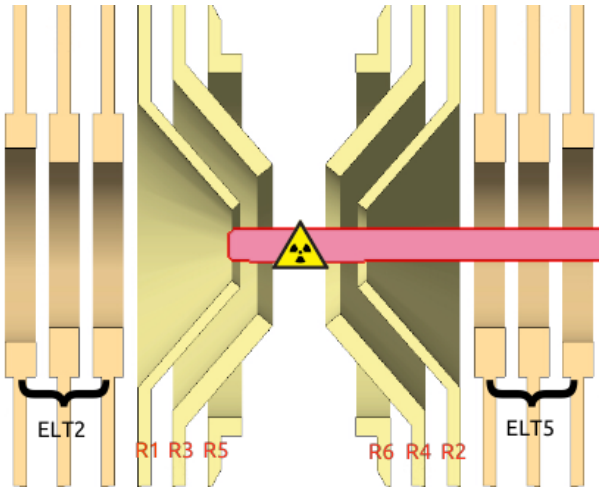

(a) Schematic view of the trap with the radioactive source finger inside, where all lenses and electrodes are labelled. ELT2 and 5 stand for Einzel Lens n°2 and n°5. The electrodes labelled from R1 to R6 stand for Ring n°1 to 6 and are the electrodes of the trap.

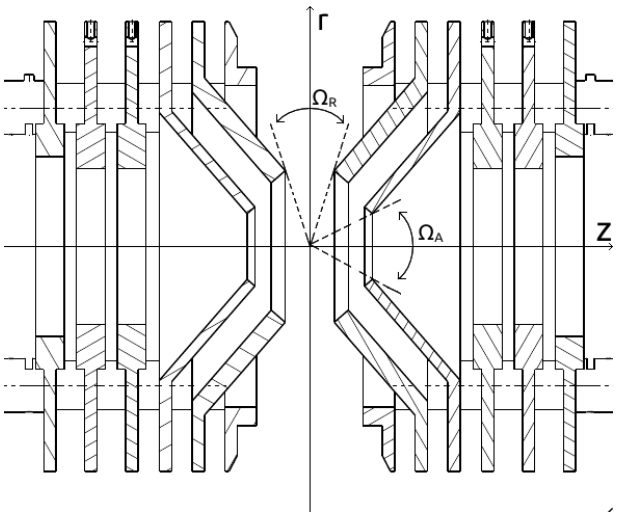

(b) Representation of MORA trap on which the different acceptances are displayed.

Figure 4.7 – Complementary views of the MORA trap.

Chapter 5

Commissioning of the experiment

In this chapter, we shall present the two commissionings that have been done. We will introduce the commissioning performed at LPC Caen where a typical ion path will be presented. The overall performance of the experiment will be compared to some SIMION simulations. In a second section, a presentation of the set-up installation at JYFL will be given, followed by the description of the different offline sources used. Finally, the results acquired during this commissioning will be presented in the same spirit as the previous part.

5.1 Commissioning at LPC Caen

5.1.1 Presentation of the line

To be able to measure D, a bunch of radioactive ions will be slowed down until they reach near-zero kinetic energy. They are then, trapped by the transparent Paul trap (see Sec. 4.1). Starting with the injection line to the vacuum chamber, the ions will successively travel through the following elements:

1. A pulsed drift tube (40.2 cm long) the operation of which is described in Sec. 5.1.3.2.
2. A steerer (four electrodes) used for correcting the beam direction.
3. An Einzel lens, for correcting the beam emittance.
4. Another steerer, identical to the first one.
5. Another pulsed drift tube (18 cm long).

At the end of the second pulsed drift tube, begins MORA's vacuum chamber and the trap itself which is composed of:

1. Six ring-shaped electrodes (see Fig. 4.7a).
2. Two Einzel lens triplets to correct the beam divergence just before and after the trapping process.
3. A deflector that drives the beam to a MCP detector.

Pulsed drift tubes, as well as the Einzel lenses, are composed of three electrodes with two of them grounded and framing the main one. At the very end of this beamline, a Micro-Channel Plate (MCP) detector is placed in such a way that it will interact neither with the laser beam nor with the offline radioactive sources. The entire line can be seen in Fig. 5.1 and a closer look at the MCP2 detector is shown at the end of Chap. 3. It is important to mention that during the commissioning at LPC Caen, the MCP located at the end of the line was in the direct configuration which means it was perfectly aligned towards the beam direction which will not be the case for the next set-up. Due to the laser beam polarisation, the MCP2 has to be slightly placed off-axis. Finally, some extra devices can be inserted via a feedthrough actuator connected to the slow control. They can be operated independently which brings great modularity to the experiment:

- Four attenuator plates (90% + 10% of transmission).
- A MCP detector + a phosphorus device.
- A mirror for the laser alignment.

These extra devices are located between the first set of steerers and the Einzel lens as shown in Fig. 5.2. The entire experiment is monitored by a slow control developed at LPC Caen in EPICS system. Each power supply as well as the vacuum pressures and the time sequences can be set and modified directly from the slow control graphical interface. Besides its modularity, it brings a very restrictive procedure to pump the system which is nearly mistake-free.

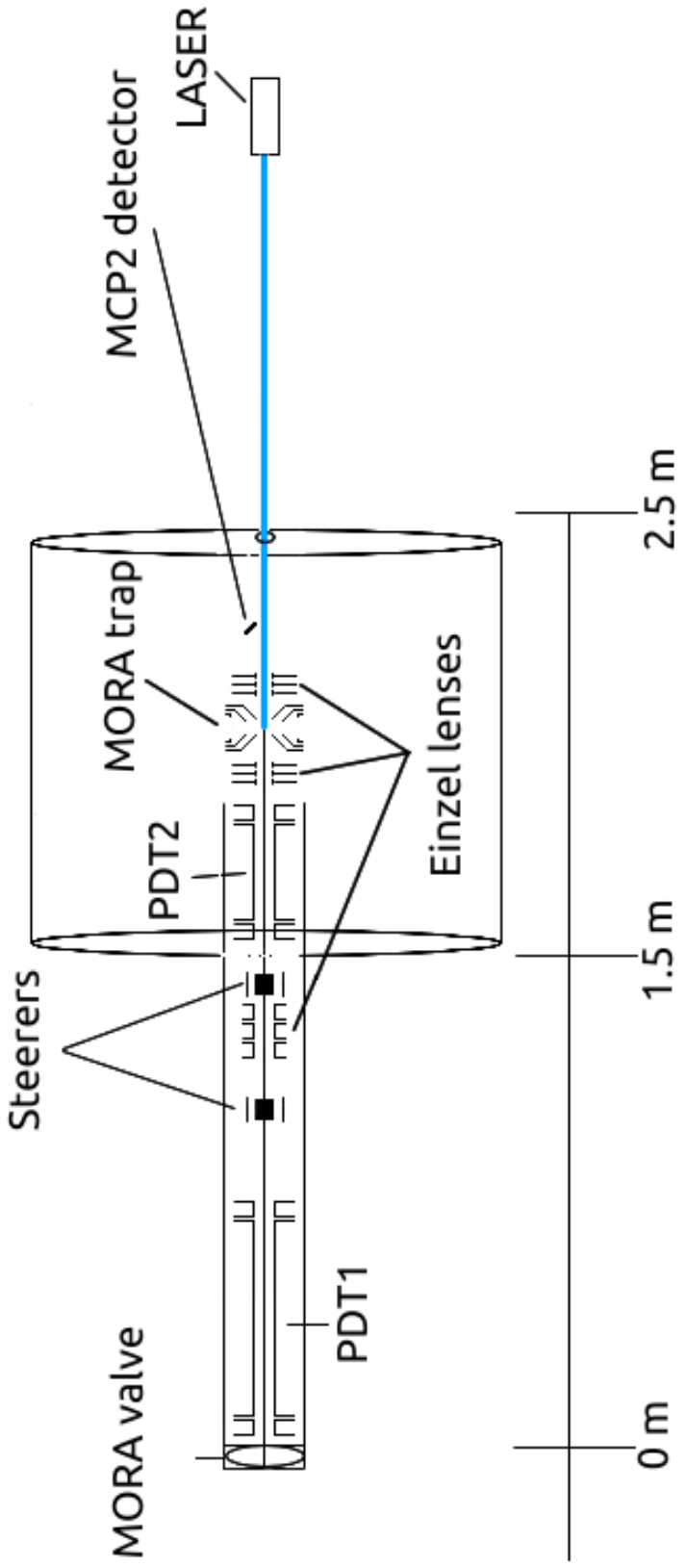

Figure 5.1 – Schematic view of MORA beamline. The devices inside the line are not scaled for visibility.

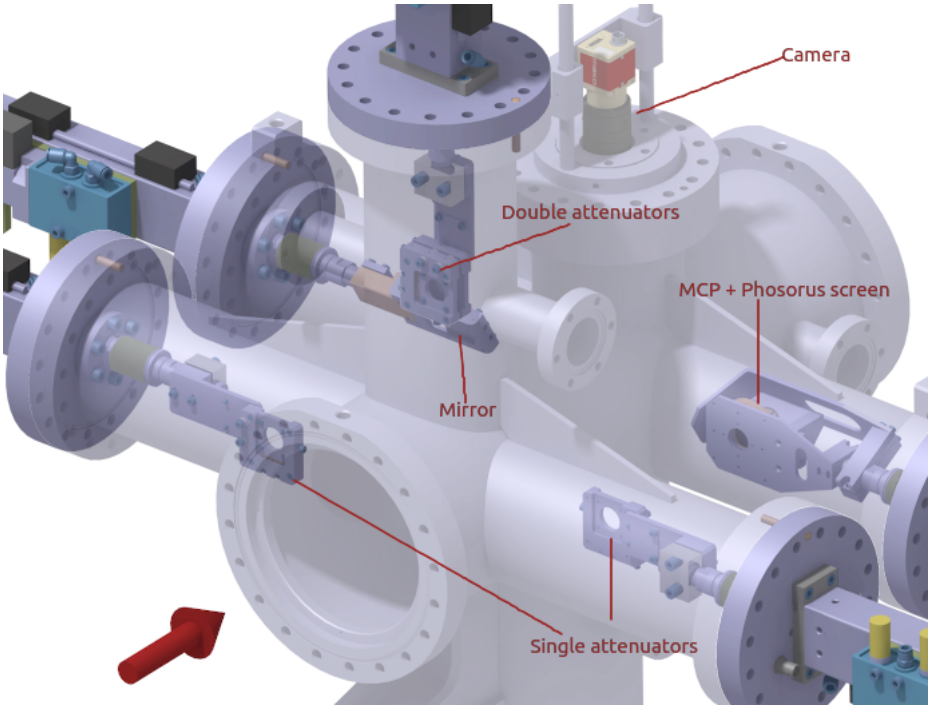

Figure 5.2 – 3D view of the center of the line displayed on the slow control interface. This image takes place just between the first steerer and the Einzel lens. The red arrow symbolises the beam direction, going from the beginning of the line to the trap chamber. As displayed in the picture, no extra devices are currently inserted in the line. The four attenuators (here in "1+2+1" configuration) can be seen as well as the MCP, mirror, and camera. The picture is a representation of the line in a sectional view.

5.1.2 Offline source

For performing the LPCC commissioning, a surface ionization source of stable ^{23}Na (see Fig. 5.3a)was used and installed instead of the MORA valve. The ^{23}Mg is used for the online experiment, which is the reason why, to calibrate the line and trap, we used the same mass number. A sodium pellet was placed before the extraction electrode (see Fig. 5.3b). An RFQ was added for creating a bunched source, as during the real experiment. Sodium atoms are ionized by heating. While the pellet reaches the nominal temperature, the current also ramps up until it reaches a maximum. The ions are extracted from the pellet by the acceleration electrode, stopped by the injection electrode, trapped in the RFQ, and finally extracted from the trap by an electrode (see Fig. 5.3). During this phase, the extraction electrode is set at 1505 V and the injection is set slightly under at 1495 V, to create a smooth slope of potential. Ions result in having about 1500 eV of kinetic energy. A lens is placed after the injection electrode to focus the beam after the source. At the end of the source, a steerer helps to guide the beam through the line.

The source itself is supposed to deliver a number of ions homogeneously distributed from its circular pellet surface. Even though a pure ^{23}Na pellet was ordered, we realised other elements[1] were also present in the pellet such as ^{39}K and ^{85}Rb, in higher emitted proportions

[1]They will be called contaminants for the rest of this chapter.

than ^{23}Na as shown in Fig.5.4. Especially at low heating[2], the ratio between the amount of ^{39}K and the amount of ^{23}Na was around 5.

Elements	*First ionisation energy*
^{23}Na	5.14 eV
^{39}K	4.34 eV
^{85}Rb	4.18 eV

Table 5.1 – First ionization energy of the different elements in the offline source according to NIST website.

According to the values shown in table 5.1, these contaminants are more likely to be ionized than sodium. This has impacted the entire commissioning since the source pellet used was highly contaminated. This surface ionization pellet source was replaced by a new one to get rid of these contaminants but it appeared that the new source was similar.

When ions fly inside the RFQ, they are firstly stopped by the injection lens, they are then trapped inside the RFQ since we apply a radio-frequency potential to its electrodes.

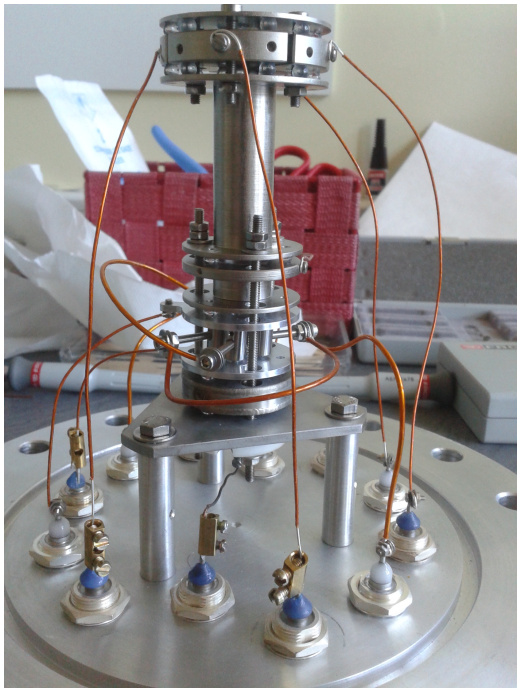

(a) Source of ^{23}Na entirely wired and ready to be used.

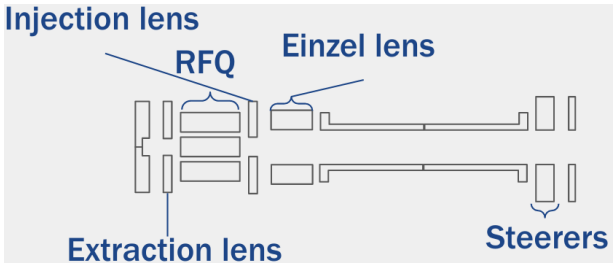

(b) Representation of the surface ionization source.

Figure 5.3 – Different views of the surface ionization source used for the LPC Caen commissioning of MORA.

Concerning the radio frequency of the RFQ, a dedicated ISEG power supply and a waveform generator are used. The potential is sinusoidal with $V_{amp} = 6.5$ V, the frequency is set at 1 MHz. The wave generator sends both signals to the electrodes and to the time

[2]The low heating is difficult to quantify since the input voltage was set by a potentiometer from which the graduations are gone.

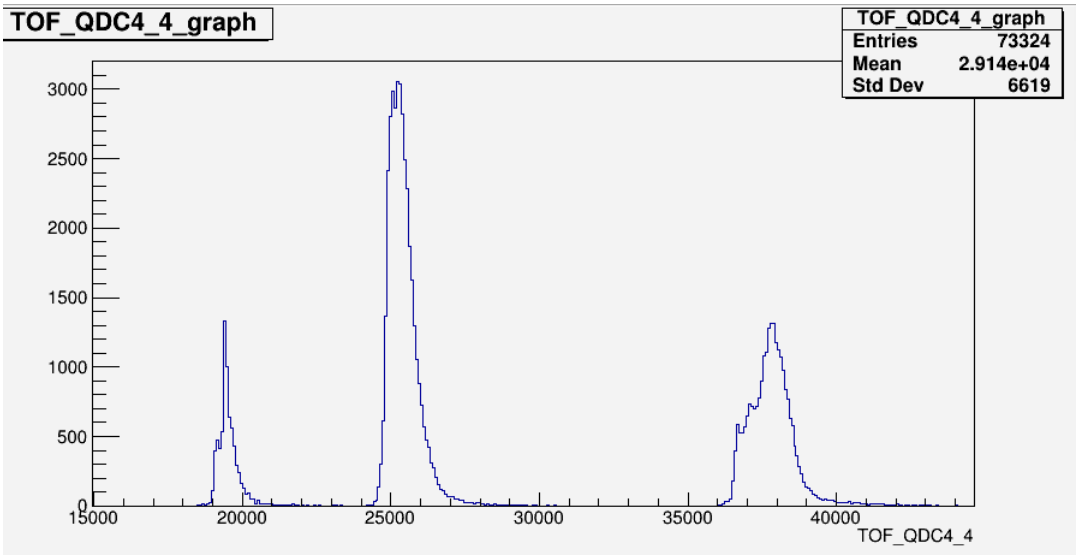

Figure 5.4 – Ions contained in the surface ionization source. From left to right, ^{23}Na, ^{39}K, ^{85}Rb. TOF is in ns.

sequencer device of the slow control. Connected to the external trigger input of the slow control, the extraction creates the T_0 for the rest of the bunch timeline.

5.1.3 The ions' journey

Once the ion bunch has been emitted from the source, it travels through the first pulsed drift tube (see Fig. 5.1). Since the bunch is already at low energy ($\sim$ 1500 eV), it does not need to be slowed down. As a result, the PDT1 was set as a lens, focusing the bunch via an 800 V positive potential. It can now either be detected by the extra MCP, called MCP1, which can be inserted in the line or continue its journey.

5.1.3.1 Detected halfway

Before sending the beam to the trap, a first check of the beam energy dispersion and shape on the MCP1 can be done. The shape can be distinguished as shown in Fig. 5.6, by applying a voltage of about 1800 V on the phosphorus device (see Fig. 5.2).

The ions hitting the MCP1 create an electronic cascade that is re-accelerated by a potential difference. Then, they hit the phosphorus screen, hence creating light by de-excitation. The assembly can be seen in Fig. 5.5. This feature of the line is handy, thanks to the direct readout of the beam shape optimization. However, to see the image presented in Fig. 5.6, a camera device is needed. It is placed just above the position of the first MCP when in the line. This position also allows us to monitor the laser beam with the mirror apparatus (see Fig. 5.2).

5.1.3.2 Continuing the travel

After the PDT1, the bunch is driven to the position/direction adjustment section made by two sets of steerers and an Einzel lens. The voltage set on the steerers is highly dependent

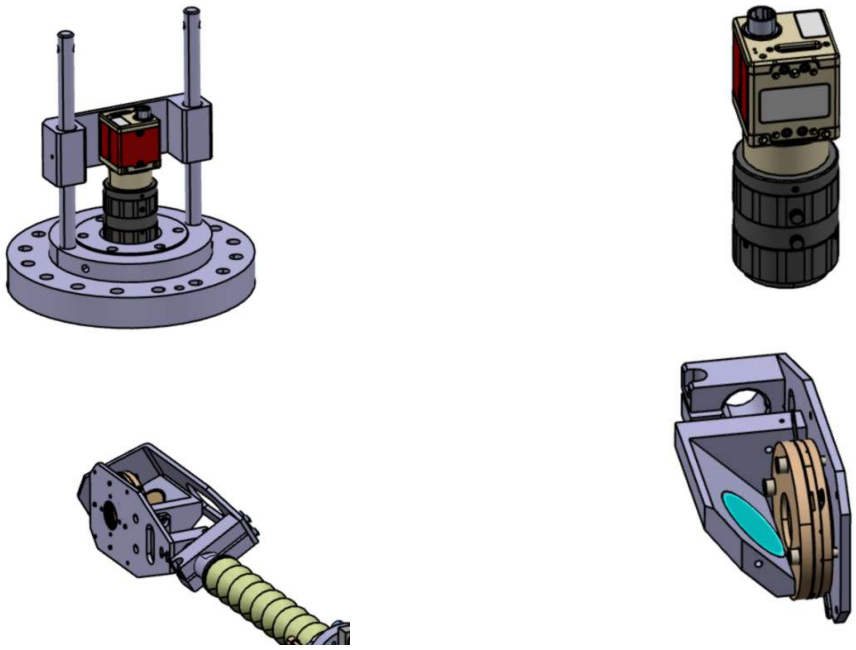

(a) (b)

Figure 5.5 – Close-up view of the system MCP + phosphorus screen, also called MCP1. In Fig. 5.5a, one can see the injection device and the camera apparatus. In Fig. 5.5b, located on the right, one can see the mirror in cyan, which reflects the phosphorus screen. In this image, the camera has been set closer to the MCP for convenience.

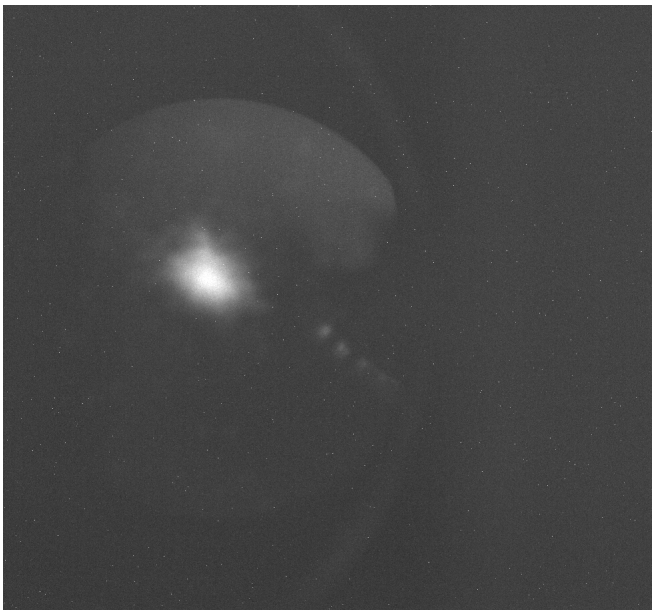

Figure 5.6 – Screenshot of the camera display. The main spots are ions interacting with the phosphorus device. The line at the bottom right of the screen is a crack in the MCP1 which has been replaced since.

on the bunch shape and, as a result, it will not be written here. The lens voltage, however, remains consistent and is set at 200 V. According to SIMION simulations, detailed in Sec. 5.2

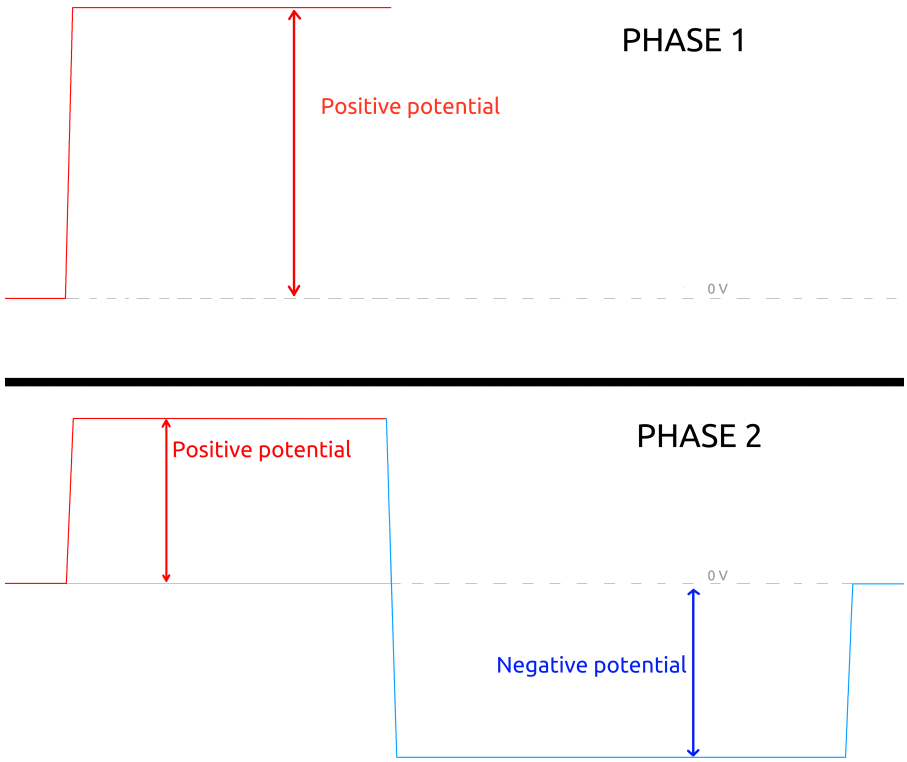

Figure 5.7 – Illustrated process used to slow down the ion bunches.

of this chapter, it helps to get a nice and focused beam. The bunch then reaches the second pulsed drift tube.

To do so, a positive potential (+945 V) is applied to the PDT2 which can be seen in Fig. 5.8. When the bunch enters inside the PDT2, ions lose 945 eV of kinetic energy. Once the bunch is fully inside PDT2, the voltage is switched down to a negative value (-455 V). Ions, when exiting the PDT2, have to "climb" this potential hill, losing again kinetic energy as shown in Fig. 5.7 to reach a mean kinetic energy around 110 eV. Nevertheless, the bunch remains too energetic to be trapped, which is why a positive potential is set on the inner electrode of the trap, named R4, at +343 V.

Since the bunch is located a few mm away from the electrode surfaces where the voltage is applied, leading to a potential about the same order as the ions bunch kinetic energy. When the ions start to get repelled by the applied voltage, we turn off R4 and switch on the RF procedure. The whole trapping sequence is described in Fig. 5.8 and the trap characteristics can be found in table 5.2.

5.1.4 The trapping procedure

This subsection presents the radio-frequency system used during this commissioning. A pulse generator (CGC instrument), was delivering square shape signals to the trap electrodes R1 and R2. The switch between the positive and negative values was very narrow and almost instantaneous (a few 10 ns). However, this switch brings a large electromagnetic wave inside the chamber that completely blinds each detection system. In order to get rid of this effect, a filter that attenuates the applied voltage on the electrode has been applied. It transforms this sharp square signal into a smoother, shark fins-shaped one (see Fig.5.9). The pulse generator is entirely adjustable and compatible with EPICS, *i.e*, fully implemented on our slow control thanks to the work of C.Vandamme from LPC Caen. Nevertheless, due to quite limited documentation given by the constructor, the settings in the user interface are not very explicit. Here is an explanation of how this works: The first thing to define is the trapping duration. This corresponds to the "RF Trap" in Fig. 5.8 and "Pulser 1" which can be seen in Annex (see Table. 9.3a). From there, the frequency of the trap is defined to have a Mathieu parameter of 0.5. However, in the setting panel of the CGC, only the half period can be set indicated by the "Pulser 0" column in Table. 9.3a. Then, one has to define the number of periods given the previous half periods, during the trapping duration symbolised by the "Burst size" in Table. 9.3a. Hence, the number of half-period × the duration of one half-period has to be inferior or equal to the trapping duration. This is theoretically how the trapping settings work but experimentally, one had to slightly readjust the trapping duration to fit the number of bursts. Of course, the calculation has to be done for any changes in the frequency or bunch cycle making the trapping procedure quite heavy and a mistake can quickly happen.

V_{RF}	***Frequency***	***Mathieu parameter***
51 V	0.333 MHz	0.523

Table 5.2 – Trap characteristics resulting from the first trapped ions in the MORA trap.

5.2 SIMION simulations

SIMION is a software used to simulate the dynamic of ion beams in electric fields. It is a very powerful tool since it brings a dedicated environment allowing the user to program a complex macro file, use data recording, visualize trajectories, and even display the potential maps. This software has been used for decades, mainly in low-energy physics experiments (nuclear and atomic) and to tune small accelerators.

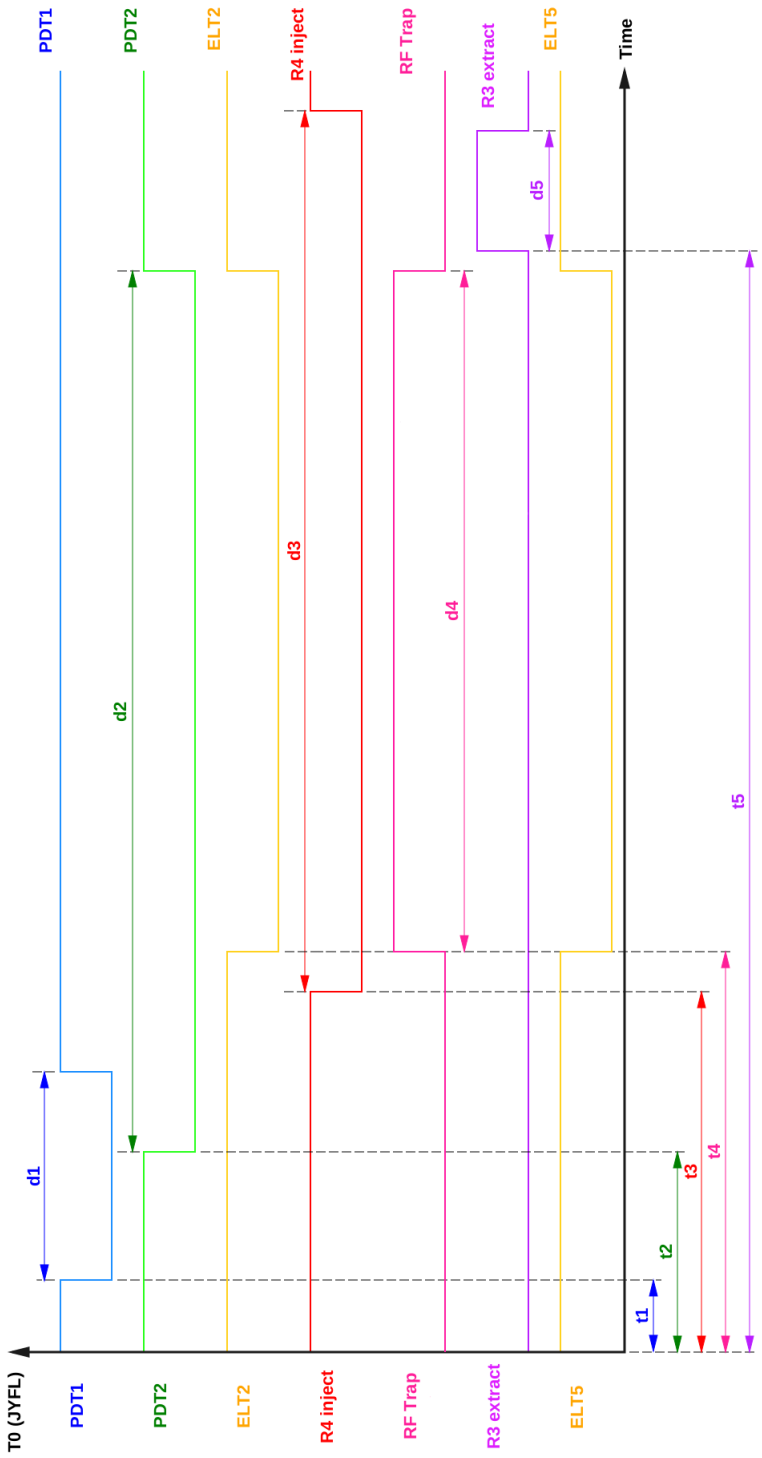

Figure 5.8 – Detailed time sequence of the trapping procedure. In this figure, one can see the shape of the logical signals triggering the different electrodes. The PDT2, for example, is constantly set on the positive voltage until t_2, also called T_{PDT2}, where the negative value is applied. At the bottom of the figure, one can see the different timings where t_3 is also called $t_{\mathrm{injection}}$, t_4 is t_{RF} and t_5 is t_{Extract}. These timings are defined according to the T_0 of the slow control. The "d" letters correspond to the duration of the switched signals.

Figure 5.9 – Picture of the RF signal after the filter.

The goal of the simulations that are performed for MORA, was to be able to recreate the beamline and the trap as set at LPC Caen during the corresponding commissioning. Former simulations have been performed by B.M. Retailleau [Ret21] and P. Delahaye but mostly for the trap section. After verification of the dimensions with the help of Y. Merrer, CAD designer of MORA, the beamline and the trap have been simulated. The simulated beam-line can be found in Fig. 5.10. The source, however, was more problematic to simulate since there were no drawings to refer to.
Concerning the ions, just like in reality they have a mass number $A = 23$ and a charge q $= +1$.

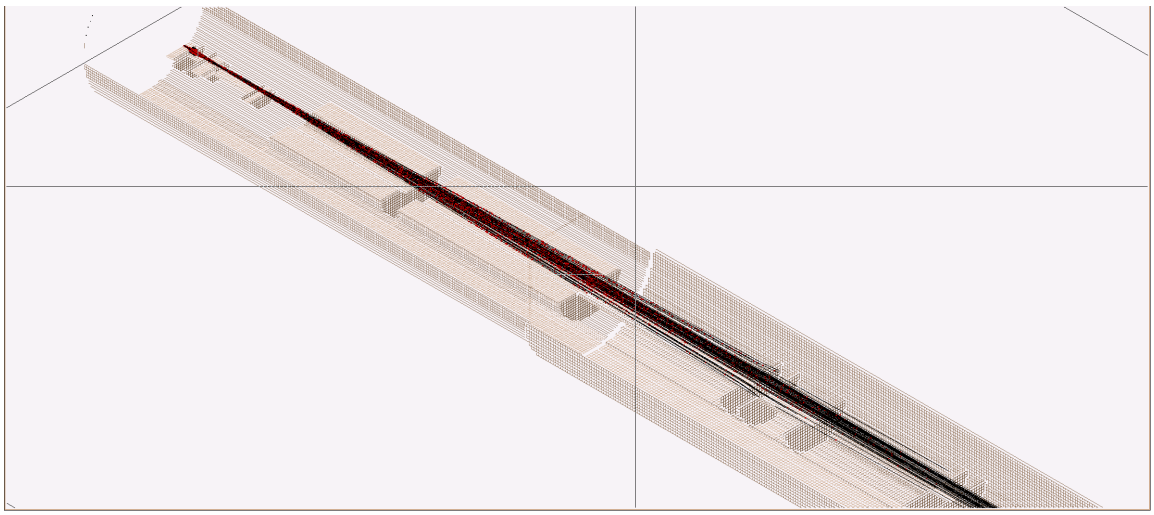

Figure 5.10 – 3D view of the beam line drawn by SIMION.

Because of SIMION limitations concerning the maximum number of ions that can be simulated, we have limited our studies to 1000 ions. This appears as a good compromise between statistics and computation time. Some approximations have been made, especially about the ion's creation. Ions have been generated in an uniform distribution from a circular surface. Ions then fly until reaching the RFQ and mostly (80% to 90%) die during the bunch formation process. As a result, by taking into account the transmission in the line plus the trapping efficiency, no ions are correctly extracted. In order to avoid this problem, we have chosen to directly create the ions inside the RFQ with a spherical distribution, after a duration of about 100 µs, ions are ejected from the RFQ by the same slope process as the one described in Sec. 5.1.2. After the PDT1, the beam is driven until it reaches the PDT2. The positive voltage has first been set at $V_{PDT2pos} = 945\ V$ and then the negative one at $V_{PDT2neg} = -455\ V$, this difference of potential should be set at ΔV =1500 V maximum due to the power supplies limitation.

SIMION gives a pretty straight beam which is, unfortunately, different from reality. For example, in the simulation, the steerers are completely useless which is obviously not the case in the experiment. This different behaviour of the beam induces some discrepancies in the results of the timings between the experiment and the simulation. The different timings of the pulsed drift tubes have been found by creating a virtual plane in the middle of the PDT, which will not interact with the particles. By passing through this "spy" plane, we will have access to several pieces of information such as:

- The mean kinetic energy and its standard deviation.
- The mean time of flight and its standard deviation.
- The mean transverse locations (y and z axes in SIMION) and associated standard deviations.
- The number of ions passing through.

The technique consists of firstly applying the positive potential (+950 V for example) without switching the pulse drift tube. We have then, the mean time of flight (TOF) in the middle of the pulsed drift tube (the second one in this example). We apply the negative voltage at the timing found earlier. To make sure the ions have the correct energy, we can shift the virtual plane at the exit of the pulsed drift and probe their energy. The trapping process, however, is way more complicated to define since there are two different times to find:

- The T_{stop} for which the ions will be almost at 0 eV during the injection phase.
- The T_{RF} for which the RF is starting.

In order to get those timings, a much more qualitative process has been done. In SIMION, the trajectories of the ions are visible, which means that one can have a direct readout of the bunch behaviour. When ions fly inside the trap, they are repelled by the potential applied on the R4 electrode. The moment, defined by the time of flight when the ions are stopped, *i.e* just before get repelled, is the T_{stop}. The T_{RF} is equal to or slightly higher than the T_{stop};

it will not be the same during the commissioning at IGISOL because the RF is on during the final slow down of the bunch. The trapping efficiency can be probed more accurately than in the experiment since we can just place two spy planes before the trap and at the MCP2 detector. Those spies are very useful since they can probe the energy and time of flight of the beam wherever in the line. As a result, the transmission and efficiencies inside the simulated line are given in table 5.3

Location of the spy planes	***Number of ions***	***Transmission***	***Total transmission***
After the source	176	PDT1 = 82.9%	Beamline = 81.8%
After PDT1	146		
Before PDT2	146	PDT2 = 98.6%	
After PDT2	144		
After Trap	30	Efficiency = 20.8%	N/A

Table 5.3 – Transmission inside the line in the LPC Caen commissioning configuration. The transmission for PDT1 is the ratio between the number of ions before and after the PDT1. The same goes for PDT2. The trapping efficiency is the ratio between the number of ions after the PDT2 and the number of ions after the trap. The trapping efficiency varies between 10 and 20% according to trapping optimizations.

5.3 Commissioning measurement

This campaign took place between the end of August[3] and the end of September 2021. The entire commissioning was done in one month, because of the very tight schedule. Indeed, the experiment was planned to be shipped to Jyväskylä at the beginning of October 2021. Unfortunately, during the travel process, the vacuum chamber box has fallen to the ground, damaging the chamber itself. The rest of the line has reached Jyväskylä but the chamber and detectors have been sent back to the LPC Caen for diagnostic and repair before their return to Finland in December. More details will be given in Sec. 7

Thanks to SIMION simulations, we obtained a good starting point concerning the timings. Indeed, due to the discrepancies in terms of initial beam properties between the simulation and the experiment, the simulated timings did not perfectly match those found experimentally. However, the time of flight between the center of the PDT2 and the MCP2 was correct and by knowing the TOF displayed by FASTER, we were able to correct the timings for switching the PDT2. Since the source we have used contained also other elements as mentioned in Sec. 5.1.2 and since the line was tuned for ^{23}Na, it implied that the contaminants will not be slowed down.

As a consequence, they will reach the MCP2 before the sodium ions. Typically when the ions are passing through the trap, we obtain the spectrum shown in Fig. 5.11. To be able to probe the beam, either by doing an energy dispersion test or a trapping efficiency test, we first have to get rid of the potassium. It appears that in front of the MCP2, there is a grid on which we can apply a positive potential. If this potential gets higher than the kinetic

[3]Technically, July for the line.

energy of the sodium at the exit of the PDT2, we can remove the sodium. By doing so, only the potassium will remain and by subtracting the integral of the potassium peak from the previous double peak, we obtained the integral of sodium passing through the trap.

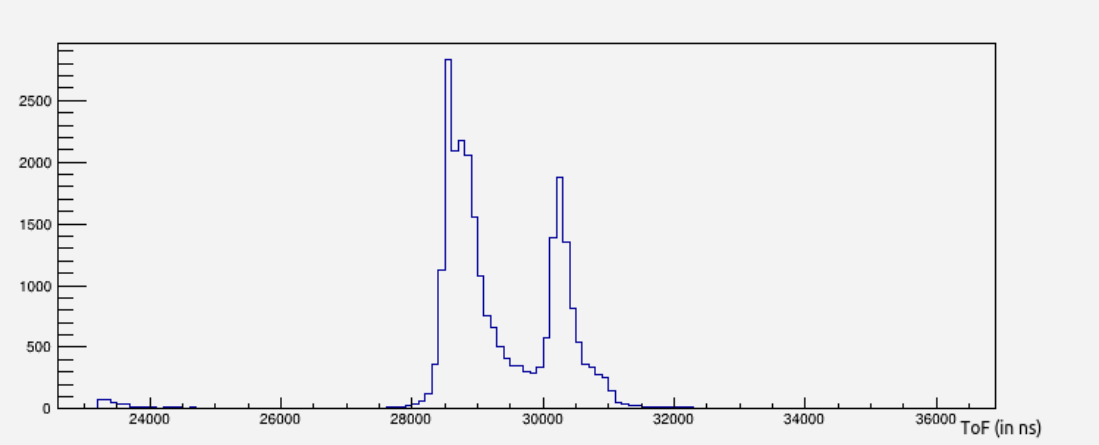

Figure 5.11 – TOF spectrum after the switch of PDT2. Due to the lower energy of the ^{23}Na (on the right), the ^{39}K (on the left) has arrived before. A much smaller peak can be seen below 24 µs, it corresponds to the sodium not slowed down.

5.3.1 Energy dispersion

Before starting the trapping procedure, we first had to make sure that the beam had the expected energy. To be able to probe the energy dispersion of the beam, we have used a very simple process. By increasing the potential on the grid in front of the detector, the integral of the sodium peak taken within 30 s on the MCP2 has decreased, according to Table 5.4. This table and the spectrum in Fig. 5.12 show a mean energy of around 110.52±0.32 eV. This value was determined by plotting the derivative of the plot shown in Fig. 5.12.

Knowing the mean energy of a bunch, the trapping process can now be tested as well.

5.3.2 Trapping efficiency

One of the other tests we could perform during this commissioning was to test the trapping efficiency. Since the trap is the most important part of the line, knowing this efficiency is crucial. Once the ions are trapped, detected by the MCP2 and during the thirty-second acquisition, for example, we disable the trapping procedure and just let ions pass through the trap. Of course, we will have the same issue as in the previous tests concerning the potassium ions. In order to remove it, we apply a positive potential, which is greater than the kinetic energy of the sodium ions, to a grid just in front of the detector. By doing so, only the potassium ions will remain and by subtracting to the integral of the dual peak, we now have the integral of the "direct" sodium ions. Once we have the number of trapped sodium ions and the number of direct ones, we can calculate the ratio:

$$\xi_{trap} = \frac{\text{Number of trapped } ^{23}\text{Na}}{\text{Number of direct } ^{23}\text{Na}} \tag{5.1}$$

Grid voltage	*Integral*
0	4035
100	3494
102	3035
104	3017
106	2907
108	2780
110	2033
111	1572
112	1213
113	752
114	358
115	228
116	70
117	70
118	19
120	48

Table 5.4 – Energy dispersion after PDT2 switch on the MCP2.

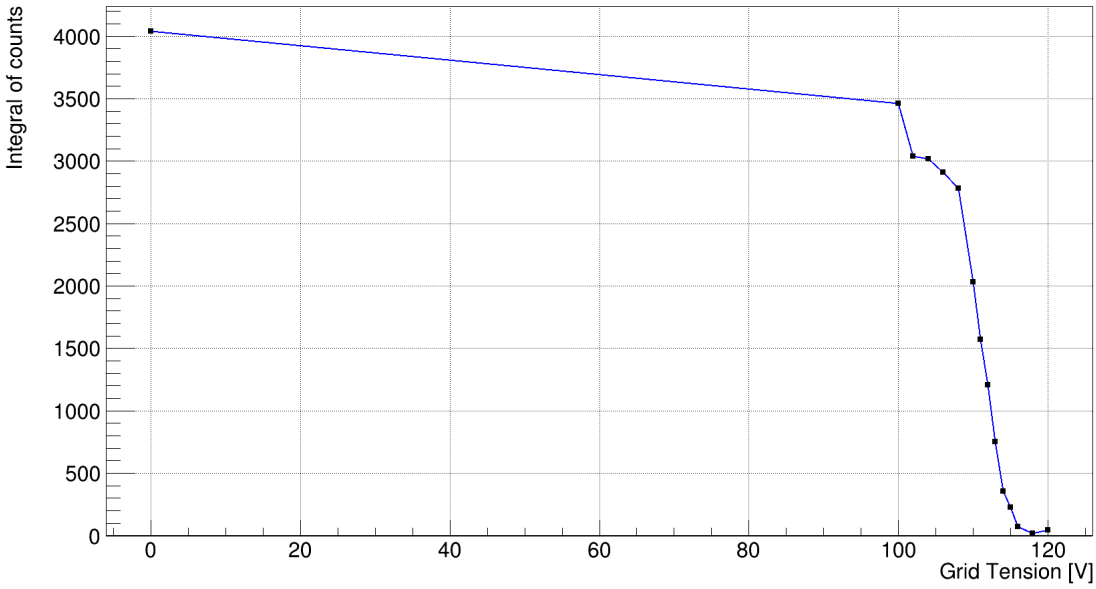

Figure 5.12 – Energy dispersion after PDT2 switch. Data collected on MCP2. The mean energy of the ions is 110.52 +/- 0.32 eV at the exit of the PDT2.

5.3.3 Gas injection

The cloud is then cooled with He buffer gas (see Sec. 4.2). This gas is injected inside the chamber *via* an injection system connected to a helium gas tank. Of course, one has to properly pump the injection tube to get rid of the impurities. This is done with a primary

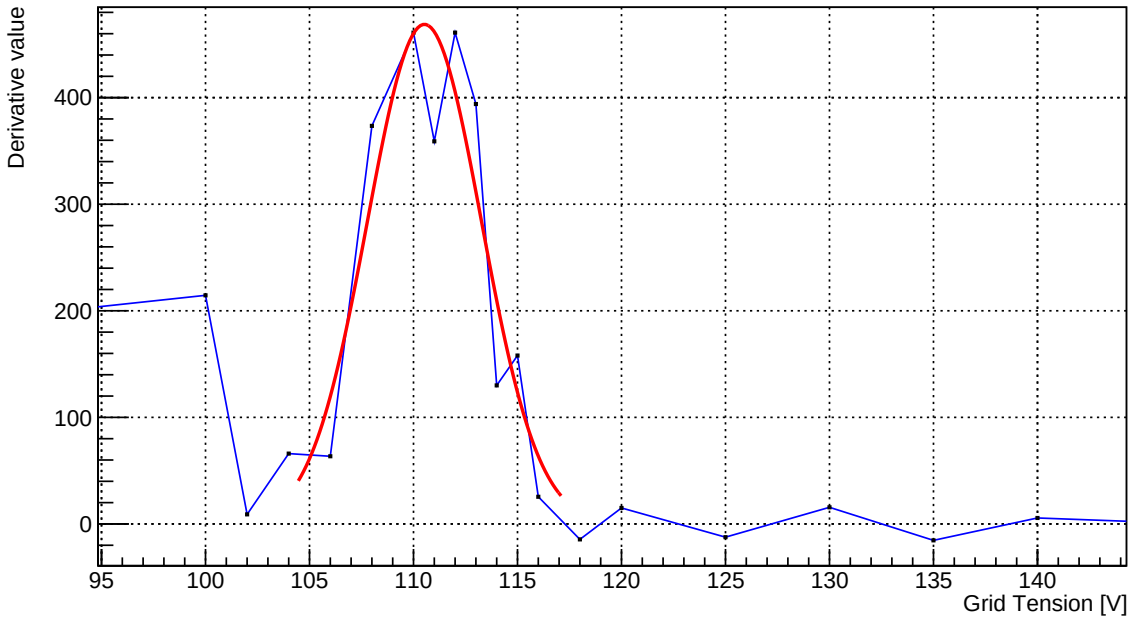

Figure 5.13 – Derivative of the energy dispersion. The mean energy is determined according to the maximum of the curve. Here it appears to have a local minimum due to statistical fluctuations. The mean value is determined *via* a fit which can be seen in red.

vacuum pump and then, once it is done, the gas can flow inside a filter first and then inside the chamber with the help of a millimetric screw. This tool controls the gas flux to avoid reaching a pressure high enough to trigger the security procedure ($P > 10^{-4}$ mbar). A known factor provided by the manufacturer enables to correct the read pressure for ^{4}He (see Annexe. 9.1).

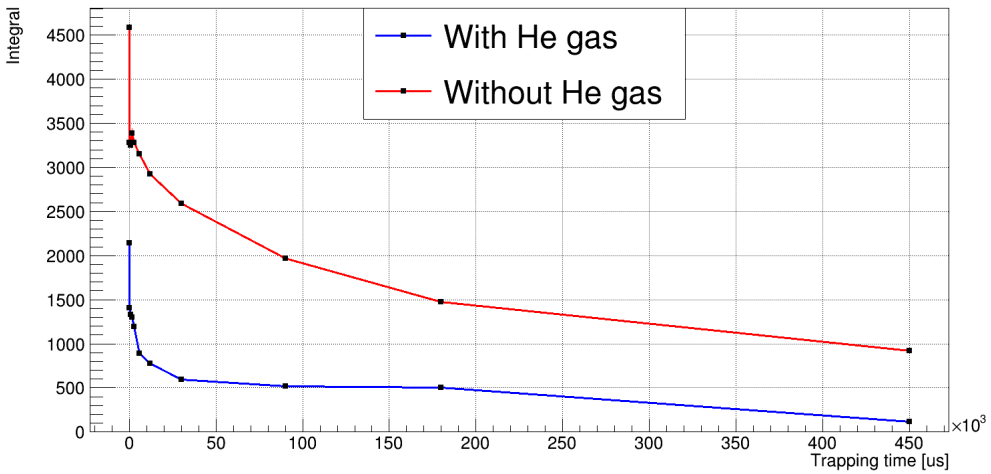

Figure 5.14 – Comparison between the integral of trapped ions peak collected during a 30 s acquisition with and without gas.

According to the results shown in Fig. 5.14, the injection of a ^{4}He buffer gas in the trap reduces the number of trapped ions by a factor of two for fast trapping times and by a factor of three for longer trapping times. Moreover, in the worst case, a difference of 9% in trapping efficiency has been observed between trapping without gas and trapping with gas. A difference of 1.7% has been observed between the two configurations in the best case so far. However, we can see that at short trapping time, the cloud is successfully cooled according to the decaying behaviour of the blue curve compared to the red one. The fact that we lose trapping efficiency can be eventually explained by the radial characteristics of the source. If the beam is focused enough then the contact with the buffer gas can scatter the beam's radial shape leading to a loss of ions during the trapping. The helium gas destabilises the cloud too much leading to loose ions instead of improving the trap. It is important to mention that due to a very tight schedule of the commissioning, the impact of the gas was not investigated further. A dedicated study has been conducted in Sec. 4.6 of [Goy23]. Nonetheless, the analysed data taken in Chap. 6 have been with a ^{4}He gas cooling.

Trapping time	***Integral without gas***	***Integral with corrected gas value (1.5×10^{-4} mbar)***
60 µs	4584	2142
300 µs	3278	1406
900 µs	3250	1329
1.5 ms	3389	1300
3 ms	3278	1197
6 ms	3149	892
12 ms	2920	773
30 ms	2587	597
90 ms	1965	520
180 ms	1478	500
450 ms	919	144

Table 5.5 – Comparison between the number of counts with and without gas with the increase of the trapping time duration. All the measurements have been done within 30 s acquisitions.

5.3.4 Global optimization

From the moment the first trapping was carried out, it was only a question of improving the trapping efficiency: ξ_{trap}. This optimization and refinement process will be detailed in this section.

As seen earlier, SIMION has given great progress although some discrepancies are present between the experiment and the simulation. However, for the optimization of the line and the transmission, we only used the number of ions per second, while for the trapping efficiency, we have chosen to take into account the integral of the hits obtained after a determined and constant duration. One way to increase the number of ions trapped is to increase the number of ions that arrive in the trap. Thus, a search for optimization of the line was carried out at the level of the major devices along the line, namely the combination of voltages of

the PDT2, the Einzel lens, and the voltage of the first PDT. These results are shown in Annex (see Tables 9.1 and 9.2).

Thanks to these successive optimizations, we have increased the efficiency from ξ_{trap} = 8.4% to ξ_{trap} = 14%. Another contribution, which allowed to increase significantly the trapping efficiency, is the RF voltage applied on the R1 and R2 electrodes of the trap. As we have seen earlier thanks to Eq. 4.19, increasing this voltage increases the depth of the potential well and thus better confines the ions cloud. An efficiency of ξ_{trap} = 38.9% was thus reached for a trapping time of 60 µs. For 1 ms of trapping time, the efficiency decreases until reaching ξ_{trap} = 23.7%. Finally, by adjusting the voltage applied to R4, we were able to reach ξ_{trap} = 45% trapping efficiency. This parameter is very sensitive we had thus to be extremely precise by applying the voltage on this electrode (see Table 9.3b). By applying successively all these optimizations, a trapping efficiency of ξ_{trap} = 56% for a short trapping time was reached, as shown in table 5.6. Given the time spent on these optimizations, achieving such a high efficiency was very encouraging for the rest of the commissioning process.

Trapping time	***Trapping efficiency***
60 µs	56%
90 ms	22%
495 ms	10%

Table 5.6 – The best trapping efficiency for different trapping times.

5.4 Commissioning at IGISOL

Located in the experimental hall of the physics department in Jyväskylä, the IGISOL line is mainly operated and diagnosed by students and young doctors, bringing a great deal of technical knowledge and independence to the students.

IGISOL stands for "Ion Guide Isotope Separator On-Line" and it is a technique which was conceived in the '80s. Thought as a novel variation to the helium-jet method, it has been used to provide radioactive beams to probe the nuclear structure of short-lived exotic nuclei. Upgrades are often made on the line [MDÄ14], opening the way to study lighter nuclei giving to MORA a fitting place within this facility.

The MORA set-up was stored in boxes before being shipped in October 2021. This shipping has been catastrophic since the box that contained the vacuum chamber, trap, and detectors fell to the ground. This regrettable incident was fortunately not serious, but required to check the status of everything, starting from the chamber to the detectors themselves. In December 2021, the MORA set-up was shipped again to the IGISOL facility at Jyväskylä. The installation of the chamber was performed by the technical team of the LPC CAEN in January 2022.

Here the MORA set-up is slightly different. Indeed, to allow the polarisation, the MCP2 detector needs to be set off-axis[4]. This involves the use of a deflector after the second silicon detector. This deflector consists of two electrodes powered by opposite voltages, with one attracting the ions while the other repulsing them.

5.4.1 Installation of the experiment

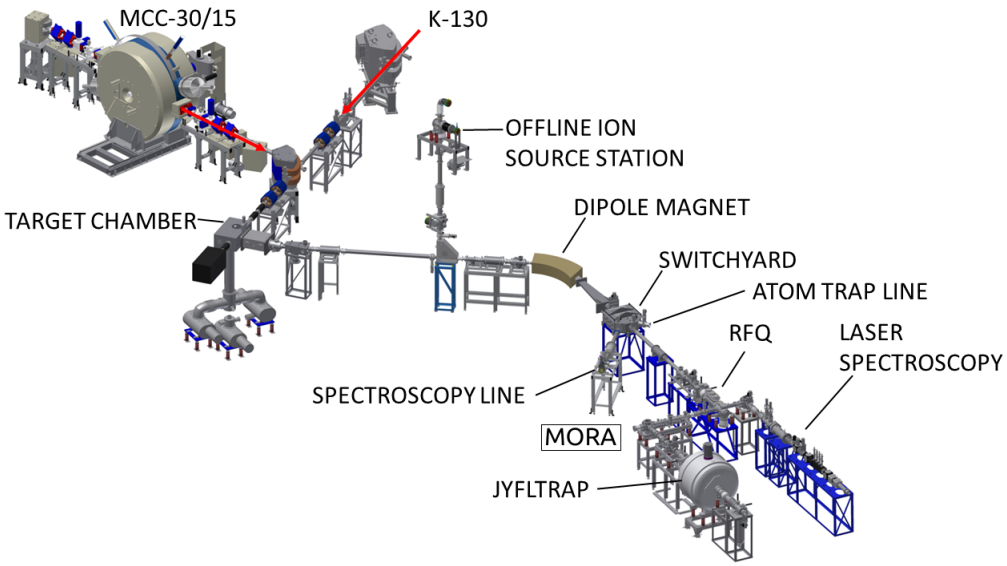

Figure 5.15 – IGISOL layout as it was in 2019. The MORA experiment is placed as indicated.

[4]The axis being the beam axis.

According to Fig. 5.15, MORA is located in the continuity of the trap line, i.e at 90° from the JYFLTRAP direction. The features depicted in the above Fig. 5.15 are important as they are mentioned several times in this text. At the entrance of MORA, there is a cross-tube where a bender serves to direct the ion bunch either towards the Penning trap or towards MORA. This cross was also used to install a stable ion source for commissioning (see the dedicated Sec. 5.4.2).

Diagnostic

The trapping efficiency and the energy dispersion tests are performed in the exact same way as for the LPC Caen commissioning. Hence, they will not be re-explained here. The IGISOL trap line includes two benders, a MR-TOF-MS and some lenses and steerers to keep the beam correctly focused. During the commissioning and more specifically during the beam times, a diagnostic concerning the amount of current can be done along the line. Located at a key point in the entire line, the Faraday cups can be inserted, thus stopping the beam but allowing to collect the number of particles going through, *i.e*, the current (usually in nA range).

5.4.2 Offline commissioning

In order to evaluate the reproducibility of the line in a brand-new environment, several stable sources of different types were used:

- A laser ablation source.
- A surface ionization source.
- A spark source.

5.4.2.1 The laser ablation source

It consists of a pellet of regular NaCl salt (shown in Fig. 5.16) placed in a rotating engine that is controlled remotely. By doing a small rotation movement, this device allows the target not to be severely damaged by the laser beam. A skimmer is placed directly after the pellet holder, a first Einzel lens can be found just before a bender. Two steerers are located just after the bender cross to make sure the beam is shooting straight before entering MORA. The laser used for this source is a YAG laser driven at a frequency of 10 Hz. The diagnostic of the beam was performed on a Faraday cup placed straight ahead compared to the bender and then directly on the MCP1, by connecting the first attenuator grid to a picoamperemeter in the line itself. Unfortunately, the ^{23}Na has high ionization energy compared to the other metals referred to in Table 5.1. As a result, the laser has been set at the maximum power to see the effect of the current. This means reducing the time duration between the laser amplification and the release of the laser beam until reaching the minimal duration of 200 µs. It appeared that a threshold effect has been noticed since for $\Delta T > 210$ μs no ions have been observed. This powerful ionization has induced sparks, resulting in huge fluctuations in the main voltage of the line. Luckily, another metallic pellet, was installed on the rotating engine allowing us to continue the tests. Those were qualitative, however, since the mass is different from that needed to calibrate the line and the trap. The goal of these tests is just

Figure 5.16 – Salt pellets before (on the left) and after grinding (on the right) to fit in the pellet holder.

to succeed in slowing down ions correctly. The main difficulty is to determine the mass of the element ionized by the laser. This one was unknown, making the calculations of switch time particularly complex. Pursuing the calibration process was unnecessary since the mass of the element was not well defined, thus another kind of offline source has been chosen.

5.4.2.2 The surface ionisation source

Surface ionisation sources have been placed at two positions (see Fig. 5.17). The first one is at the exact same spot that the skimmer in front of the laser ablation source. Indeed, the surface ionisation pellet is installed with its own skimmer. The other sodium pellet has been placed upstream of the RFQ cooler buncher. The goal was to inject the ions inside the RFQ for its tuning. Since it became a bunched beam, this pellet has been used for tuning the line with a much more realistic behaviour. These two pellets are those that have been used for the LPC Caen (line) and GANIL (RIDE detectors) commissioning:

- The LPC Caen pellet is placed between the switchyard and the RFQ (see Fig. 5.15).
- The GANIL pellet is placed before the bender of the cross at the entrance of the MORA line (see Fig. 5.15).

During the commissioning at LPC Caen, the pellet was composed of three elements, ^{85}Rb, ^{39}K, and ^{23}Na (see Sec.5.1.2). Some calculations have been done in order to find which element the MCP1 was detecting. Since we knew the time of flight and the energy, we could determine the element:

$$v_{ions} = \sqrt{\frac{2 \times E_{ions}}{m_{ions}}} \approx 13859 \times \sqrt{\frac{E_{ions}}{A}} \tag{5.2}$$

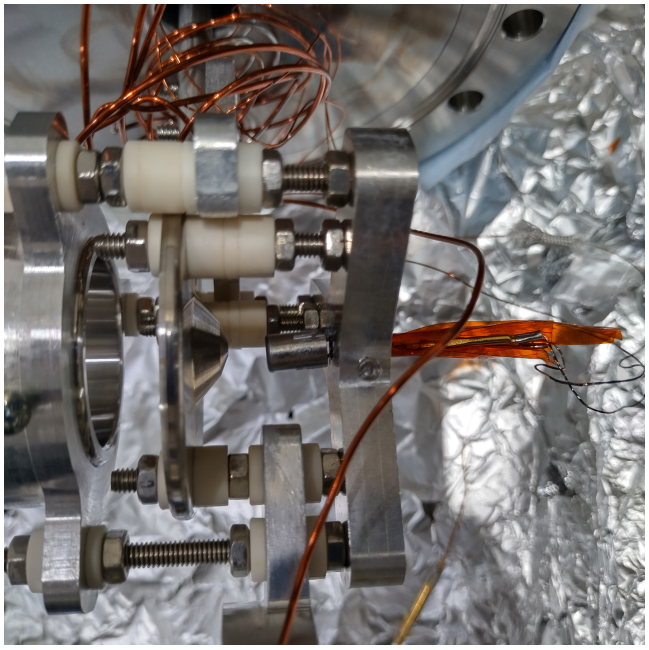

Figure 5.17 – Surface ionization pellet used at IGISOL. The Kapton is for preventing the two electrodes from touching each other.

With A the atomic mass, E in eV, and the 13859 factor including all conversion factors passing from Joules to eV and from kg to amu. However, despite a current of 3.8 nA, it appeared that, according to the TOF measured on MCP1, potassium was privileged. After a few tries, no sodium was detected whatsoever due to an exhaustion of the sodium sample.

5.4.2.3 The spark source

We finally used a spark source located at the target area to mimic the real travelling of the radioactive ions. The spark source consists of a thin sodium sample placed on an electrode in a gaseous environment[5]. In the electrode, an alternating current is set. According to Paschen's law, the sparking voltage is reached and a spark occurs between the two electrodes, *i.e* on the sodium wire as illustrated in Fig. 5.18. Ions are extracted by a skimmer electrode and sent into the line, after passing through the magnet for beam purification. As mentioned, it is heavily dependent on the gas pressure, as such the more pressure inside, the more ionization. More statistics resulted from such an increase, however, the sodium sample is drastically shrunken. A new sample had to be placed every two or three days of use. With such a source, the MORA line efficiency of 62.5% could be achieved alongside a trapping efficiency of 15.2% at $V_{RF} = \pm 65$ V and at $\nu = 0.33$ MHz, for a cycle of 60 μs. We obtained a traaping efficiency worse than in LPC Caen due to the complexity of the IGISOL line. It is important to know that this source was tested only few days before the first beam time.

[5]Helium in our case.

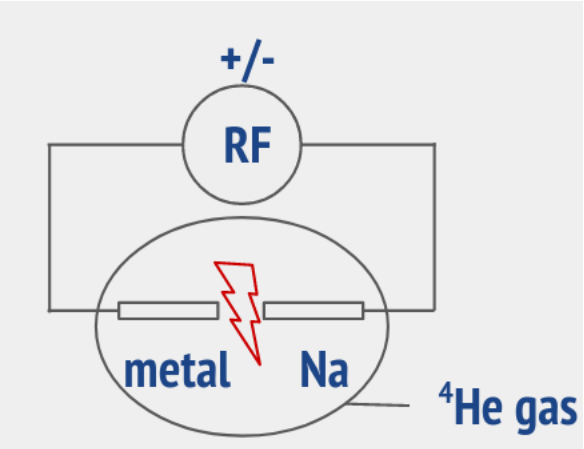

Figure 5.18 – Scheme of the principle of the spark source.

5.5 Online commissioning

5.5.1 18-20 of February 2022

Once the line has been properly set with the help of the spark source, the 30 MeV proton beam is sent to a ^{24}Mg target removing a neutron from the target thus creating ^{23}Mg and a deuteron (^{24}Mg(p,d)^{23}Mg). The flux of the radioactive beam is extracted from the target area with the help of the SextuPole Ion Guide or SPIG. It is then sent to the RFQ where the continuous beam is bunched by the end-plate[6] of the mini-buncher device.

The mini-buncher is a technology developed by IGISOL, its principle rests on successive alternating "gates" and wells of potential shown on Fig. 5.19.

Three gates and two wells are created. The first well aims to bunch the beam by cooling it down thanks to a high buffer gas pressure in red in Fig. 5.19. The bunch is then transferred to the second potential well (see the green line), closing the second gate and opening the first one again in order to create a new bunch (the red potential is then applied). When the first bunch is sent through the line and re-accelerated up to 30 keV (see the blue potential), the second bunch goes to the second well (red potential), re-doing the process over and over. The beam is driven to the entrance of MORA and slowed down by the process explained in section 5.1.3.2. However, the procedure is slightly different. Indeed, the original way to slow down the ions was to use the PDT1 switching from a high positive potential (28 kV[7]) to a negative one (-500 V). This procedure is possible thanks to its dedicated SPELLMAN power supplies which can endure such rapid switches. Nevertheless, the switch was inducing a huge fluctuation in the JYFL line potential changing the beam kinetic energy. The beam which had been calibrated with an offline source was not useful since the TOF did not correspond to the calibrated values anymore, hence making impossible the trapping process. One solution has been found and consists of plugging the positive entry of the PDT1 directly on the

[6]The mini-buncher was not operational at that time so the bunch have been done by the endplate, leading to a large bunch (see later in the text). The mini-buncher, however, has been used for the rest of the beam times presented in this document.

[7]This high voltage comes from the difference of volatage applied in the HV plateforme(IGISOL line) and the MORA line

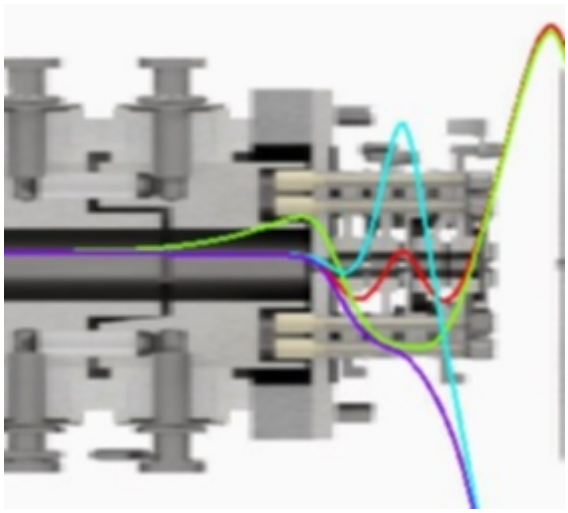

Figure 5.19 – Screenshot of the EPICS module of IGISOL where different potentials applied are shown. The red is the push-plate accumulation, the green one is the transfer to the buncher, the blue one is the push-pull extraction and the purple one is the sum of all potentials.

IGISOL line. This makes sure the PDT1 has the same tension as the rest of the IGISOL line leading to getting rid of the fluctuations. During that period of time, the beam was highly contaminated: 2000 to 20000 of ^{23}Na for one ^{23}Mg. This diagnostics has been done with the help of Silicon detectors placed along the line before the MORA one. To conclude, we have ended up with the following result for the first beam time:

Trapping efficiency	***Trapping duration(ms)***	***Line efficiency***	***Contamination factor***
5-50%	500	$10^{-4} - 10^{-5}$	∼20000 to 2000

Table 5.7 – Different characteristics of the MORA first online beam. The transmission through the line was very low due to the fact that the buncher was delivering a very large bunch (20-100 µs) and the tuning of the mini-buncher was challenging for light elements.

5.5.2 27-31 of May 2022

Strong efforts have been deployed to attempt to improve the contamination ratio. As a result, both the target head and the target window have been cleaned by an ultrasound bath and baked under vacuum. The cleaning contributed to reducing the contamination ratio, leading to a yield ratio of about 2000 to 500 for ^{23}Na to ^{23}Mg.

Another attempt was made by using the MR-TOF-MS located in the trap line before MORA. The goal was obviously to purify the beam but also to look at the contamination ratio and the number of ^{23}Mg that was remaining. Fortunately, the efficiency to separate contaminants from ^{23}Mg was close to 100%. It was leading up to a number of radioactive ions of 100 from a 10^5 originally. The remaining beam, cleared from contaminants, was containing not enough ^{23}Mg to be properly trapped regarding the successive efficiencies of the line then of the trap. Of course, ideally, this purification process has to be coupled with

a rebuncher to be able to accumulate a better statistics before entering the line. One of the solution is also to install the MR-TOF-MS before the mini-buncher, making the rebuncher process done by the min-buncher. Even though this option was not taken into account now, it may be used for future beam times especially if the contamination ratio can not be improved whatsoever.

Compared to the first beam time, the mini-buncher has been improved allowing to deliver much shorter bunches passing from 100 μs to 500 ns. The PDT1 huge fluctuations were mitigated by a large capacitor, leading to an overall efficiency of up to 10% of the initial beam measured at MCP1 after being slowed down by our first PDT. A trapping efficiency from 30% to 100% has been measured at the MCP2 after being slowed down by the second PDT. This large difference of trapping efficiency can be explained by a low statistics. The efficiency from the mini-buncher to the trap was 1 to 5%. Finally, according to the number above, from an initial beam containing 10^5, we only get 1:500 contamination ratio leading to 200 ^{23}Mg per bunch from the mini-buncher. By taking into account the overall efficiency of the line, it gives 10 ions successfully trapped, which is a factor 1000 lower than the targeted value for MORA [Del+19b]. These results are shown in Table ??.

PDT1 to MORA Trap efficiency	***PDT2 to MORA trap efficiency***	***Overall efficiency***	***Trapping duration***	***Number of ^{23}Mg trapped/bunch***
10%	30% to 100%	1% to 5%	500 ms	∼10

Table 5.8 – Overview of the efficiency of the second online beam time. The first efficiency is measured from the MCP1 to the MCP2 without trapping. For the PDT2, the efficiency has been measured by the MCP 2 without the trapping process. Finally, the overall efficiency led to 5% at max. with the trap.

The bunch has then been trapped during 500 ms without losses. This has been made possible by changing the radio-frequency amplifier of the trap since the previous one broke. The new one is way simpler and better since it directly gives a perfect sinusoidal waveform for the radio frequency instead of the fins-shaped waveforms (see Fig. 5.9). This new amplifier, a WMA-300 model from Falco Systems, is triggered by an external signal sent by the slow control to generate the waveform of the RF up to $\pm 150\ V$.

We have also noticed a discrepancy in the number of counts detected by the MCP1 as a function of the number of attenuators placed inside the line (see table 5.9).

The conclusion of the last table is alarming, meaning that we can not rely on online acquisition about the different efficiencies inside the line. It does not concern the Faraday cup or Silicon detectors placed in the IGISOL line before MORA line.

5.5.3 10-13 of November 2022

For this beam time, the target head and target itself have not been baked in the oven but have been cleaned since the last beam time. The first attenuator has been replaced by a Si detector in order to be able to probe the beam contamination directly in the line. A way to get rid of the contamination was also to look for the 2^+ charged state of the ^{23}Mg. Previously, sodium and magnesium always had been selected via their 1^+ state. Unfortunately, no 2+

Nb of attenuators	*Attenuation factor*	*Ions in 1 min*
4	10000	94
3	1000	490
2	100	5475
1	10	51645
2 (middle one)	100	4391
3 (middle + back)	1000	478

Table 5.9 – Different numbers of counts integrated over 1 min. The attenuators are just mechanical grids that, obviously can be damaged but not with a beam with this intensity ($<$ 1 nA). It was probably resulting from a pile-up effect from the MCP itself that the online acquisition read-out was struggling with. Regarding the value shown here, one has to determine at which rate the MCP is not saturating. One way to figure out, is to evaluate the pile-up depending on the beam focus. This can be done by focusing/defocusing the beam on purpose with the Einzel lens on the MCP1, since one can see the beam shape on that device.

state has been observed during the beam time, keeping the contamination ratio down to 1000 after three days of beam. A global efficiency of 10% from the buncher to the entrance of MORA was measured. The MCP used in an expected unsaturated mode showed a trapping efficiency between 1 to 15% due also by low statistics. The number of trapped ions has been confirmed by the Si detector of about 20 ^{23}Mg trapped per bunch.

Concerning the trapping half-lives, the trapping efficiency has been optimized to be able to trap up to 2 s without losses, as described in table 5.10.

Trapping time	*Counts*[8]
130 ms	2913
1030 ms	2712
2030 ms	3018
11030 ms	1144

Table 5.10 – Number of detected trapped ions for different trapping times. The number of counts stays comparable until 2 s of trapping.

An 11 s trapping has been achieved, proving the cloud can be trapped as long as the magnesium half-life time. After an overall optimization of the trap and the line, around 30 hours of data were taken (see chap. 6).

On top of that, three hours of environmental background were also taken using the same line set-up, trap, and laser beam but without the radioactive beam. To conclude these measurements, 12 hours of calibration were taken with the help of the offline radioactive finger-shaped source[9].

[9]This device has already been introduced and can be seen in Fig. 3.8

5.6 Comparison with SIMION simulations

The studies made with SIMION on the commissioning of the line in the IGISOL configuration are only qualitative since approximations are made on the beam shape. Indeed, at first and also because the geometry of the Finnish line was not known at that time, a circularly and uniformly distributed beam with a bunch duration of the order of 500 ns was assumed, which has been observed experimentally[10]. In the simulation, the beam is created shortly before the bender so that it travels a minimum distance before entering the clean part of MORA. Due to the different approximations, the transmission is perfect and all the ions produced are carried in the line. This is unfortunately not the case experimentally. The role of these simulations is to study the behaviour of the ions in the line and in the trap with the latest experimental parameters. Thus, all the voltages have been adjusted accordingly. The only difference between the two is the timing of the R4 electrode, the so-called stop electrode. It is shorter by 1 µs in the simulation than in reality due to the difference of beam shape.

However, contrary to the trapping tests carried out at LPC Caen, the radio-frequency field is switched on during the injection phase of the ions into the trap, since an increase in the trapping efficiency has been observed in this case during tests at IGISOL. Indeed, by injecting the bunch directly on a high-phase of the RF, the trapping process will be more efficient instead of just trapping after an injection phase. To do that, the electrodes R1 and R2 are set to their positive nominal voltages, and then when the bunch leaves PDT2, the RF is triggered. Just keeping the voltage parameters as they are, we obtain a trapping efficiency between 38 and 45% (for 1000 ions). Nevertheless, an increase of 500 V on the extraction electrode allows a theoretical gain of about 20%. However, this increase in voltage; and thus an increase in ion energy; implies adjusting the voltage of the trap output deflectors as shown in Table. 5.11.

To determine the effective loss of ions during trapping, the voltage of the trap output deflectors was deactivated. By doing so and by setting a condition on the spy detection plane, it is possible to take into account only the ions emitted during a time shorter than the extraction time. Thus, out of 1000 initial ions, 10% were lost during trapping and in this direction. About 20% are also lost in the deflection of the ions and an overview of these results is shown below in table 5.11.

[10] Only the temporal emittance.

Trapping time	***Nb of detected ions***	***Trapping efficiency***	***Operation***
500 μs	111	**N/A**	Ions detected while trapping
500 μs	380	380/1000=38%	$V_{\text{defl}} = \pm 650$V; $V_{\text{extract}} = 1000$ V
500 μs	736	(736-111)/1000=62.5%	$V_{\text{extract}} = 1500$ V
500 μs	673	(673-111)/1000=56.2%	$V_{\text{extract}} = 1500$V; $V_{defl} = \pm 700$ V
500 μs	697	(697-111)/1000=58.6%	$V_{\text{extract}} = 1500$ V; $V_{defl} = \pm\ 750$ V

Table 5.11 – Study of trapping efficiency with different parameters. V_{extract} represents the voltage set on the R3 electrode in order to extract the ion from the trap. The usual $V_{\text{defl}} = \pm\ 650$V.

5.6.1 Conclusion:

The commissioning of the experiment took place into two stages. The first phase was carried out at the LPC Caen using stable sodium sources. These preliminary tests were MORA's first baptism of fire, as its entire operation was put to the test. SIMION simulations enabled the first ions to be trapped without too many difficulties.

After a laborious move (also carried out in two stages), MORA was installed in IGISOL's experimental hall in Jyväskylä, Finland. There, and with the help of several sources, offline tests were first carried out to ensure that the experiment was working properly. Since the installation, three beam times have been dedicated to taking data with ^{23}Mg radioactive isotope. Of the three, only the most recent was able to produce a dedicated analysis which is detailed in Chap. 6. An overview of the results acquired at JYFL is shown in table 5.12.

Beamtime	ξ_{line}	ξ_{trap}	***Trapping time***	***Number of ^{23}Mg trapped/bunch***
February	0.03%	5-50%	500 ms	∼4
May	10%	5%	120 ms	∼10
November	10%	1-15%	2 s	∼20

Table 5.12 – Summary of the trap efficiency reached during the different beam times.

Finally, in view of everything that has been achieved on MORA, from the first commissioning to the last beam time, we can conclude that the experiment is working as it was initially designed. In a future free of this contamination, we can only be seriously optimistic about MORA's ability to demonstrate the polarisation of the cloud and then establish its first measurements of D.

Chapter 6

First data analysis

This chapter is dedicated to the analysis of the data taken during the November 2022 beam time. First, a short presentation of the fine and hyperfine structure is presented to make the following study more understandable. Then, the way we have acquired the data and the method used to analyse them is explained, especially the way the background is removed.

6.1 Ion cloud polarisation

To be sensitive to the D parameter, the ion cloud has to be polarized. To do so, the cloud is enlightened by a laser beam that will probe the hyperfine structure of the $^{23}Mg^{+}$. Before entering into the details of the hyperfine structure, the fine structure is introduced.

6.1.1 The fine structure

The ^{23}Na, for instance, is very convenient to illustrate the fine structure since its electronic structure is the one of the Neon plus one electron. Since the neon electronic configuration is a closed shell configuration, only the valence electron contributes to the total orbital momentum such that $\vec{L} = \vec{l}$ and the spin angular momentum $\vec{S} = \vec{s}$. The total angular momentum can then be written as $\vec{J} = \vec{j}$ with $\vec{j}$ being included between:

$$|l - s| \leq j \leq l + s \tag{6.1}$$

with the angular momenta of one electron written in lower letters as $\vec{s}, \vec{l}$ and $\vec{j}$ whereas the angular momenta of the atom are in capitals as $\vec{S}, \vec{L}$ and $\vec{J}$.
The different values of $\vec{J}$ lead to the different energies of the states resulting from the spin-orbit (SO) interactions. This splitting of states by the SO interaction is called the fine structure of the atom. By transposing this notion to our example and by using the Russel-Saunders notation ($n^{2S+1}L_J$, where n is the principal quantum number, S the electron spin angular momentum, J the electron total angular momentum), the lowest state of the sodium can be written as $3^2S_{1/2}$. The first excited state corresponds to the change from the 3s shell to the 3p one. Therefore, the first excited state can be written as: $3^2P_{1/2,3/2}$. We were just looking from an atomistic level to the ^{23}Na energy levels. If we add now the nuclear spin to it, the system becomes a bit more complex.

6.1.2 The hyperfine structure (HFS)

The structure of the atomic atoms becomes more complicated when the nuclear spin $\vec{I}$ interacts with the total angular momentum of the electrons $\vec{J}$ to form the total angular momentum as $\vec{F} = \vec{I} + \vec{J}$. Here, a very handy parallel can be drawn between the fine structure (FS) and the hyperfine structure (hfs). In the same way as for $\vec{J}$, the different values of $\vec{F}$ lead to the different energies of the states resulting from the interaction between $\vec{J}$ and $\vec{I}$ as: $A\vec{I}.\vec{J}$, with A a parameter defined experimentally [AIV77]. The small shifts of the otherwise degenerate energy levels provide a new structure called the hyperfine structure, generally much smaller than the fine structure because of the small size of the nuclear magnetic moment in comparison to the atomic one.
For each state of J, the interaction with I leads to $(2I + 1) \times (2J + 1)$ sub-levels called Zeeman sub-levels. To illustrate it, the ^{23}Na atom has a nuclear spin of $I = 3/2$ which leads to 8 Zeeman sub-levels in the ground state with $J_{gs} = 1/2$. However, those sub-levels are degenerated without any perturbation. An external field, like an electromagnetic field induced by light, can lift the degeneracy as presented in Sec. 1.2.1 of [MV99].

This phenomenon is the well-known Zeeman effect [Zee97]. The energy level shifts ΔE between two sub-states are proportional to the strength of the applied magnetic field as:

$$\Delta E = g\mu_B MB, \tag{6.2}$$

where μ_B is the Bohr magneton, M is the projection of the angular momentum along the axis of the magnetic field applied, and B is the magnitude of this field. The parameter g is the Landé g-factor which is expressed as:

$$g_j = 1 + \frac{J(J+1) + S(S+1) - L(L+1)}{2J(J+1)}, \tag{6.3}$$

and yet, due to the presence of the nuclear spin, the g-factor is slightly changed into:

$$g_F = g_j \frac{F(F+1) + J(J+1) - I(I+1)}{2F(F+1)} \tag{6.4}$$

Concerning our example, the ^{23}Na, the nuclear spin I is equal to 3/2, giving F values equal to 1 or 2 for the ground state thanks to the following formula:

$$|I - J| \leq F \leq I + J \tag{6.5}$$

Since J is either 1/2 or, 3/2 for the excited states, F can take the values 0, 1, 2, and 3. It results that it gives m_F sub-states (with m_j= -F,...,m_j=F) since:

$$\hat{F}_z |\psi\rangle = \hbar m_F |\psi\rangle \tag{6.6}$$

where $\hat{F}_z$ is the contribution of the operator of the total angular momentum on the z-coordinate and $|\psi\rangle$ is the wave function

For the MORA experiment, the nucleus of interest is ^{23}Mg. By populating the $m_F = \pm 2$ state of the ^{23}Mg, we make sure to have the contribution of the alignment of both the nuclear spin I and the total angular momentum J of the electronic cloud. These states can be populated by a circularly polarised optical pumping, here represented by the $\sigma+$ or $\sigma-$ symbol. Of course, this must obey to selection rules here $\Delta M = \pm 1$, where (+)-sign is for right-handed and (-)-sign is for left-handed for circular polarised light. Since photons carry angular momentum, their projection on the z-axis can be 0, ± 1. Moreover, the conservation of angular momentum implies a modification of a change in the projection of the angular momentum of the atoms. In our case, the $\sigma+$ configuration allows us to access the $m_F = +2$ state which means both of the momenta are aligned along the beam magnetic field. The $\sigma-$ configuration reverses the alignment of the spin which is now anti-parallel to $\vec{B}$.
These notions are illustrated in the Fig. 6.1. Reversing the laser polarisation will reverse the ion spin direction allowing us to measure the polarisation degree of the ion cloud and D by extension (see 3.2.6). This can be done experimentally by simply adding or not a half-plate in the laser beam path. The laser table can be seen in Fig. 6.2

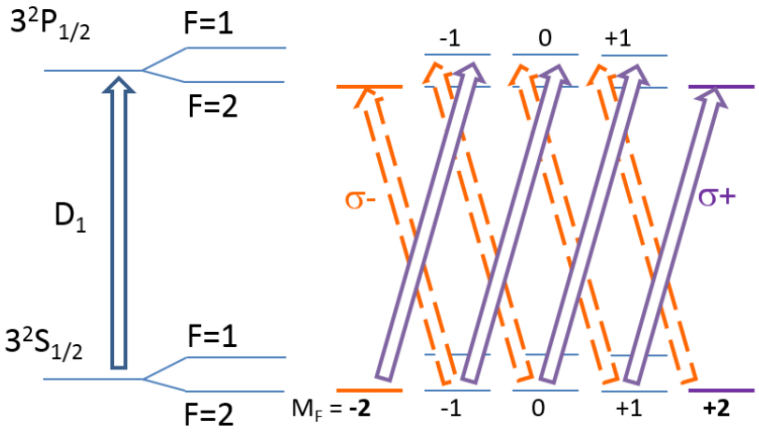

Figure 6.1 – Hyperfine transitions used to orient the spin of the $^{23}Mg^{+}$. This figure is coming from [Del+19b].

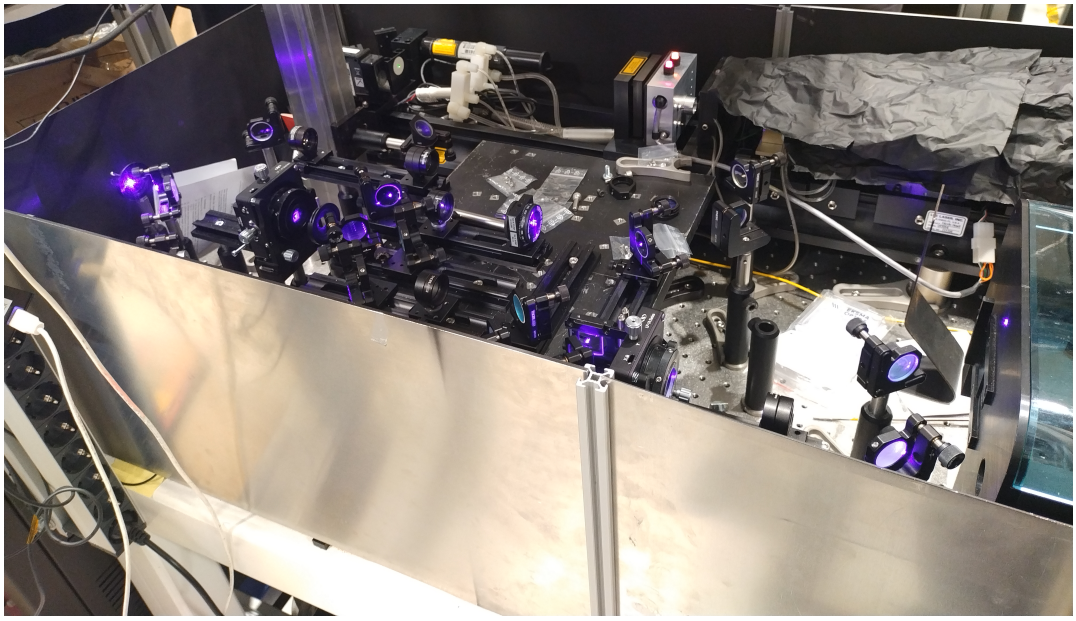

Figure 6.2 – Picture of the laser table used for the cloud polarisation.

6.2 Evaluation of the polarisation degree

The November 2022 campaign of measurement was successful (see Sec. 5.5.3)in the way that a large sample of data has been registered. Three configurations of files have been acquired:

- Laser-on with half-wave plate, known as the σ- configuration (11 h) (see Fig. 6.3).
- Laser-on without half-wave plate, known as the $\sigma+$ configuration (8 h).
- No laser (7 h).

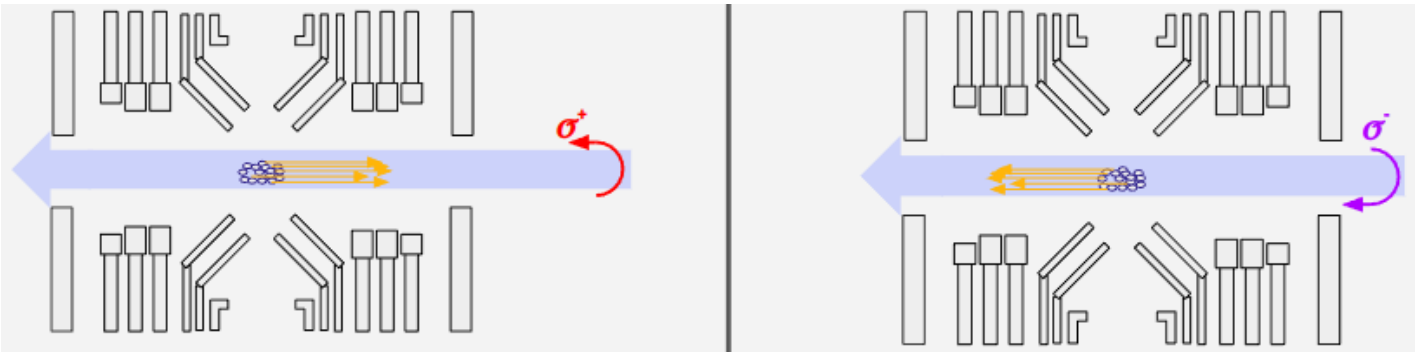

Figure 6.3 – Illustration of the laser polarisation, the nuclei and the laser beam have been magnified for visibility. Here the blue arrow symbolises the laser beam and, depending on the polarisation, the nuclear spin is either parallel or antiparallel to the beam direction here shown with yellow arrows. The Silicon detectors can be seen on both sides of the traps just after the Einzel lenses. The circular arrows represent the circular polarisation of the laser beam.

After the experiment, a 3 hours run of background was also taken in the same conditions as during the radioactive beam time. The cycle is 3 s in length, and during the cycle, only 2 seconds were used for trapping the radioactive ions (see Fig. 6.4). The last second

was, indeed, used to measure the radioactive background from non-trapped ions during the experiment. As a result, we end up with two kinds of backgrounds:

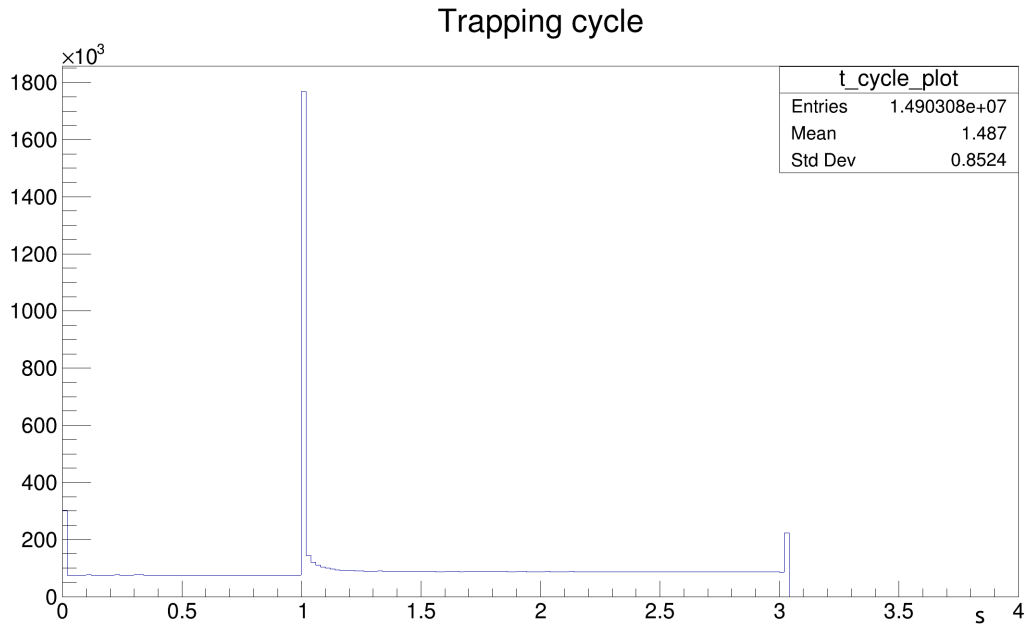

Figure 6.4 – Histogram of the typical cycle used during the experiment. Here the first second aims to measure the radioactive background contrary to the 2 other seconds during which the ions are trapped.

- The environmental background, present in both cases.
- The radioactive background, only present during the online experiment.

Of course, to end up with clean data, all sources of background have to be correctly removed.

6.2.1 Background analysis

Environment background removing

Starting from the simplest case, the environmental background removal process is straightforward. The idea is to subtract the histogram from the data files with the one from the background file. For this, we stick to the three hours of data, for both background and online data.

Radioactive background

As mentioned before, the trapping cycle is split into two seconds of trapping and one second of background acquisition. During the one second of radioactive background, which will be called b_{rad} in the following, there is an amount of ^{23}Mg which is not trapped and which is freely moving inside the chamber. These offtrap ^{23}Mg have been already decaying during the trapping time and need to be reconstructed within the trapping duration. As a result, once b_{rad} has been cleaned from b_{env}, a negative exponential function fits the data as shown in Fig. 6.5. The fit is performed using the following expression:

$$e^{(A-\lambda t)} = e^{A} \times e^{-\lambda t} \tag{6.7}$$

where A is a constant and λ is the decay constant of ^{23}Mg, here $\lambda = ln(2)/T_{1/2} = 0.06134\,\mathrm{s}^{-1}$. Since there are only a few events to fit on, λ has been fixed in order to help the procedure to fit easily. It results that the constant, A, remains the free parameter. An empty histogram

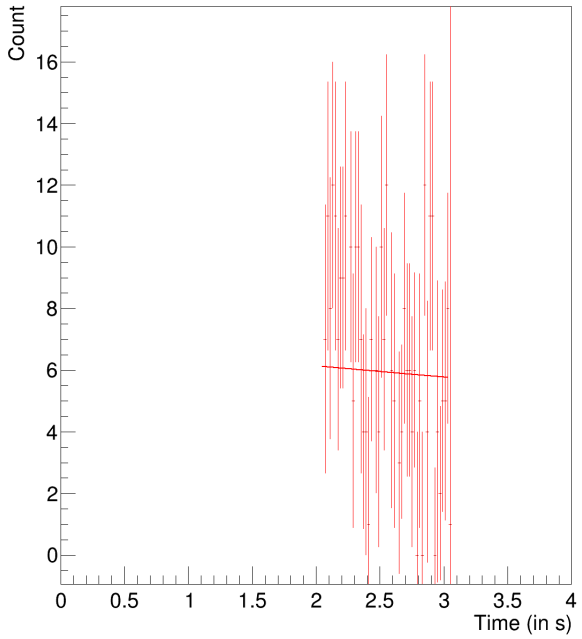

Figure 6.5 – Example of an exponential fit performed on the radioactive background data of the first channel on the Si 1 detector.

is then filled with the exponential function defined by the fit, which is then subtracted to the (data + b_{rad}) histogram, resulting in the histogram shown in Fig. 6.6.

Once done to every channel on both detectors (Si 1 and Si 2), all channels are stacked together in order to get the total spectrum for each detector. Then, the total number of counts is gathered with its error bar. The asymmetry number is retrieved by applying the formula seen earlier (see eq. 3.42).

There are two ways to probe the asymmetry by using this method. Either, the number of counts is summed up for the two silicon detectors for one laser polarisation configuration ($\sigma+$, σ- or no laser), or just one detector is selected and two laser configurations are used. The asymmetry is then deduced by subtracting the number of counts of the different configurations over the sum of them. The results given by this method are compiled in Table. 6.1

Conclusion:

An analysis of the data acquired in November 2022 has been done. Due to high contamination of stable single charged $^{23}Na^{+}$, the amount of data resulting from detecting radioactive isotopes is nothing but meagre. Even though almost 30 h of data have been taken, only a few hours are in the same configuration (laser polarisation and/or trapping cycle).

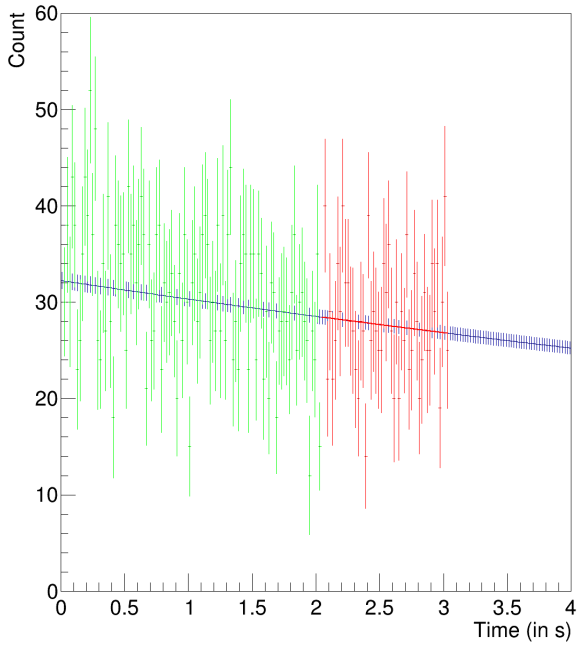

Figure 6.6 – Both sets of data are coming from channel 1 of the Si 1 detector. The green plot represents the trapped data cleaned from b_{env}, and the red plot is b_{rad} also cleaned from b_{env}. The red line is the exponential function.

Configurations	***Si 1***	***Si 2***	***Asymmetry***
2 Detectors with Half-Plate	89.22 ± 85.49	23.91 ± 125.18	-0.58 ± 1.55
2 Detectors without Half-Plate	27.65 ± 94.48	181.99 ± 129.99	-0.74 ± 0.95
2 Detectors Without laser	-82.85 ± 73.69	-116.60 ± 111.35	-0.17 ± 0.68
Configurations	$\sigma+$	σ-	***Asymmetry***
Si 1	27.65 ± 94.48	89.22 ± 85.49	-0.53 ± 1.23
Si 2	180.00 ± 129.99	23.91 ± 125.18	0.77 ± 1.10

Table 6.1 – Table gathering the results resulting from the analysis described above. The table is in two parts corresponding to the two ways to probe the asymmetry. Thus, the first part shows the results for taking both detectors for one laser configuration whereas the other parts are present on the detector for both laser polarisations. The asymmetry obtained is highly dominated by the uncertainties making both the results compatible with 0 and, since the asymmetry must belong to the [-1,1] interval, away from any physical meaning.

Starting from these samples, we have performed a background subtraction method based on fits using a decaying exponential function. After summing up the contribution of all channels, we have ended up with the statement that no polarisation of the cloud has been observed. The contamination in ^{23}Na was too high and prevented trapping enough ^{23}Mg to observe the asymmetry.

A new technical campaign was performed in June 2023 where 4 different targets were tested to reduce the amount of contamination:

- One backed Mg target
- One backed Mg target coated with BaO (∼250 nm)
- One backed MgO target coated with BaO
- One non-backed Mg target for comparison

Sodium was still seen in the beam, however, it appears that the injection of SF_6 gas in the target chamber was creating molecular structures with magnesium ions and possibly allows, thanks to the sorting magnet, better discrimination between ^{23}Mg and ^{23}Na. Since the priority of the experiment is to get a better ratio Mg/Na, another test is scheduled in December 2023 to improve the overall efficiency of the line and of the trap with a ^{24}Mg spark source. If there is enough time, molecular bonding between Mg and F elements will be tested. If the test is successful, the sodium contamination could be simply removed since the mass selection is way upstream from the RFQ. Once inside, the molecular bond can be hopefully broken thanks to the buffer gas. The magnesium can then be purely selected since the masses of ^{23}Mg and ^{19}F being different, the associated TOF would be also different.

Chapter 7

Phoswich calibration and Geant4 simulations

This part is dedicated to the phoswich detector study performed during the thesis. First, a general presentation of the detector principle is given. The calibration procedure is then presented, followed by the various studies investigating the origins of amplitude differences between simulated and experimental data.

7.1 Data acquisition

The data have been taken by a homemade acquisition system. Developed at LPC Caen, the FASTER technology allows handling a data flux up to 7×10^5 signals per second with a rather simple but robust user interface. Concerning the phoswich detectors, the charges collected are sent to the FASTER acquisition card, leading to one channel by Photomultiplier (so 4 channels by phoswich detector). Data coming from a channel have a label which is gathered in a group.

The data are stored in a .fast file which is converted to a .root file depending on their original labels. For the phoswichs, the different charges are separated in "leaves" which can be accessed later by an algorithm. In the framework of the experiment such as presented in Sec. 5.5.3, a T_0 signal is sent to the slow control, corresponding to the moment when the RFQ-CB sends the bunch through the line. Then, all the timings set in the line are based on this T_0.

Once the trap is working, it defines a T_1 signal to the FASTER acquisition cards to register the upcoming events. This creates the $T_{0_{data}}$ which is thus different of the $T_{0_{line}}$. This $T_{0_{data}}$ sets the T_{cycle} defined in the next chapter. From the T_1, all the channels from all detectors are registered in a .fast file up to a 2 Gb size. When it reaches this size, the software puts the data in a buffer while it creates a new file. Once done, the software fills the file with the buffer data and the acquisition returns to normal.

7.2 Phoswich detectors

The MORA set-up contains four detectors that aim to detect β particles and discriminate γ particles (see Fig. 7.1 for a closer view of the detector and Fig. 7.2 for the view in real

conditions). These detectors are made of four independent and identical structures made of 2 plastic scintillators held together mechanically (named Phoswich) and one photo-multiplier (PM). The characteristics of both scintillators can be seen in Fig. 9.2.

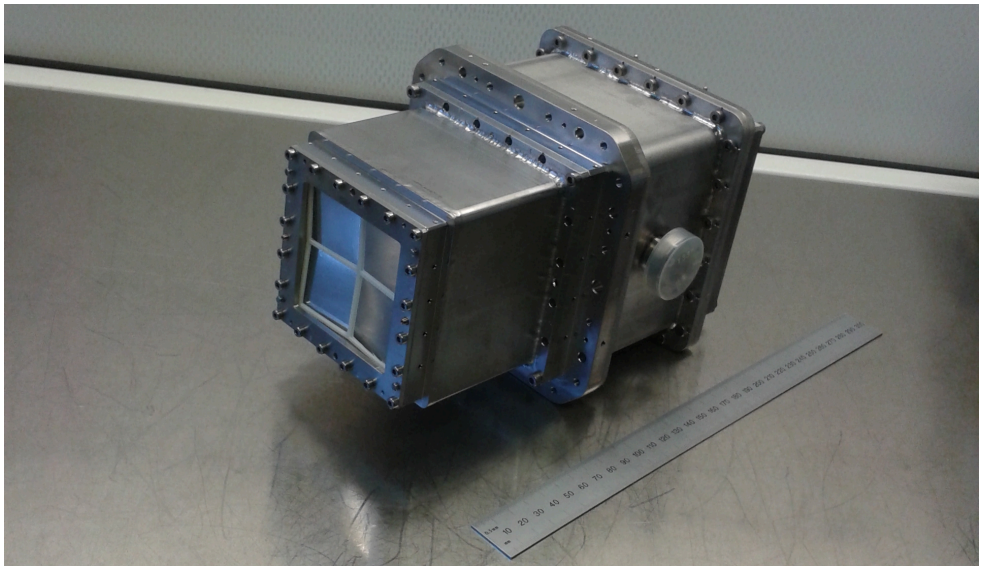

Figure 7.1 – A picture of a phoswich detector with a ruler for the scale. One can see the four modules on which a mylar window is placed. It is important to notice that in the final design, another mylar window is placed in front of the modules as described later.

Those plastic scintillators have the following characteristics:

- Thickness: The thin scintillator is 0.5 mm thick and the thick one 5 cm.
- Time response: The thin scintillator has a fast time response (1.8 ns) and the thick one has a slow time response (285 ns).

This last property involves an overlapping between signals obtained when detecting a particle. Indeed, each time a particle is detected, it can trigger both scintillators meaning the slow and the fast signals are sharing a contribution. Thus, the total charge coming from the slow signal will have 2 contributions, one from the thin scintillator and another from the thick one, and the same for the charge coming from the fast signals. To summarize, we have:

- $Q_{fast,thin}$: the charge corresponding to the contribution of the thin scintillator in the fast signal.
- $Q_{fast,thick}$: the charge corresponding to the contribution of the thick scintillator in the fast signal.
- $Q_{fast,total} = Q_{fast,thin} + Q_{fast,thick}$

for the fast signal and,

- $Q_{slow,thin}$: the charge corresponding to the contribution of the thin scintillator in the slow signal.

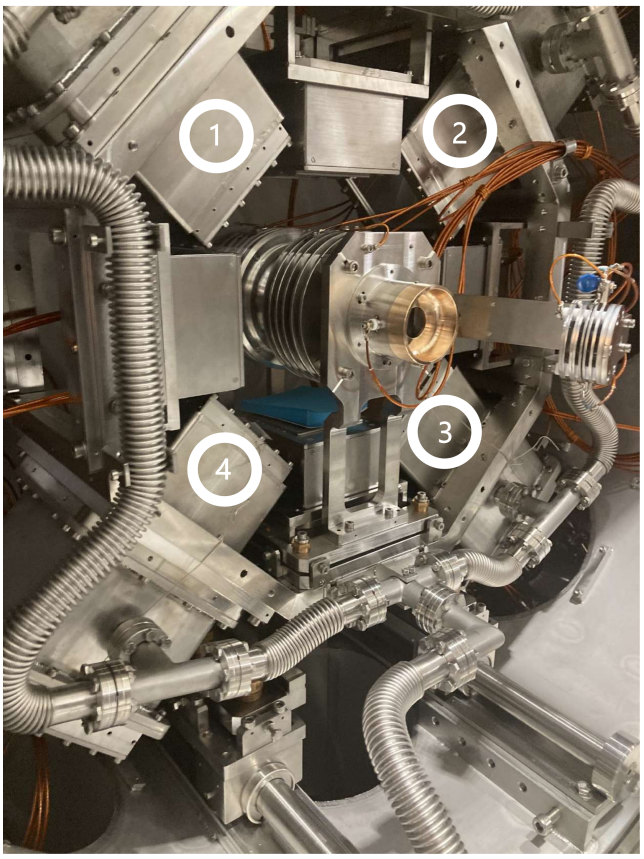

Figure 7.2 – Close-up of the MORA trap and detection system. One can notice that the phoswich detectors ($1 \longrightarrow 4$) are connected to a vacuum circuit. This secondary circuit allows a primary pump to pump directly through the detectors, improving the overall secondary vacuum of the chamber. This operation can only occur during an already existing secondary vacuum environment because of the risk of implosion of the mylar windows.

- $Q_{slow,thick}$: the charge corresponding to the contribution of the thick scintillator in the slow signal.

- $Q_{slow,total} = Q_{slow,thin} + Q_{slow,thick}$

The total charge collected for a given event is defined as:

$$Q_{tot} = Q_{fast,tot} + Q_{slow,tot} \tag{7.1}$$

This is illustrated in Fig. 7.3 and experimentally, these different contributions cannot be distinguished but they will be important for later development (see Sec. 7.3).

The data for testing the detectors were taken at LPC Caen with a prototype detector and also the detectors currently placed in the MORA chamber. The prototype is identical to the current detectors. The 4 assemblies that formed the detector are wrapped in a stainless steel case (see Fig. 7.2), reducing the outgassing from the scintillators and the photo-multipliers. In front of each scintillator, a 1.5 µm square-shaped window of mylar has been installed as well as a larger one with the same thickness in front of the 4 phoswich, closing the detector.

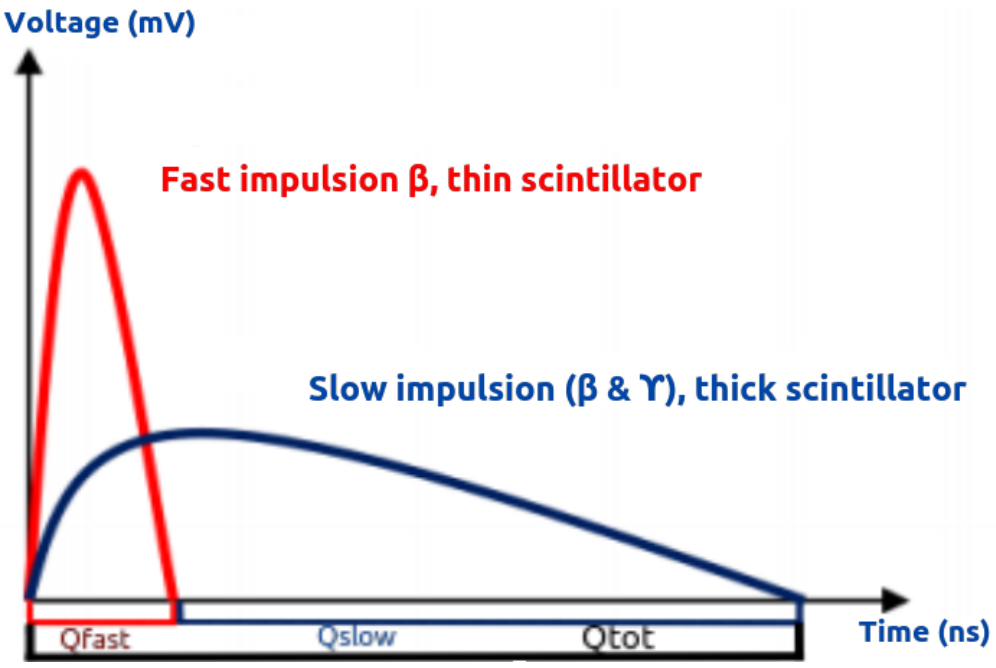

Figure 7.3 – Different signals illustrated.

For the tests at LPC Caen, the experimental setup is composed of a cylindrical vacuum chamber. The circular source was placed on an aluminum spatula with the help of vacuum-compatible tape. This spatula can be rotated from outside with the help of a scroll wheel, which can be seen in Fig. 7.4. This device allows one to place two radioactive sources(^{207}Bi,^{90}Sr) simultaneously instead of breaking the vacuum each time the source has to be changed. Hence, the phoswich detector is placed at 10 cm from the source on a stainless steel grid. The acquisition has been made with a FASTER module which can be seen alongside the power supplies rack located outside the chamber in Fig. 7.5. For each PM, three channels are created, one for each dedicated charge:

- A channel dedicated to the fast charge: Q_{fast}.
- A channel dedicated to the slow charge: Q_{slow}
- A channel dedicated to the total charge: Q_{tot}

A ^{207}Bi source was used for calibrating the detectors. A program has been created to convert the data from a FASTER file type to a ROOT file type.

7.2.1 ^{207}Bi

For the detector calibration, a source of ^{207}Bi has been used. Indeed, the ^{207}Bi decays to ^{207}Pb via electron capture. This phenomenon involves the emission of gammas and internal conversion electrons (as shown in table 7.1) making this source a good candidate for electrons-gamma discrimination.

Due to the multiple emitted conversion electrons, this source is also a good candidate for energy calibrating the phoswich detectors. Nevertheless, since the charges collected are correlated, one needs to properly process the data. The raw data, Q_{fast} vs Q_{tot}, can be seen in Fig. 7.6, where three kinds of events are shown:

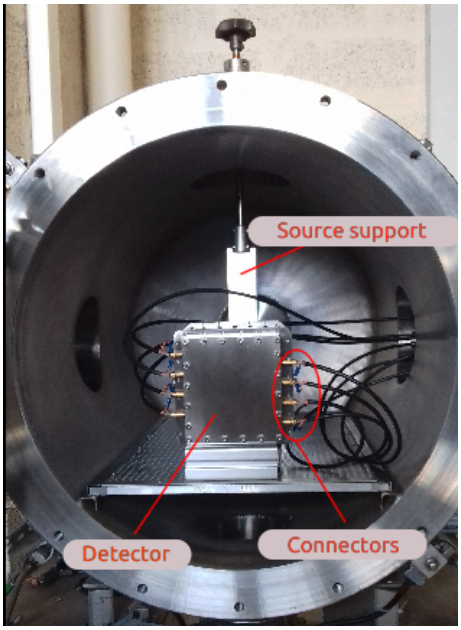

Figure 7.4 – Picture of a Phoswich detector placed inside a vacuum chamber. This detector is facing a radioactive source held to the source support with vacuum-compatible tape.

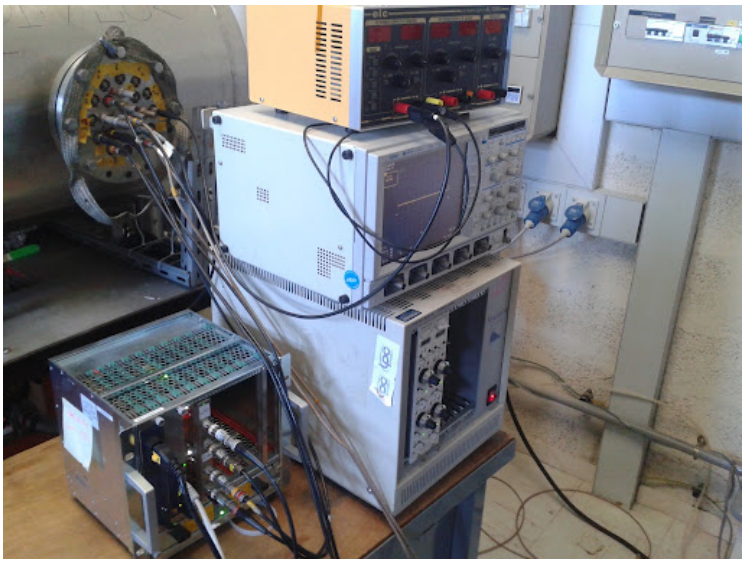

Figure 7.5 – Picture of the experimental setup used for the data acquisition of the phoswich at LPC Caen. The detector's voltages are set at 830 V by the ISEG power supply shown in the picture. The detector signals are brought to the outside with the help of the pins connector on the left of the chamber.

- The diagonal line closer to the y-axis corresponds to the electrons that are stopped in the thin scintillators.
- The diagonal line closer to the x-axis corresponds to events creating a charge only produced by the thick scintillator, *i.e* the gamma events.
- The rest of the events are either electrons or gammas, both coming from either the thin or the thick scintillators.

Electrons	*Energy (keV)*	*Intensity (%)*	*Peak number*
Auger L	7.97	54.4	N/A
Auger K	56.7	2.9	
CE K	240.10	1.88E-4	
CE L	312.24	3.2E-5	
CE M	324.25	7.5E-6	
CE K	481.6935	1.537	1
CE L	553.8372	0.442	2
CE M	565.8473	0.111	
CE K	809.77	0.00246	N/A
CE L	881.91	4.07E-4	
CE M	893.92	9.5E-5	
CE K	975.651	7.08	3
CE L	1047.765	1.84	
CE M	1059.805	0.44	
CE K	1354.20	3.55E-4	N/A
CE L	1426.34	6.13E-5	
CE M	1438.35	1.44E-5	
CE K	1682.224	0.0238	4
CE L	1754.367	0.0034	

Table 7.1 – Table containing the Auger and conversion electrons [Wan+12] from ^{207}Bi.

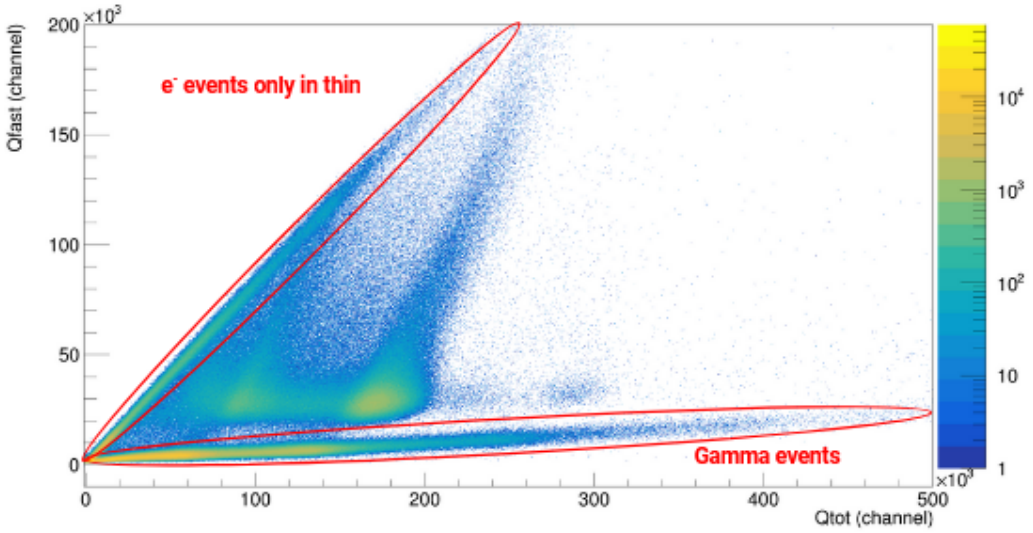

Figure 7.6 – An example of raw data of ^{207}Bi with Q_{fast} in the Y-axis and Q_{total} in the x-axis, both in channels.

Here, the typical tilting of the events reflects the correlation between the charges. This correlation has to be removed to work on the calibration process later on. Two contributions have to be removed: one impacting the total charge Q_{total} and, one impacting the $Q_{fast,total}$. Starting with the last one, one has to remove the contribution $Q_{slow,total}$ of the thick scintillator when a fast signal has been triggered. That is why, the $Q_{fast,total}$ charge becomes:

$$Q_{fast,total} = a \times Q_{total} + b \tag{7.2}$$

$$Q_{fast,total} = a \times (Q_{fast,total} + Q_{slow,total}) + b \tag{7.3}$$

$$Q_{fast,total}(1 - a) = a \times Q_{slow,total} + b \tag{7.4}$$

$$Q_{fast,total}(1 - a) - a \times Q_{slow,total} = b = Q_{fast,total}^{Corrected} \tag{7.5}$$

with a the slope of the gamma line. This correction will make the gamma line horizontal. Q_{total} also has to be de-correlated from the $Q_{fast,total}$ dependency. By removing a contribution, of $Q_{fast,total}$ in Q_{total} such as:

$$Q_{total}^{Corrected} = Q_{total} - A \times Q_{fast,total} \tag{7.6}$$

with A, the slope of the tilted events. The spectrum, corrected from correlations, can be seen in Fig. 7.7. Here the A constant is retrieved directly on the tilted spectrum (see Fig. 7.6). By taking several points which belong to the same peak, we can deduce the slope of the spot and thus A.

Cuts can be performed on the spectrum to make it easier to handle. This way, we get rid of the gamma line and also the electrons stopped in the thin scintillator. That is why the gammas and the electrons that are only detected in the thin scintillator are removed[1]. Once corrected, the 2D-histogram can be projected on the x-axis. The calibration is done using 3 energies: the peak at 481.69 keV, the one around 1 MeV and the one at 1691.24 keV (see Table 7.1). The last two are defined, due to the experimental resolution, by a weighted average using the most branching ratios of the most intense conversion electron lines contributing to it. This gives, for the 1 MeV peak for example:

$$< E_{peak} >= \frac{\sum_n E_n \times w_n}{\sum_n w_n} = \frac{975.651 \times 7.08 + 1047.765 \times 1.841 + 1059.805 \times 0.44}{7.08 + 1.84 + 0.44} = 993.78\,\text{keV} \tag{7.7}$$

The energy of the peak around 560 keV is also calculated this way, but since this peak does not contribute to the calibration process, even though it has been taken into account in the

[1]The electrons that have been removed are technically good events. However, these events are removed to obtain a much simpler spectrum for the calibration.

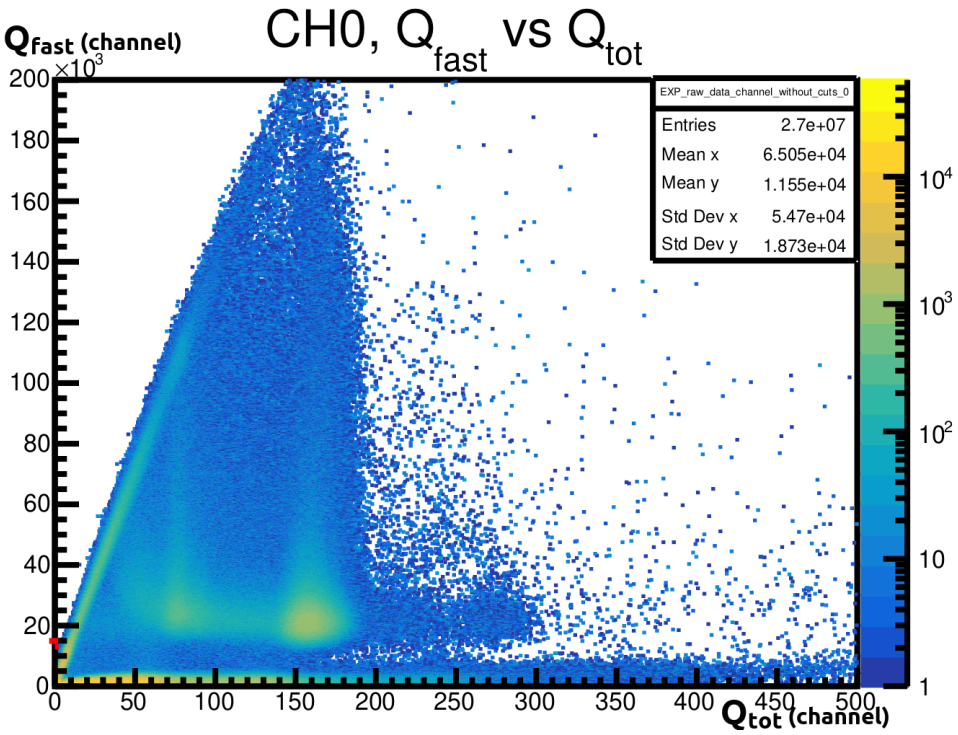

Figure 7.7 – An example of corrected data of ^{207}Bi with $Q^C_{fast,total}$ on the Y-axis and Q^C_{total} on the x-axis, both in channels.

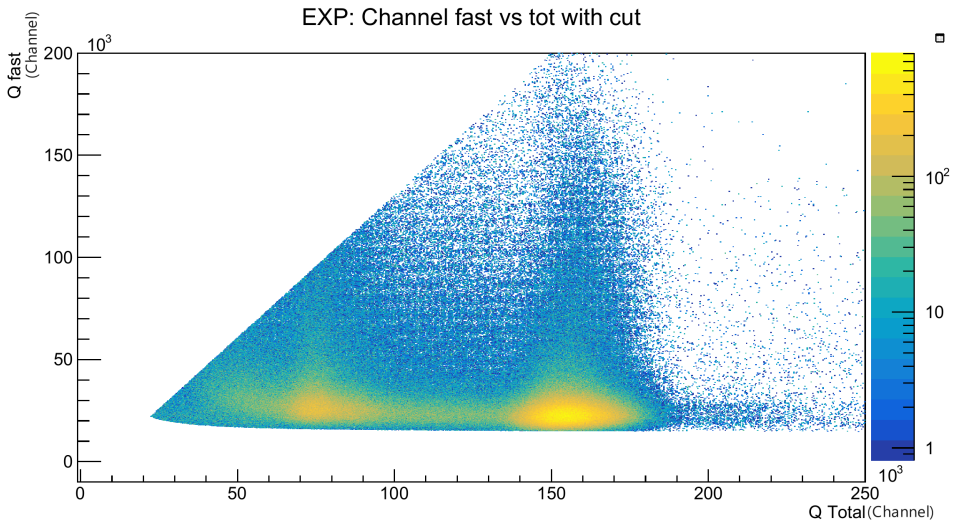

Figure 7.8 – An example of the spectrum after the cuts performed on the electons and the gamma line.

expression of the fit, it is not shown in Table. 7.2. Then, by fitting the peaks with Gaussian functions, one can have access to the mean values needed for the energy calibration. By creating a direct correspondence between the charge and the theoretical energies, a function can fit the resulting histogram by giving the calibration parameters: the slope α, and the offset value β. The data are then converted from channel to energy (see Fig. 7.9) and by fitting the peaks, the mean values are recovered and stored in table. 7.2.

The calibration has been done but in order to improve it, simulations were performed

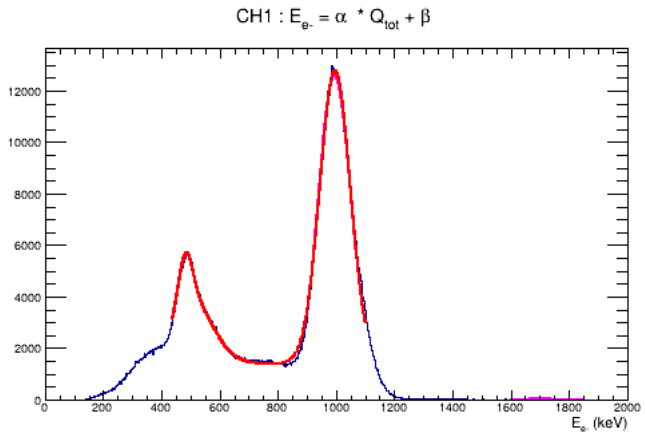

Figure 7.9 – Example of the 1D histogram fitted with 3 Gaussian functions for the three major bigger peaks. The third peak at 1.6 keV is fitted separately.

	Energy 1 (keV)	***Energy 2 (keV)***	***Energy 3 (keV)***
Channel 1	482.22 ± 0.68	994.69 ± 0.10	1697.4 ± 2.4
Channel 2	481.82 ± 0.59	994.72 ± 0.11	1689.3 ± 2.6
Channel 3	482.07 ± 0.39	994.649 ± 0.079	1689.3 ± 1.9
Channel 4	481.86 ± 0.81	994.693 ± 0.092	1689.3 ± 2.9
Expected values	***481.69***	***993.78***	***1691.24***
	Peak resolution 1	***Peak resolution 2***	***Peak resolution 3***
Channel 1	12.19% ± 0.39%	13.809% ± 0.035%	11.38% ± 0.38%
Channel 2	14.95% ± 0.24%	13.464% ± 0.046%	11.49% ± 0.44%
Channel 3	14.95 ± 0.24	13.044 ± 0.025%	10.37% ± 0.31%
Channel 4	14.95% ± 0.24%	14.306% ± 0.031%	11.96% ± 0.43%

Table 7.2 – Table containing the values from the fit of the experimental peaks and also the expected values. The other part of the table shows the resolution of each fitted peak. It is calculated as $R = \frac{FWHM}{Energy} \times 100$.

on GEANT4. The result of this work will be presented in the following section.

7.3 GEANT4 calibration

7.3.1 Simulated offline sources with GEANT4

Originally, this study aimed to improve the former calibration study. For this, the use of the GEANT4 [Ago+03] software has been chosen. This toolkit is mainly used within particle and nuclear physics. This software simulates the trajectories and interactions of the particles by using Monte-Carlo methods. The first step of this study was to recreate the experimental setup used for the data acquisition done at the laboratory. The source itself was set as a point source for simplicity. The simulated source, as the experimental one, is placed on a support at 10 cm from the center of the detector. This source support contributes a lot to the total spectrum as shown in Fig. 7.10.

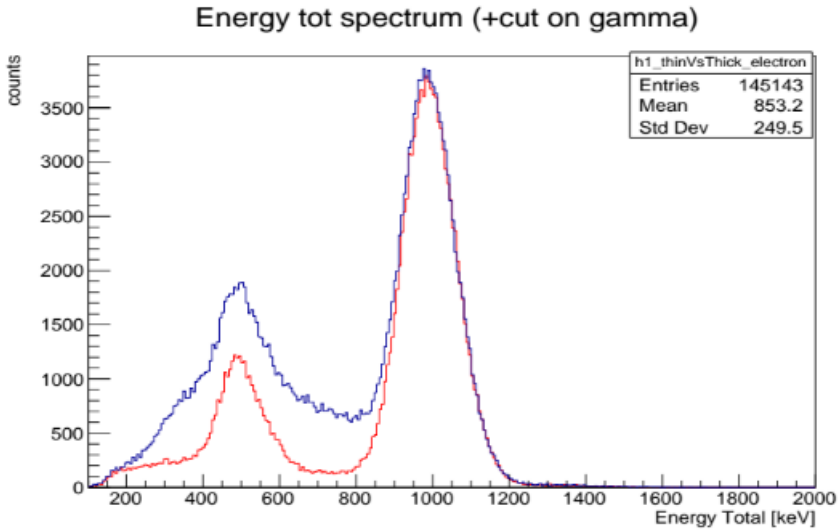

Figure 7.10 – Comparison between both simulated spectra. The red spectrum reproduces the complete simulation except the source support while the blue spectrum regroups all the features of the simulation.

Each simulated PM can be accessed independently and is filled with three different data sets. All these counts are stored in the form of a ROOT tree:

- The primary events: this stores the primary vertex for each event in the run. It typically stores the energy and type of each particle, as well as the initial vertex position in x, y, and z. Here at (0,0,0) for the source.
- The detector events: This stores the information concerning the Phoswich hits for each event. It can be separated into two different parts:
  - Phoswich level information: the information is merged at the phoswich level. In an event where 2 particles hit the same phoswich, the energy will be the sum of the 2 deposits. Hence, this level of information is closer to what can be measured in data taking.
  - Track level information: this part stores the information at the track level. This allows individual particle reconstruction. E.g. a particle crossing two phoswiches

will induce two tracks inside the root tree, with the summary of the deposit for each phoswich and the same trackID for both tracks. The trackID refers to its definition in GEANT4 and it represents a unique identifier allocated to each particle in an event. Another example: 2 particles interacting in the same phoswich will generate 2 different tracks (even if they are both gammas, as soon as they are not the same particle, they will be separated).

The simulated data give the exact energy of the peaks as shown in Fig. 7.11a. The first step is, thus, to add some artificial resolution or smearing to this data. Indeed, the generation of light in the plastic scintillators and the conversion in signal by the PMT are not implemented in the code. The smearing parameter is proportional to the square root of the energy and is applied on both axes. Since the gamma line is at $E_{fast} = 0$, these events are not smeared. The cuts on gamma and back-scattered electrons are applied either on the experimental or simulated spectra after the smearing. Then, the next step is the projection of the spectra on the x-axis in order to compare them. This test has two purposes:

- To check the smearing of the simulated spectrum.
- To check the calibration of the experimental spectrum.

A χ^2/NdF test is done for each value of calibration, using 50 different smearing values[2]. This results in the best agreement between the experimental and simulated spectra. Even though the best agreement was found, an amplitude difference can be seen in Fig. 7.12 at the 481.69 keV peak.

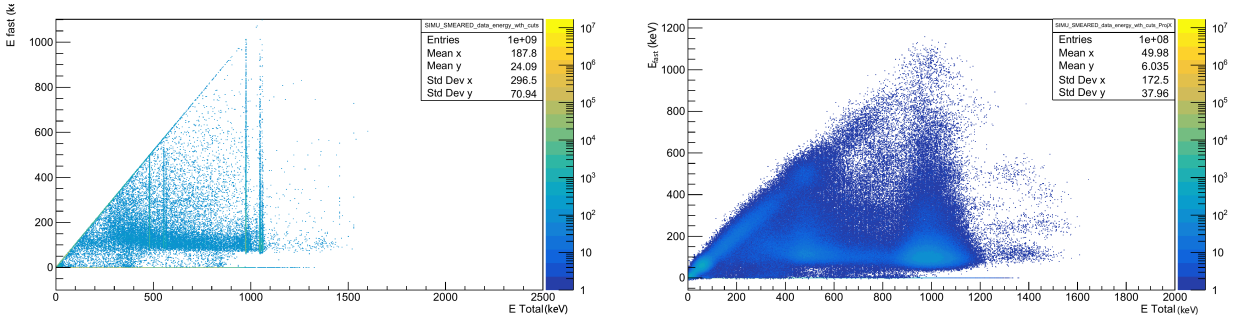

(a) (b)

Figure 7.11 – Transformation of the simulated spectrum before (a) and after the smearing factor applied (b).

Even between experimental spectra, differences can be seen, especially on the "valley" between the two peaks. One can also notice that the behaviour of two photo-multipliers is reacting the same way, the PM 1 with the PM 2 and the PM 0 with the PM 4. A comparison PM by PM has been done in Fig. 7.13. However, the main issue is the difference in amplitude which is still unknown to us, it has been investigated in the following study.

[2]These values are set between arbitrary minimum and maximum. From the minimum, a stepper explores the 50 different values.

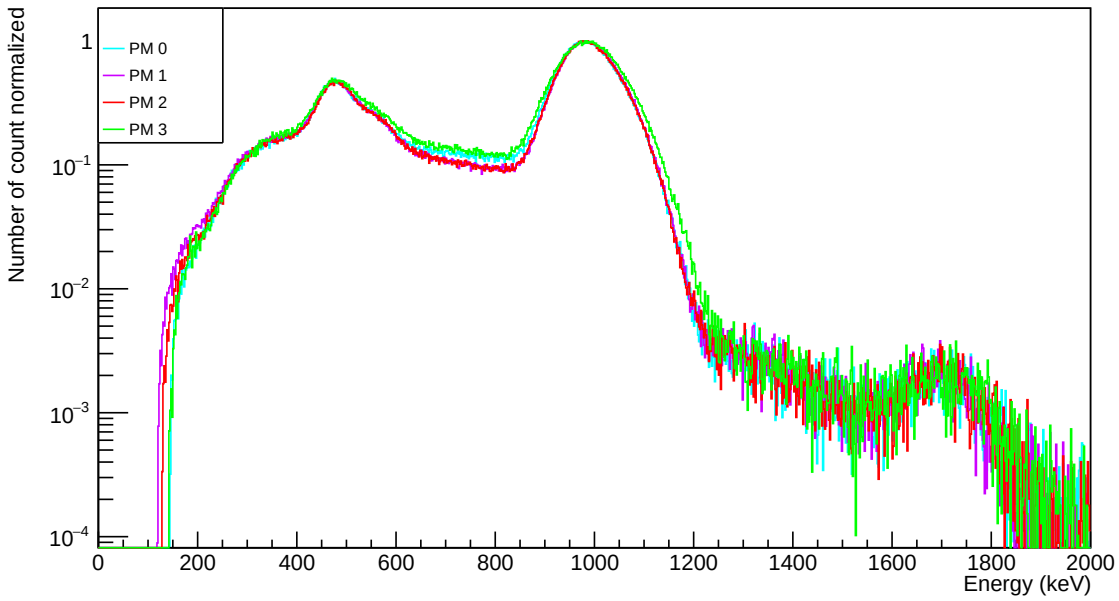

Figure 7.12 – Comparison between experimental spectra. All spectra have been normalized according to the 1 MeV peak amplitude.

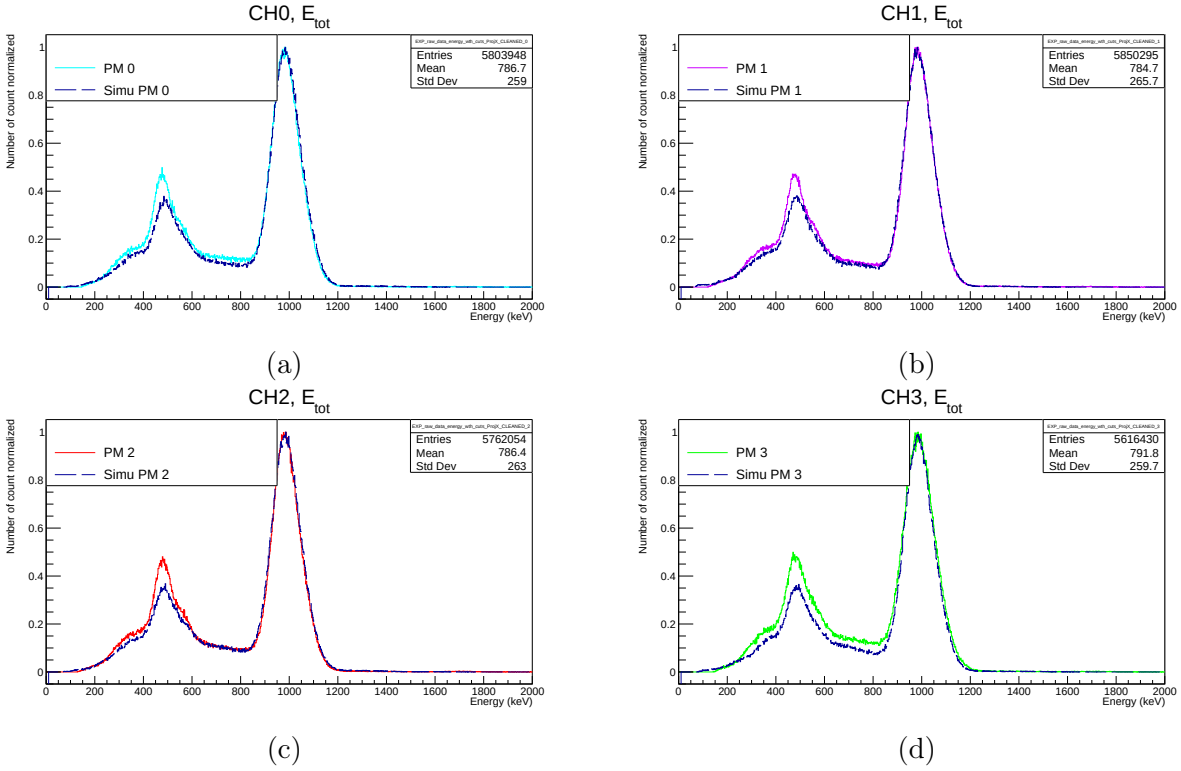

Figure 7.13 – Comparison between experimental and simulated (in blue) spectra with GEANT4.

7.4 Study of the amplitude difference

The difference between the experimental and simulated spectra has been investigated in many ways, as presented in the following section.

7.4.1 Branching ratio

One of the leads to explore is that this difference in amplitude is due to a non-realistic branching ratio in the simulation. This comparison has been done of the primary spectra on the simulated data (GEANT4 and NUCLEIDE++). NUCLEIDE++[Thi+20] is a file generated by the LHNB, which was taken as a source for generating the events. This particular file and method will be called "NUCLEIDE++" in the following of this work.

If the intensities of the energy levels are not correct regarding to the latest database published, here on the NNDC website [Wikd], the ratio between the primary low energy peak (at 481.69 keV) and the high energy one (at 975.65 keV) should be different as well. The comparison of both ratios is tabulated in Table 7.3.

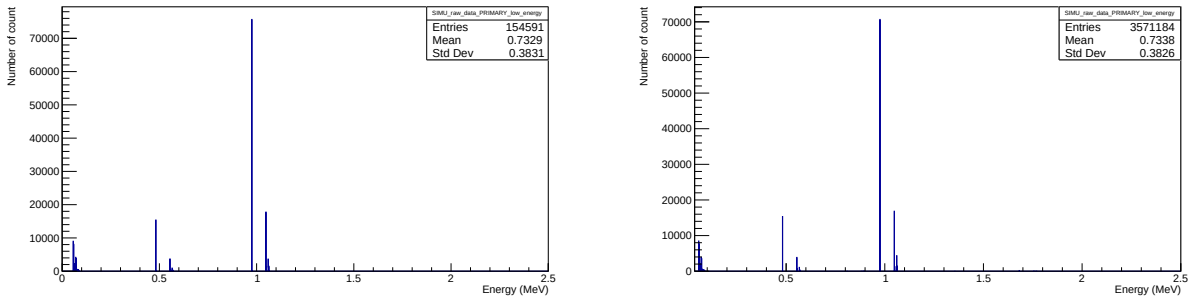

(a) GEANT4 primary spectrum.

(b) NUCLEIDE++ primary spectrum.

Figure 7.14 – Different amplitudes on the primary spectra of the different data sets. One can notice the difference in amplitude on the peak at 975 keV.

File	*Branching ratio*
GEANT4	0.2036
NUCLEIDE++	0.2169
NNDC	0.2170

Table 7.3 – The ratio between two peaks on the NUCLEIDE++ file is 99.95% similar to the NNDC ratio while the GEANT4 one is just 93.82%.

According to Fig. 7.14 and Table 7.3, the difference between the GEANT4 ratio and the NNDC one is 6.18% but the multiplicative factor needed for the low energy peak to reach the experimental one is around 15%. This shows the fact that the lead of the branching ratio could explain partially the difference in amplitude, but other factors have to be investigated as well.

7.4.2 Smearing factor

To reproduce the experimental data, the simulated data have to be smeared. The smearing factor has a huge impact on the data: if it is too large it will completely spread the data over the entire histogram and if it is too small it will still present some inner structure of the peak which is supposed to be merged experimentally. This smearing is applied the same

way on each charge and one way to reproduce the experimental data is to play with the Q_{fast} contribution. Furthermore, as shown later, the closer to zero this factor, the better the discrimination between the gammas and the peaks. This is true to some extent, since the closer this factor is to zero, the worse the data reproduction. That is why the lower limit on this smearing factor is set to 0.35, an arbitrary value, cycling through the following values: 0.35, 0.50, 0.75 and 1.0. Here, only the 0.35 and the 1.0 figures are shown to illustrate.

It is also important to mention that, for the following study, another way to display the data has been chosen: Instead of plotting the data shown in Fig. 7.7, hence Q_{fast} vs Q_{tot}, the y-axis becomes Q_{fast}/Q_{tot} meanwhile the x-axis remains unchanged. This new paradigm allows us to have a better visualisation of the events and a correspondence in y between non-calibrated spectra and calibrated ones. Furthermore, this way of processing the data allows a smearing of the gamma line which was not present with former plots. One can notice in Fig. 7.15 an accumulation of events on the right of the peak around 1 MeV. This phenomenon is induced by the smearing factor. Therefore, for the following tests, a smearing factor of 0.75 is set on Q_{fast} events in order to get a better discrimination between gammas and electrons[3].

[3]The dedicated figures can be seen in the Annex part. Here just the most extreme values are presented to see the real difference between simulated spectra.

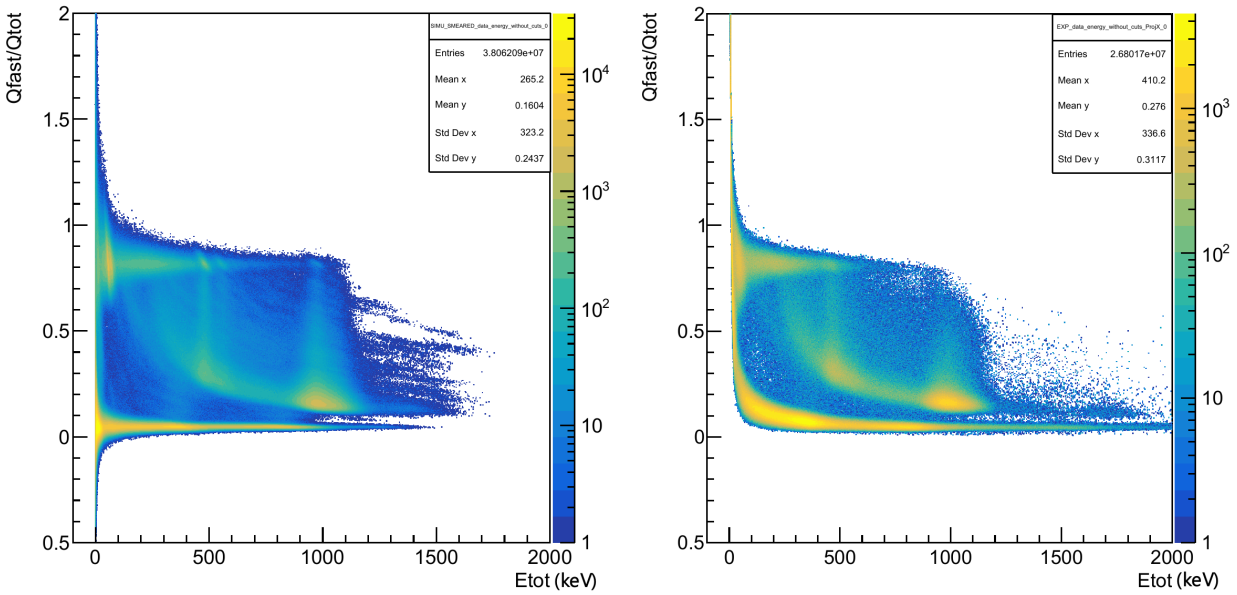

(a) On the left: The simulation with a 0.35 smearing factor. The gamma and the rest of the spectrum are very well separated, however, the general structure shape of the histogram contains events that are highly impacted by this smearing factor leading to a separation between the energy of the peak at low energy.
On the right: the experimental spectrum.

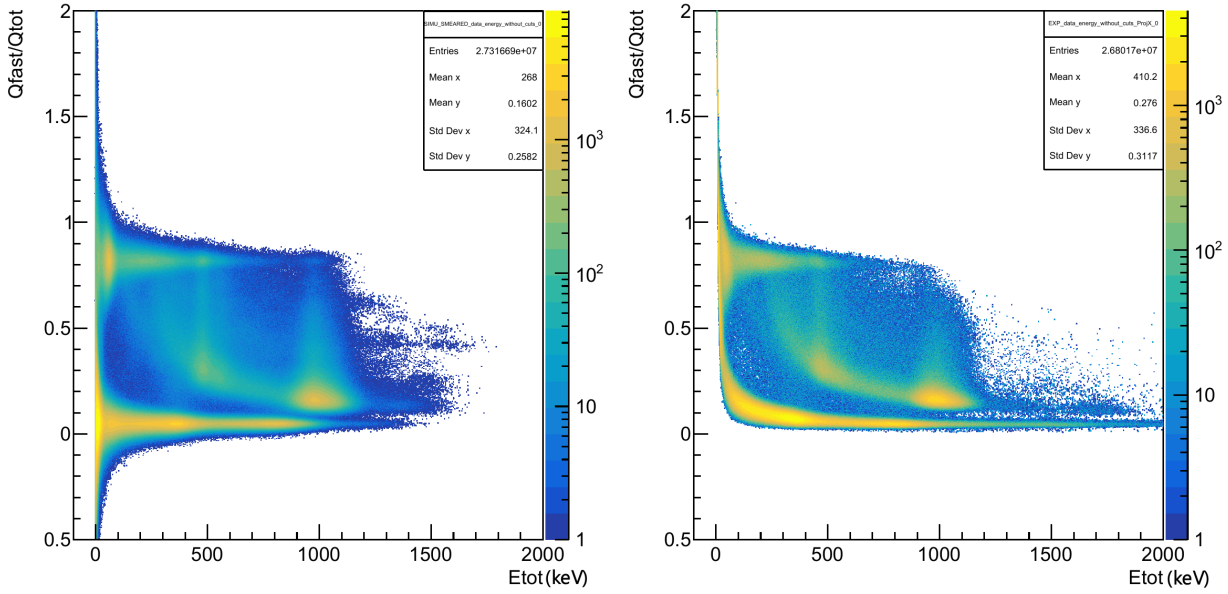

(b) On the left: The simulation with a 1.0 smearing factor which is the default smearing.
On the right: the experimental spectrum.

Figure 7.15 – Study of the impact of the smearing of the thin scintillator on the simulated spectra.

7.4.3 Thickness of the thin scintillator

Knowing that the thin scintillator is 0.5 mm thick according to the manufacturer does not mean it is actually the case. The typical uncertainty on the thickness is about 0.03 mm, however, for the sake of curiosity, several thicknesses have been tested, from 0.30 mm to 0.53 mm.

7.4.3.1 0.30 mm

This value is obviously way thin regarding the supposed thickness of the scintillator but it has nevertheless been simulated to see how intense the effect is on the 2D histogram (see Fig. 7.16a) and, of course, on the final 1D spectrum.

On Fig. 7.17, the agreement between the peaks of the simulated spectrum (in dark green) and the experimental one (here in light blue) fits correctly (ratio equal to 1).Probabliy due to its low intensity, the high energy peak (1691 keV) is not reproduced by GEANT4 explaining the difference at this point on the spectrum. Nonetheless, the low energy part and the valley between the two peaks are not correctly reproduced. Moreover, besides the fact that the peaks are well reproduced, the way the cut has been done theoretically induces that more events should be in the peak around 1 MeV which means, according to the normalization, lowering the peak at low energy. Thus, even though the match seems good on this plot, with an appropriate cut the peak at low energy should be slightly under the experimental spectrum.

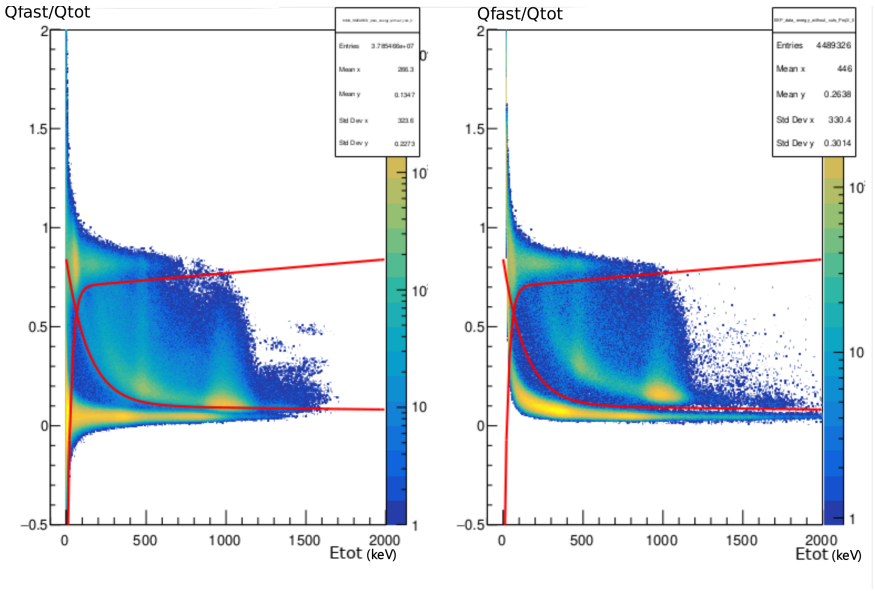

(a) On the left: 2D histogram of the simulated data with a thickness for 0.30 mm on the thin scintillator.
On the right: The experimental spectrum. The cuts are seen as the red lines on both plots. They have obviously been adapted to the new way to plot the data. However, the "philosophy" of it remains since the gamma line and the back-scattered electrons are removed.

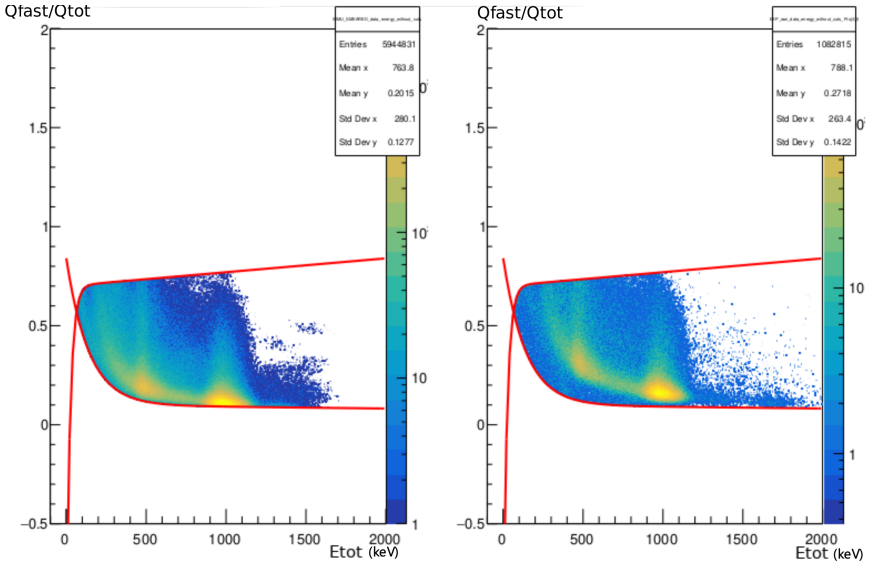

(b) On the left: 2D histogram of the simulated data with a thickness of 0.30 mm for the thin scintillator after cuts.
On the right: The experimental spectrum after cuts.

Figure 7.16 – Comparison before and after applying the same cuts between simulated data with a thickness of 0.30 mm on the thin scintillator and the experimental spectrum.

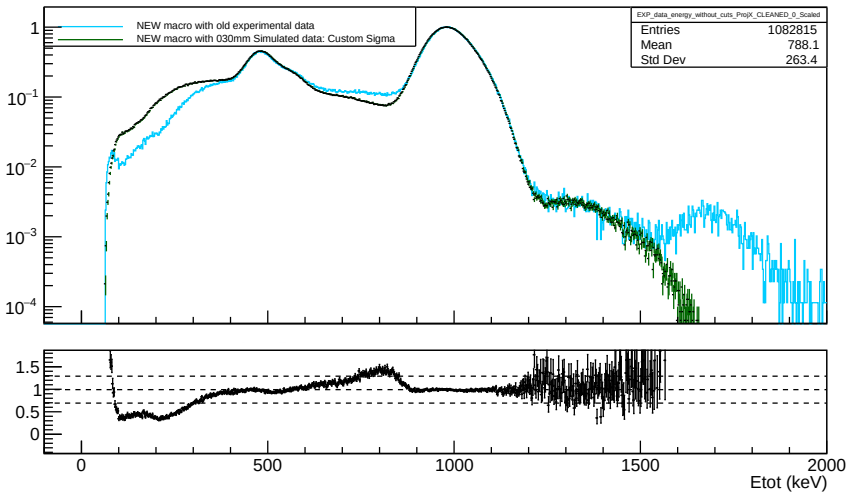

Figure 7.17 – This figure represents two 1D spectra on the first plot for a thickness of the thin scintillator of 0.30 mm. The second plot, shows the ratio between the two 1D spectra. On this figure and on all figure produced by the GEANT4 event generator, the peak at 1.68 keV is not reproduced.

7.4.3.2 0.40 mm

This thickness has been probed with two different methods. The same as for the other thickness, *i.e* by using the default way to generate events with GEANT4 but also with NUCLEIDE++.

7.4.3.2.1 GEANT4

Here the same study as for the 0.30 mm above (see Fig. 7.16), has been done. The resulting 2D-plots can be seen below in Fig. 7.18 and projecting those plots on the x-axis gives Fig. 7.19.

One can still notice, in Fig. 7.19, that the valley between the two peaks is still not correctly reproduced. However, the low energy part at the left of the peak @ 481.86 keV has a better agreement than the previous spectrum. The 0.40 mm thickness brings slightly more differences, compared to the 0.30 mm, in the agreements between the peaks according to the ratio graph beneath the figures. This difference still remains negligible the ratio between spectra being close to 1 in this region. However, a better agreement is observed in the low-energy part.

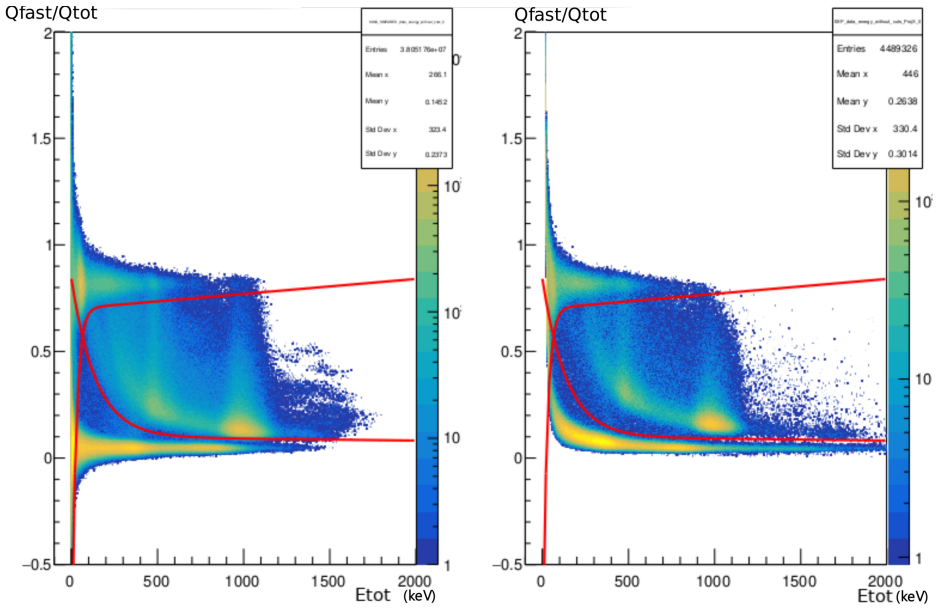

(a) On the left: 2D histogram of the simulated data with a thickness of 0.40 mm for the thin scintillator.
On the right: the experimental spectrum with the usual cuts seen as the red lines on both plots.

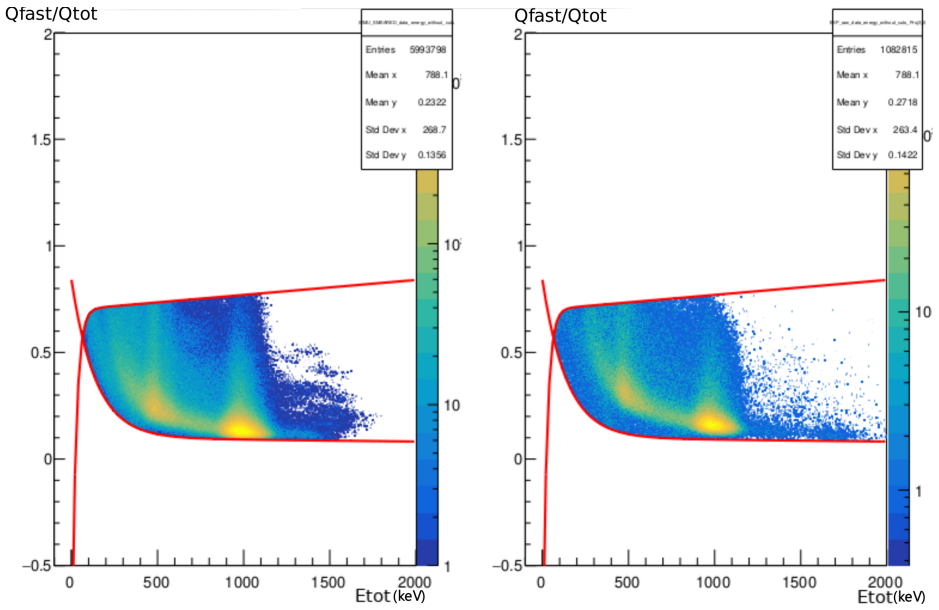

(b) On the left: 2D histogram of the simulated data with a thickness of 0.40 mm for the thin scintillator after cuts.
On the right: the experimental spectrum after cuts.

Figure 7.18 – Comparison before and after application of the same cuts between simulated data with a thickness of 0.40 mm on the thin scintillator and the experimental spectrum.

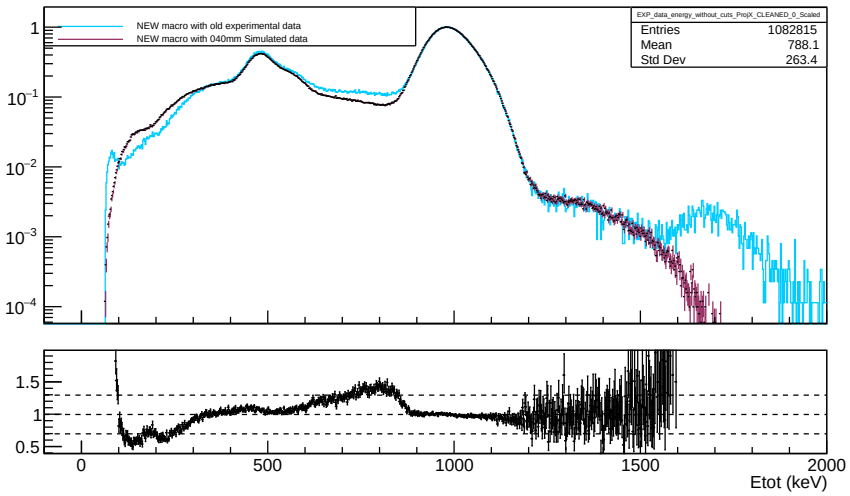

Figure 7.19 – On this figure, the agreement between the simulated spectrum (in dark brown) and the experimental one (here in light blue) is slightly worse than the previous one, especially on the low energy peak.

7.4.3.2.2 NUCLEIDE++

Two different cuts will be tested on the NUCLEIDE++ file because of the nice agreement between the spectra. The first one, defined as the "same cuts" is identical to the one applied on the experimental spectrum. The "different cut", however, has been adjusted to not cut any events on the main peaks.

NUCLEIDE++ with the same cuts as the GEANT4 study:

This file has been used as a generating event as described earlier. It was provided by the Laboratoire National Henry Becquerel (LNHB). This file has been generated using the specificity of the NUCLEIDE++ tool kit [Thi+20], and will not be explained here. The resulting 2D histograms are in Annex (see Fig. 9.3) where a reproduction of the peak at 1.68 keV can be seen. In Fig. 7.20 and Fig. 7.21, we can see that the peak at 1691 keV is reproduced contrary to the GEANT4 simulation. The low energy part, however, is still badly reproduced in a way similar to the GEANT4 simulations.

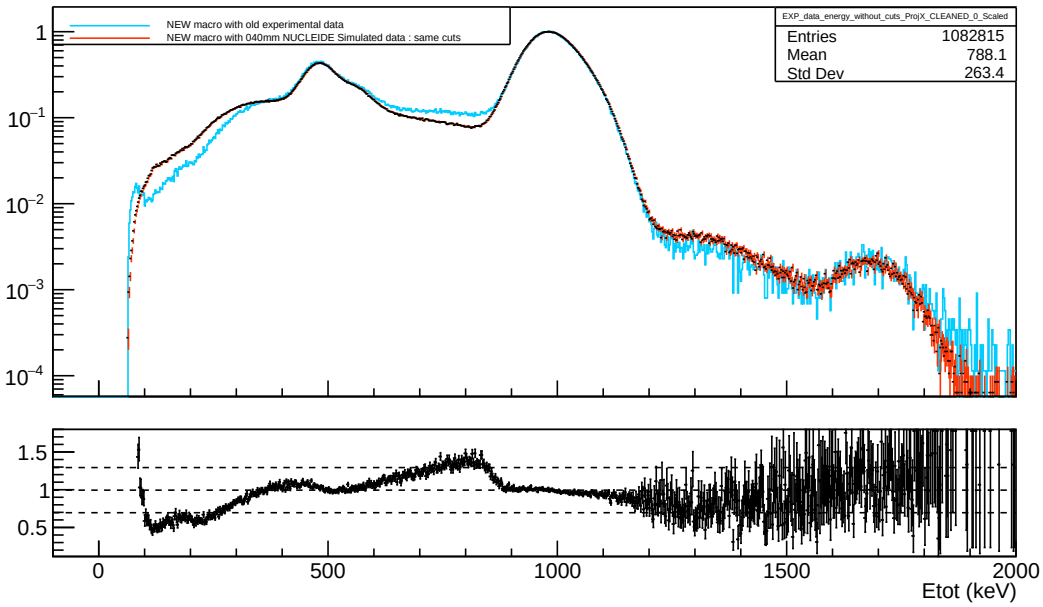

Figure 7.20 – Comparison between the projection of the experimental data in light blue and the projection of the simulated data (NUCLEIDE++) for 0.40 mm with the same cuts between the experimental and simulated data.

NUCLEIDE++ with the different cuts:

The same study has been done with better cuts on the simulated spectrum. These cuts can be seen in Fig. 9.4. The comparison between those two spectra in presented in Fig. 7.21.

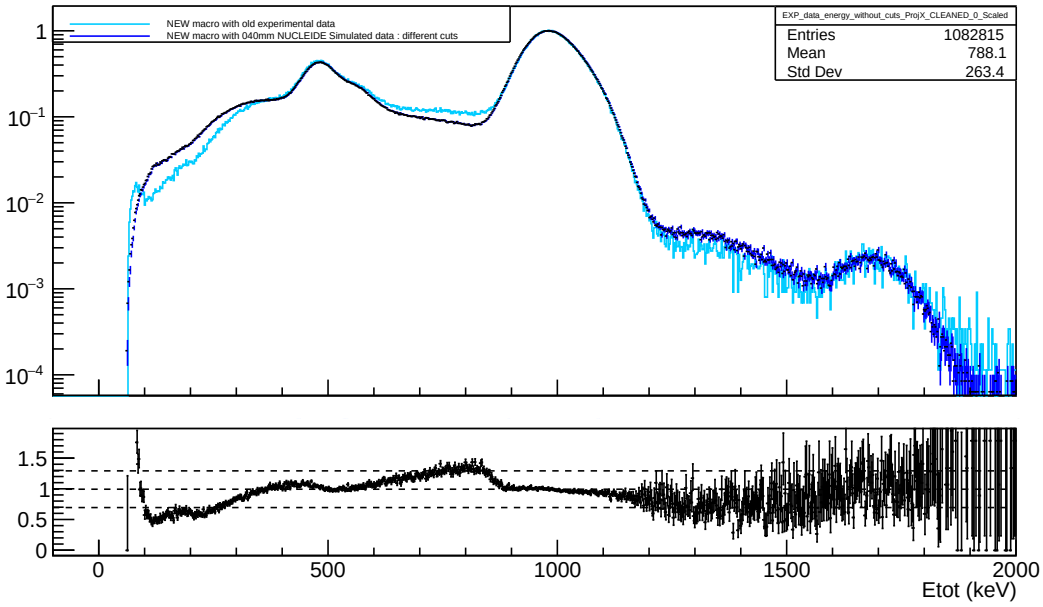

Figure 7.21 – Comparison between the projection of the experimental data in light blue and the simulated data (NUCLEIDE++) in light brown for 0.40 mm with the more adapted cuts.

Study on the cuts impact:

An overlap of the spectra has been done in order to see more closely the impact of the kind of cuts applied on the 2D plots.

According to Fig. 7.22, the difference in counts between the two simulated spectra is

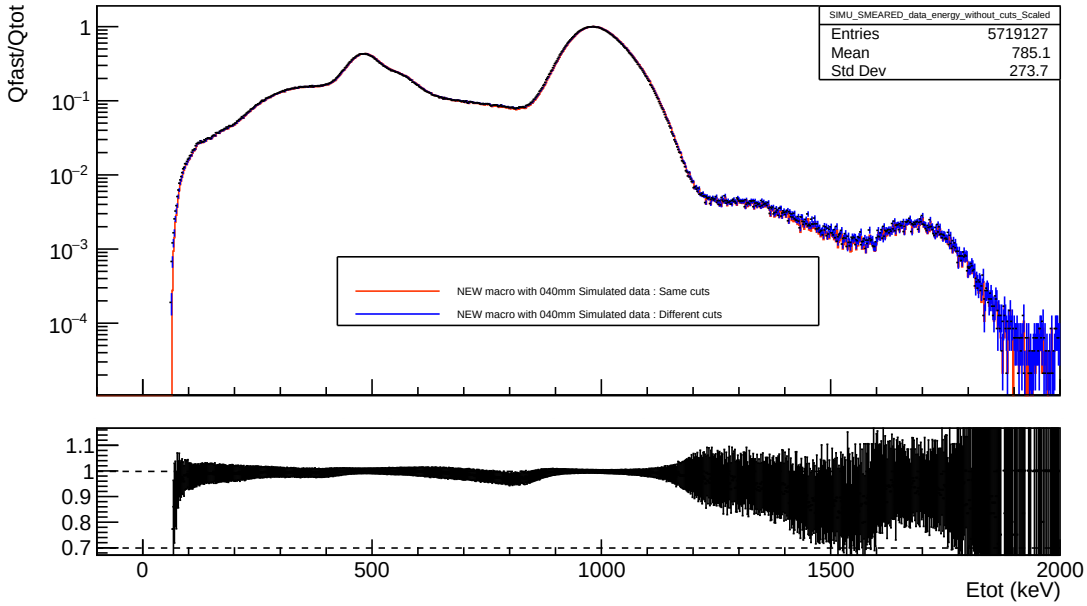

Figure 7.22 – Comparison of the two simulated 1D histograms. The colours have been changed to help distinguish the spectra.

negligible. This conclusion can, to some extent, be applied to the other tested thicknesses, meaning that even if the cuts are going through the events the projection on the x-axis will not be strongly impacted.

7.4.3.2.3 Different materials

The final possible explanation for the difference in amplitude that has been explored was to study the thickness of specific materials such as Mylar sheets and the source support. These tests have been done with a beam of 1 MeV of kinetic energy in order to see the effect of the high-energy peak on the amplitude of the low-energy peak. This test has been done with a thin scintillator of 0.50 mm as by default and with:

- Mylar: the default thickness of 1.5 µm and the thickness of 2.5 µm (see Fig. 7.23) have been tested.
- Source support: the default thickness of 3 mm and the thickness of 1 mm have been tested (see Fig. 7.24).

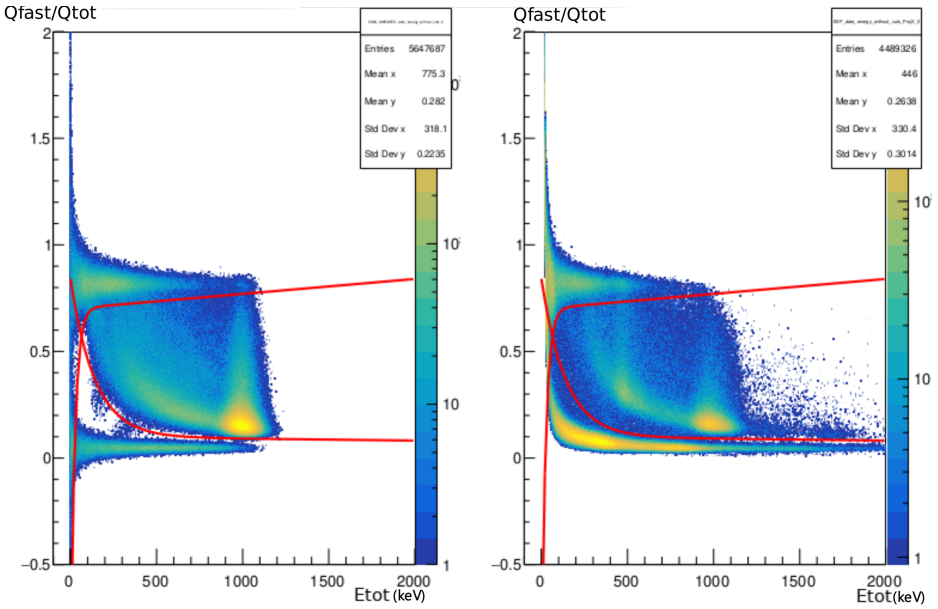

(a) Comparison of the simulated data on the left and the experimental data on the right. The red lines are the cuts that will be applied.

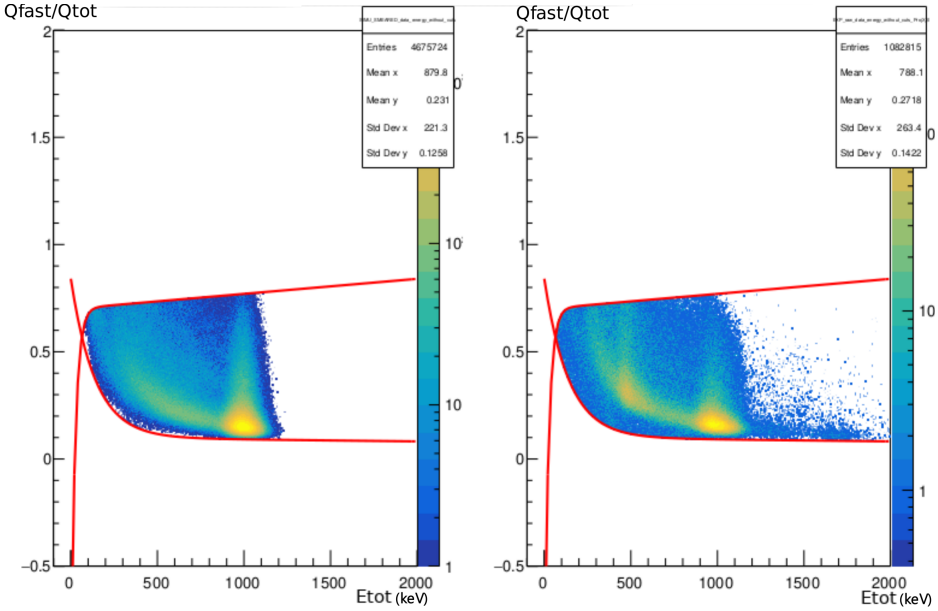

(b) Comparison of the simulated data on the left and the experimental data on the right after the cuts have been applied.

Figure 7.23 – The simulated figures (left panel on both) have been created using of 2.5 µm of Mylar and a thick source support of 1 mm of aluminum.

To conclude this study, the thickness of the mylar or the source support does not impact the overall spectra. Concerning the thickness of the mylar sheets, it is small meaning that even though it has been increased for the test, it remained small regarding relativistic electrons. However, changing the materials of the source support has a huge impact on the spectrum. For example, passing from aluminium to stainless steel makes a huge difference, as shown in Fig. 7.25 but unfortunately it has been verified later that the source support is

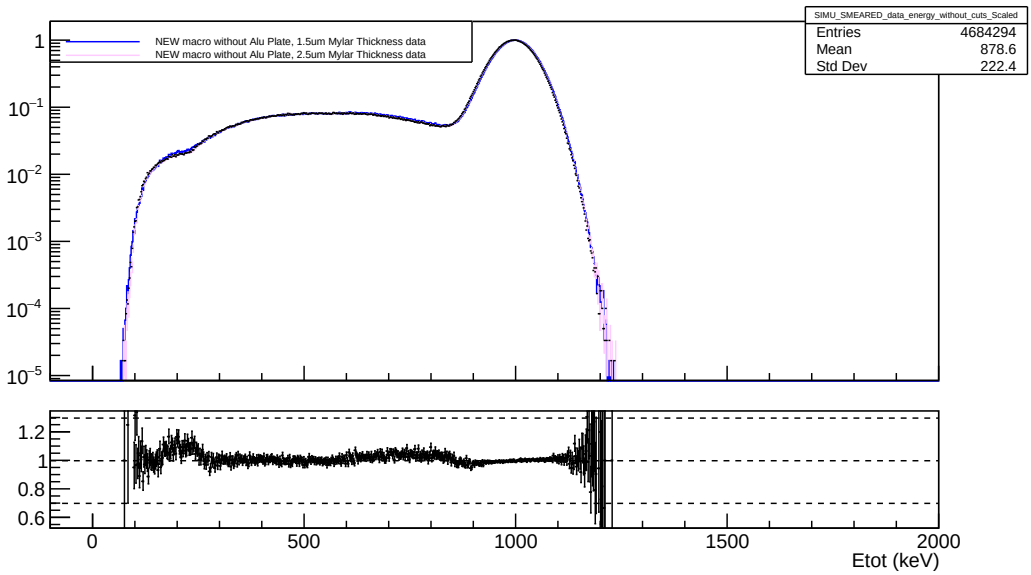

(a) Comparison of the effect of the mylar thickness with respect to the thickness of the source support. Here the source support is 1 mm.

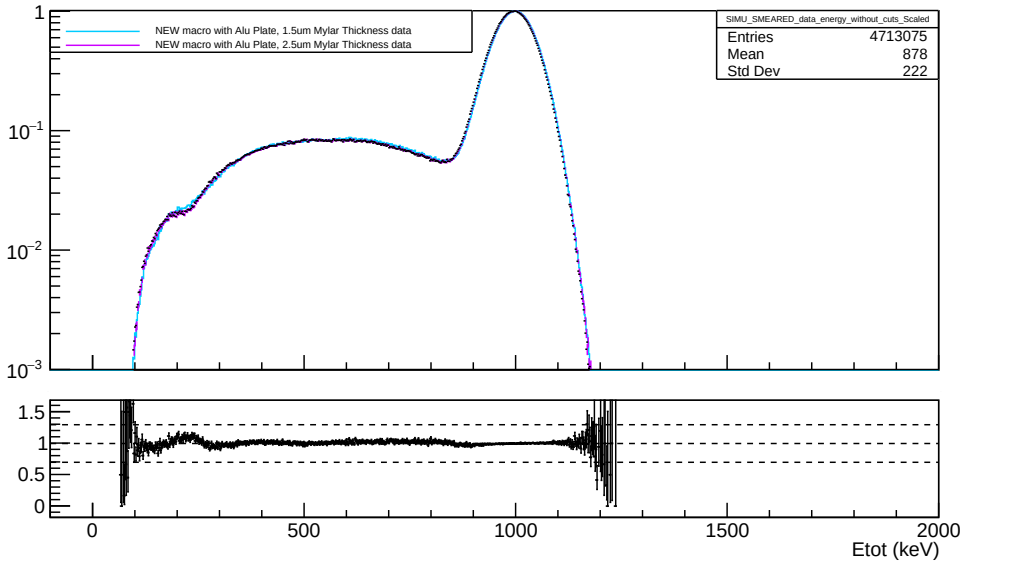

(b) Comparison of the effect of the mylar thickness with respect to the thickness of the source support. Here the source support is 3 mm.

Figure 7.24 – Comparison of the impact of the mylar thickness.

made of aluminium.

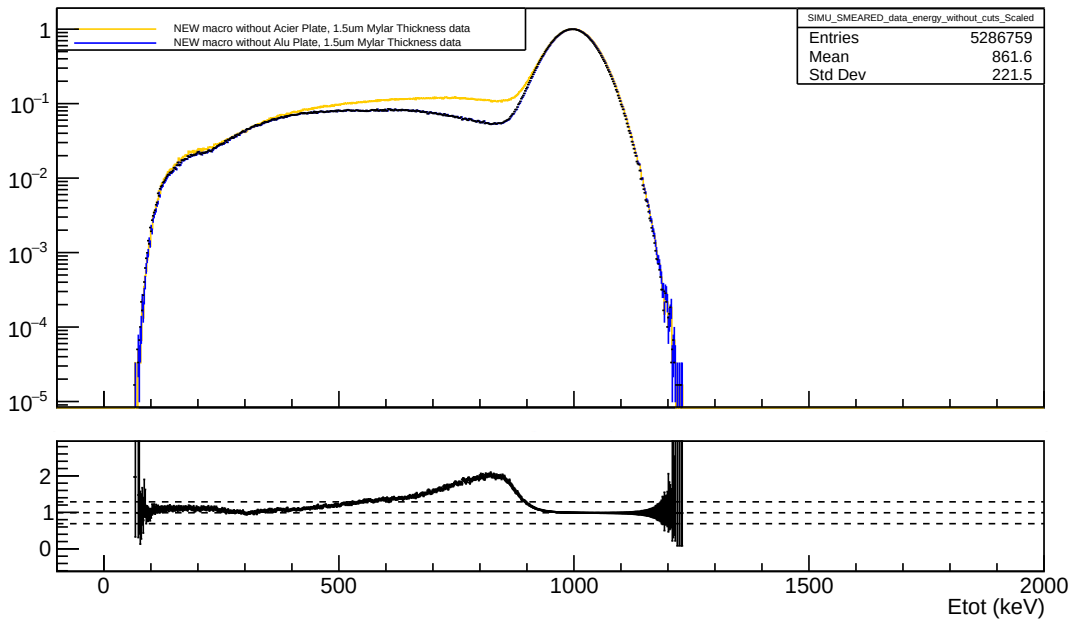

Figure 7.25 – Comparison between 2 materials (Al in blue and steel in yellow) used for the source support simulated with GEANT4.

7.5 Conclusion:

This chapter aimed to present in deep detail the study of phoswich detectors. The process of calibration of those detectors is not straightforward contrary to usual ones. Here the collected charges are correlated and one must solve this problem way before starting to calibrate the detectors. A first calibration has been done with the help of a circular ^{207}Bi. This source provides both electrons and gamma particles leading to a good discrimination between those particles, knowing that we could remove the gammas from the non-calibrated spectra. For the calibration, back-scattered electrons and electrons detected only by the thin scintillator are also removed even though they are valuable events. Hence that way, spectra are simpler to handle. Once the charges are de-correlated, the channel spectra are projected on the x-axis and the main peaks are fitted with Gaussian functions to access the mean position of each peak. A correspondence is made between the channel and the energy as a linear function which is a reasonable assumption.

To ensure the fidelity of the calibration, GEANT4 simulations were performed, recreating the experimental set-up. Since the simulated spectra are exact in terms of energy, it was needed to degrade them to fit the experimental resolution. A strong difference between the simulated and experimental spectra was observed and investigated in this chapter. We have probed the smearing factor, the thickness and the materials used in several parts of the simulations and, unfortunately, the origin of the issue is not fully understood. The final results are, however, shown in Fig. 7.26. This can be frustrating for the reader but it is certainly worse for the writer. However, several ways to improve these results can be thought of:

- For now, the calibration has been done in a very simple set-up, even though the differ-

ence of amplitude exists and remains unknown the calibration algorithm works making the calibration only possible with old data and simulations that are not representative of the actual experimental set-up. We have contributed to build the simulation that mimics the current experimental environment with all the detectors (RIDE, phoswich and Si detectors) placed near the trap which is also simulated (only the geometry and not the RF field). The "finger" device, described in Sec. 3.4.2, currently holds pure beta emitting ^{90}Sr sources but this will be replaced with a new "finger" containing calibration sources of ^{207}Bi making the full comparison between more relevant and up-to-date set-up. We can also think that implementing the NUCLEIDE++ as a particle generator will certainly create more realistic data as the one presented in this chapter.

- Performing separate tests for each scintillator for both simulations and experiments in a most simplistic setup could help to implement their characteristics in the final simulation. By testing the thin detector and then the thick one separately, we will be capable of determining with better precision the behaviour of each charge contribution.

Finally, even if this study was incomplete does not mean that the detectors are not working properly. Beta can still be detected correctly during online experiments.

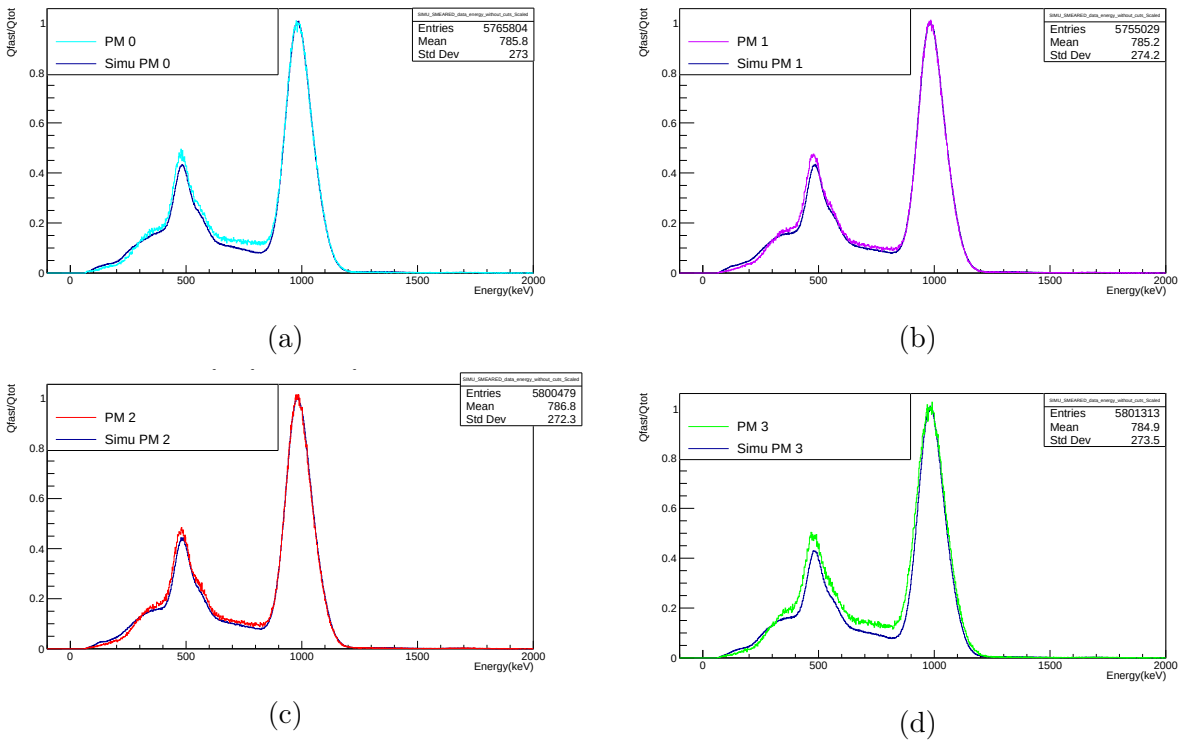

Figure 7.26 – Comparison between experimental and simulated (in blue) spectra with the best settings achieved so far.

Chapter 8

Conclusions and perspectives

In this work, we have presented the results of the commissioning of the MORA set-up. This experiment has been developed to measure the triple correlation parameter D. If this parameter is not null, even though it is theoretically zero according to the Standard Model, it points to a possible time reversal violation, hence maybe new physics. In our case, this measurement is possible thanks to a crown of detection of beta and recoil ions with each kind of detector placed alternatively every 45°. These detectors are placed perpendicular to the 3D trap assuring the maximal correlation between the spin of the nuclei and the different momenta (i.e. beta particles and recoil ions).

The MORA set-up has been first tested at LPC Caen with an offline surface ionisation source using ^{23}Na. This source was also contaminated with potassium and rubidium. However, the different time of flight due to their respective masses could be easily sorted thanks to the massive slow-down process of the PDT2 device. Thanks to SIMION simulations, we could successfully trap ions during 60 µs and later, optimise the trapping efficiency up to 60%.

We have also commissioned the experiment at the IGISOL experimental area where the MORA set-up is meant to stay during the time needed for the construction of the upcoming DESIR facility. A laser ablation, a surface ionisation and a spark source have been used in order to test the setup in final conditions before running online beams. Only the spark source has given valuable results such as a 20% trapping efficiency and, contrary to the other sources, was placed directly at the target location. This source has been reliable at each beam time to recalibrate the injection line and trap.
In total three online experiments[1] have been performed during this thesis. Each beam time has led to different results in terms of efficiencies on both line and trapping leading to 10% of transport efficiency from the mini-buncher to the trap and value ranging from 5 to 50% for the trapping efficiency according to the MCP2 detector.

Finally, the MORA trap has worked perfectly and we were able to trap without losing many ions during 2 s. We have also extended the trapping duration to 11 s which corresponds to the half-life of ^{23}Mg. Regarding all the results, we can surely say that the experimental setup is ready to be used and we are hoping to be able to accumulate enough statistics to first probe any signal indicating a polarisation of the cloud.

[1] Actually four but I have not contributed to the last one.

We, then, have analysed the first exploitable data of the MORA experiment looking for the polarisation degree P of the cloud. This can be only possible after the removal of two different backgrounds polluting the data: the radioactive and the environmental ones. This has been done by using fits and reconstructing histograms using the results coming from the fits. The polarisation has then been calculated and we have ended up with the conclusion that, as shown during the online experiments, the beam was too highly contaminated with ^{23}Na. Indeed, a level of 20000:1 to 1000:1 (^{23}Na:^{23}Mg) could be observed for each beam time. This involves the fact that the cloud contained only a dozen of ^{23}Mg per bunch making the polarisation degree compatible with zero.

Last but not least, we have also presented a first study of the phoswich detectors. Working with an energy resolution of around 13% for $\sim$ 1MeV electron, they are especially efficient in discriminating *beta* particle from *gammas*. Calibration has been made in a non-straightforward way due to the correlation between collected charges. This correlation impacts the 2D spectrum by tilting the events and this has to be fixed. In order to go further, GEANT4 simulations have been conducted in order to have a better knowledge of the detector properties. Since the scintillation-light emission and propagation are not simulated, a smearing parameter has to be set to be able to compare *in fine* the experimental data with simulations. Some work is still necessary since the performed simulations do not properly reproduce the experimental data. This further analysis in the actual chamber of the MORA experiment will be possible thanks to the installation of a ^{207}Bi source on the off-line finger. Thus, one way to improve the study of the detectors would be, once the calibration source is installed, to run simulations to compare them.
Despite this partially unknown difference between the simulation and the experiment, the phoswich detectors are working correctly.

The ^{23}Na is the main problem with the current set-up of MORA, and that is why a technical beam time was scheduled last June 2023. In total, four ion sources have been tested with different parameters such as a coating of BaO in order to avoid the potential sodium trapped in surface and in volume in the source, escaping and contaminating the beam. If no improvement seems to have been shown, an interesting technique using SF_6 gas to create MgF molecule is promising and will be tested in 2024. Another way to decrease the contamination level is to use an MR-TOF-MS coupled with a rebuncher before the MORA injection line. This device was tested in May 2022 without a rebuncher and it showed an almost 100% efficiency. Hence, this last option could be used if the molecular solution is proving to be not successful. It would, however, be very expensive in time and cost since developing such a device would be a matter of months. Finally, another target made of ultra-pure aluminium can be placed instead of our ^{24}Mg making the following reaction ^{27}Al(^{3}He^{7}Li)^{23}Mg. A test with this target is scheduled for February 2024.

Chapter 9

Annex

9.0.1 Gauge symmetries

This concept represents the fact that the Lagrangian of a system, i.e. the dynamic of it, is invariant under specific transformations, which are called gauge transformations. The fact that the system is invariant under such transformation is called gauge invariance. The example and reasoning come from a lecture given by L. Hayen at Notre Dame in 2022. Lie group theory enables to describe these transformations and invariances.

Lie groups:
A group G is a mathematical tool which contains elements g with an operation that satisfies the following constraints

- There must be an identity e
- Each element has an inverse
- The operation is associative, meaning $a * (b * c) = (a * b) * c$ for the $*$ operation

Elements of the group can be represented by a $n \times n$ matrix, such as $\mathrm{M(g_1)M(g_2) = M(g_1g_2)}$. This involves the creation of one matrix for each element of the group which leads rapidly to an infinite amount of matrices. To avoid this problem, Sophus Lie has developed a model which simplifies the process [Lie70]. To illustrate that, let's consider a rotation made of N rotations with an infinitesimal angle θ:

$$R(\theta) = \left(R\left(\frac{\theta}{N}\right)\right)^N . \tag{9.1}$$

When N tends to infinity, it becomes:

$$R\left(\frac{\theta}{N}\right) \longrightarrow 1 + A(\theta) + \mathcal{O}(\theta^2) \tag{9.2}$$

with $A(\theta)$, the contribution of the theta angle at the first-order and $\mathcal{O}(\theta^2)$ the contribution at the second order. This expression is almost equal to 1 since, with N tending to infinity, this rotation is similar of doing nothing.

Furthermore, since the rotation does preserve the translation, it gives, in first order, the following relation:

$$\begin{aligned} a^T b &= a^T R^T R b \\ R^T R &\approx 1 + A(\theta) + A^T(\theta) \end{aligned} \tag{9.3}$$

This implies that A has to be anti-symmetric, meaning A can be expressed as:

$$\begin{aligned} A &= \frac{\theta}{N}\alpha \\ \text{with} \qquad \alpha &= \begin{pmatrix} 0 & 1 \\ -1 & 0 \end{pmatrix} \text{an anti-symmetric matrix.} \end{aligned} \tag{9.4}$$

This leads to

$$R(\theta) = \lim_{N\to\infty} \left(1 + \frac{\theta}{N}\alpha\right)^N \tag{9.5}$$

This form is similar to the Fourier development of the exponential function which gives: $R(\theta) = e^{\theta\alpha}$. This simple expression can generate all matrices from one number and 1 only matrix. Of course, this can be expanded to the three-dimensional world as:

$$R(\theta_1, \theta_2, \theta_3) = e^{i\theta^a \alpha^a}, \tag{9.6}$$

where a goes from 1 to 3 to designate three different anti-symmetry generating matrices. However, the rotation in 3D does not commute since rotating on the x-axis and then on the y-axis does not give the same result as rotating from the y-axis first and then on the x-axis. One has then, to introduce a term which will allow that. This term made of generator α^a forms the Lie algebra and is defined as:

$$[\alpha^a, \alpha^b] = i f^{abc} \alpha^c, \tag{9.7}$$

where f^{abc} are defined in chapter 25 of [Sch13] as structure constants. Furthermore, the structure constant can be equal to 0 and in this case, the gauge symmetry is called Abelian and non-Abelian otherwise.
Finally, the notion of Lie algebra and Lie groups are very present in the SM since the Standard Model is made of three Lie groups as the unitary group U(1) describes the QED, the special unitary group SU(2) describes the weak force and, at last, the SU(3) group describes the strong force.

9.1 Commissioning at LPC Caen

The tables below show the optimal values found during the commissioning at LPC Caen.

Positive voltage	*Negative voltage*	*ions/30s*
950 V	-450 V	1093
960 V	-490 V	1100
970 V	-430V	992
980 V	-420 V	1016
1000 V	-400 V	754
1020 V	-380 V	643
940 V	-460 V	1168
920 V	-480 V	1141
910 V	-490 V	1027
900 V	-500 V	917
930 V	-470 V	1072
940 V	-460 V	1133
950 V	-450 V	1151
945 V	**-455 V**	**1174**

Table 9.1 – Optimum found with the last tested combination of PDT2 voltages.

Einzel lens	*ions/30s*
200 V	1411
0 V	1163
100 V	1276
300 V	1126
250 V	**1399**
150 V	1364

(a) Evolution of the number of ions by changing the lens voltage.

PDT1	*ions/30s*
750 V	1385
775 V	1555
800 V	924
770 V	**1705**
765 V	1677
760 V	1630
755 V	1612

(b) Evolution of the number of ions with the PDT1 voltage.

Table 9.2 –

Pulser 0 (ns)	***Pulser 1 (ns)***	***Burst size***	***R3 (µs)***	***Ions/s***
1590	60040	19	88.25	1576
1670	60130	18	88.38	972
1760	59870	17	88.13	575
1430	60050	21	88.30	1203
1360	59020	22	88.07	1402
1500	60000	20	88.25	1594
1300	59770	23	88.02	1201
1250	59950	24	88.2	791
1200	59950	25	88.20	874
1150	59730	26	87.98	929
1110	69870	27	88.12	548
1070	69870	28	88.08	474
1030	59630	29	87.88	529
1000	59000	30	88.15	302
1500	60000	20	88.25	1840

(a) Here the R3 parameter corresponds to the extraction timings which need to be slightly corrected in order to be in phase with the new RF cycle. This correction is found thanks to the oscilloscope. As mentioned in chap. 5, the Pulser 0 corresponds to the half period of the RF, the Pulser 1 corresponds to a total duration of the RF. The burst size is the number of bursts within the Pulser 1 duration.

R4 (V)	***Ions/s***
339	3150
337.5	2274
339	3212
339.9	2941
339.5	3592
340.5	3953
341.5	4368
342.5	4699
343	4739
343.5	4729
344.5	4390
345.5	4040

(b) Evolution of the number of trapped ions with the variation of the R4 voltages. Originally set to $V_{R4} = 310.5$ V, we have found, step by step, a better optimum at 343 V.

Table 9.3 – Optimisation tables of the R3 and R4 electrodes.

PFEIFFER VACUUM

B: Gas Type Dependence

Indication range above 10^{-2} mbar
(Pirani only mode)

Pressure indicated (gauge calibrated for air)

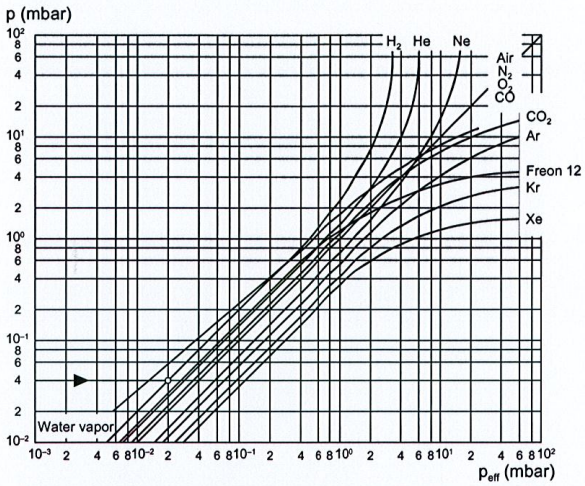

Indication range
10^{-6} ... 0.1 mbar

Pressure indicated (gauge calibrated for air)

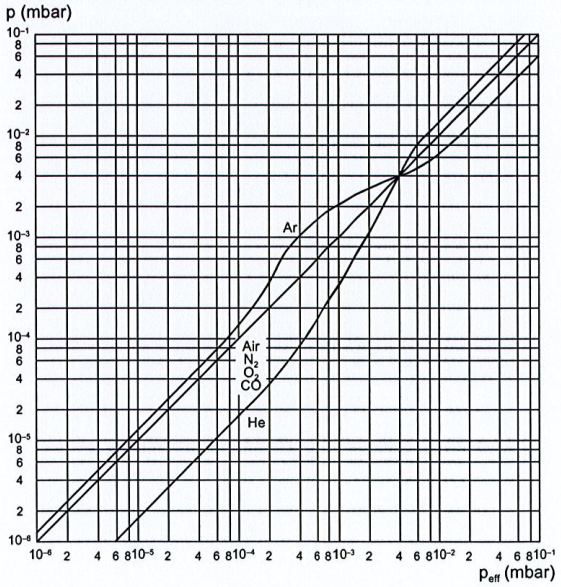

Figure 9.1 – Read pressure versus the effective pressure of the MORA gauges.

9.2 Phoswich

9.2.1 Scintillator characteristics

PROPERTIES	EJ-200	EJ-204	EJ-208	EJ-212
Light Output (% Anthracene)	64	68	60	65
Scintillation Efficiency (photons/1 MeV e^-)	10,000	10,400	9,200	10,000
Wavelength of Maximum Emission (nm)	425	408	435	423
Light Attenuation Length (cm)	380	160	400	250
Rise Time (ns)	0.9	0.7	1.0	0.9
Decay Time (ns)	2.1	1.8	3.3	2.4
Pulse Width, FWHM (ns)	2.5	2.2	4.2	2.7
H Atoms per cm³ ($\times 10^{22}$)	5.17	5.15	5.17	5.17
C Atoms per cm³ ($\times 10^{22}$)	4.69	4.68	4.69	4.69
Electrons per cm³ ($\times 10^{23}$)	3.33	3.33	3.33	3.33
Density (g/cm^3)	1.023	1.023	1.023	1.023
Polymer Base	Polyvinyltoluene			
Refractive Index	1.58			
Softening Point	75°C			
Vapor Pressure	Vacuum-compatible			
Coefficient of Linear Expansion	7.8×10^{-5} below 67°C			
Temperature Range	-20°C to 60°C			
Light Output (L.O.) vs. Temperature	At 60°C, L.O. = 95% of that at 20°C No change from -60°C to 20°C			

Scintillateur mince

PROPERTIES	EJ-240
Light Output (% Anthracene)	41
Scintillation Efficiency (photons/1 MeV e^-)	6,300
Wavelength of Maximum Emission (nm)	430
Light Attenuation Length (cm)	240
Decay Time (ns)	285
H Atoms per cm³ ($\times 10^{22}$)	5.19
C Atoms per cm³ ($\times 10^{22}$)	4.68
Electrons per cm³ ($\times 10^{23}$)	3.33
Density (g/cm^3)	1.023

Polymer Base	Polyvinyltoluene
Refractive Index	1.58
Softening Point	75°C
Vapor Pressure	Vacuum-compatible
Coefficient of Linear Expansion	7.8×10^{-5} below 67°C
Temperature Range	-20°C to 60°C
Light Output (L.O.) vs. Temperature	At 60°C, L.O. = 95% of that at 20°C No change from -60°C to 20°C

Scintillateur épais

Figure 9.2 – Characteristics of the scintillators.

9.2.2 Scintillator thickness

In the following figures, a 0.40 mm thickness is set on the thin scintillator. As always, the

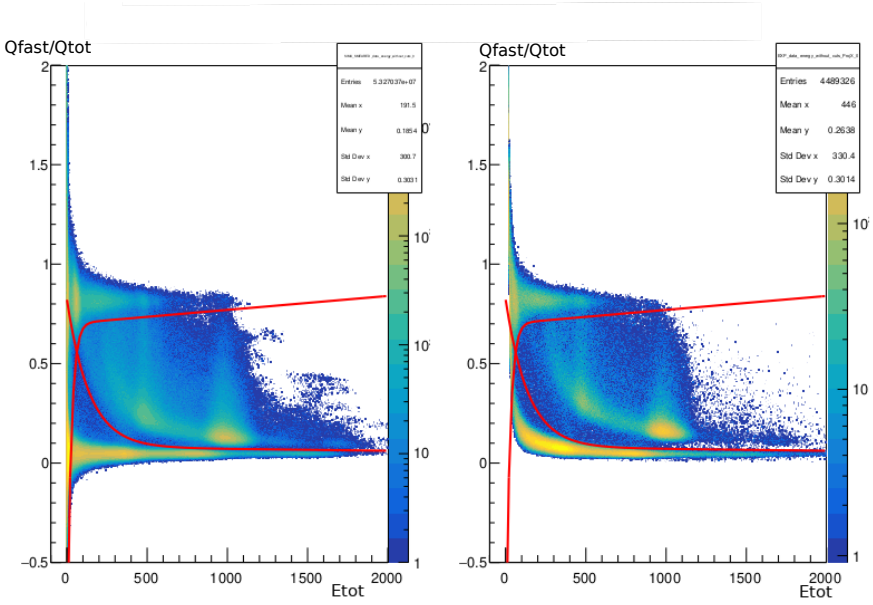

(a) As shown on the 2D histogram, the gamma line is better reproduced since it is spread on the whole x-range like on the experimental spectrum. Moreover, the peak at 1689 keV that was not produced by the GEANT4 default decay event generator is properly simulated by the NUCLEIDE++ file.

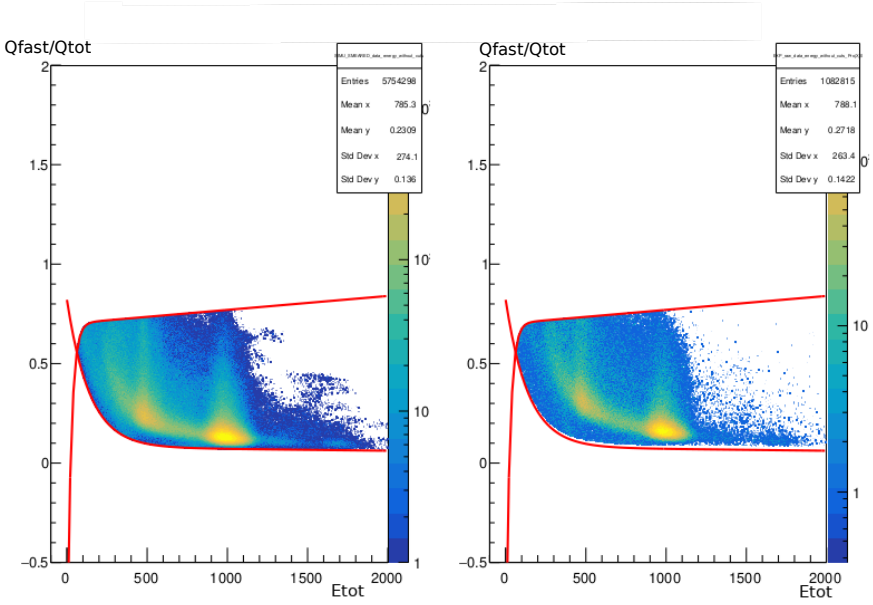

(b) The same plot as Fig. 9.3a on the left after applying the cuts.

Figure 9.3 – Comparison before and after application of the same cuts between simulated data with a thickness of 0.40 mm on the thin scintillator and the experiential spectrum.

9.2.3 Different cuts

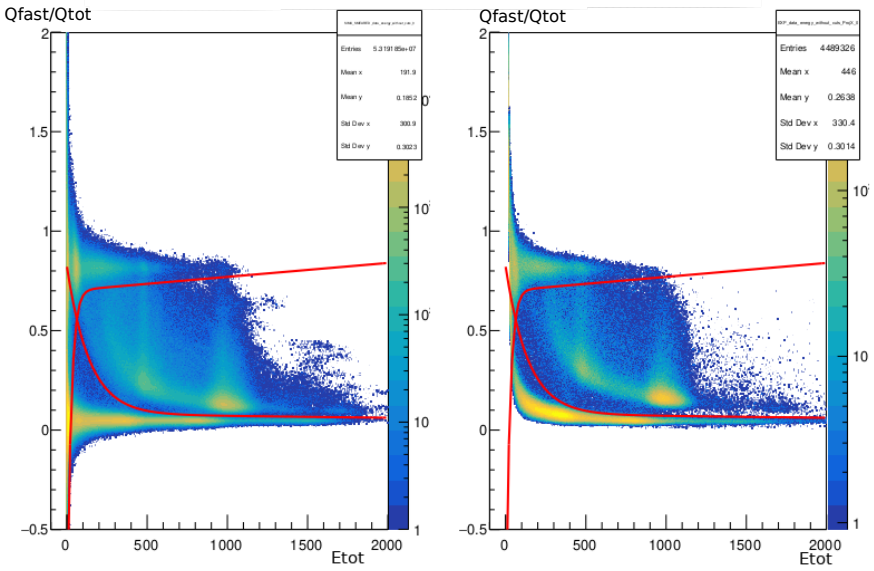

(a)

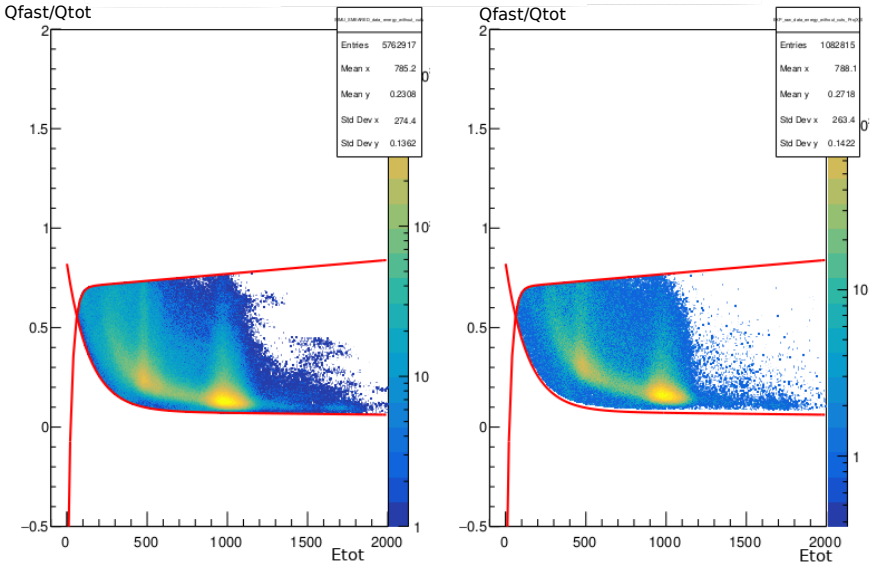

(b)

Figure 9.4 – Comparison before (a) and after application (b) of a more adapted cut between simulated data (NUCLEIDE++) with a thickness of 0.40 mm on the thin scintillator and the experimental spectrum.

9.2.4 Mylar thickness

With 1.5 mylar thickness.

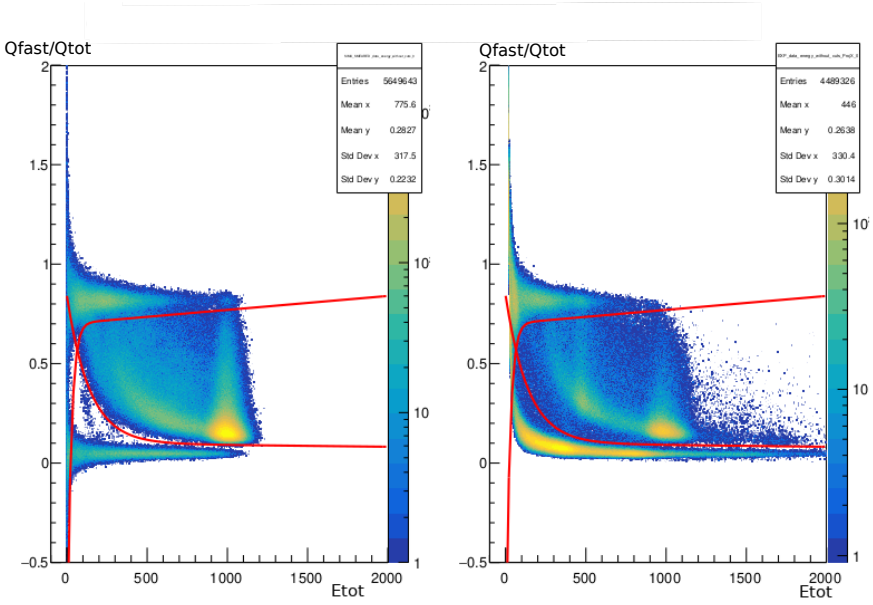

(a) Comparison of the simulated data on the left and the experimental data on the right. The red lines are the cuts that will be applied.

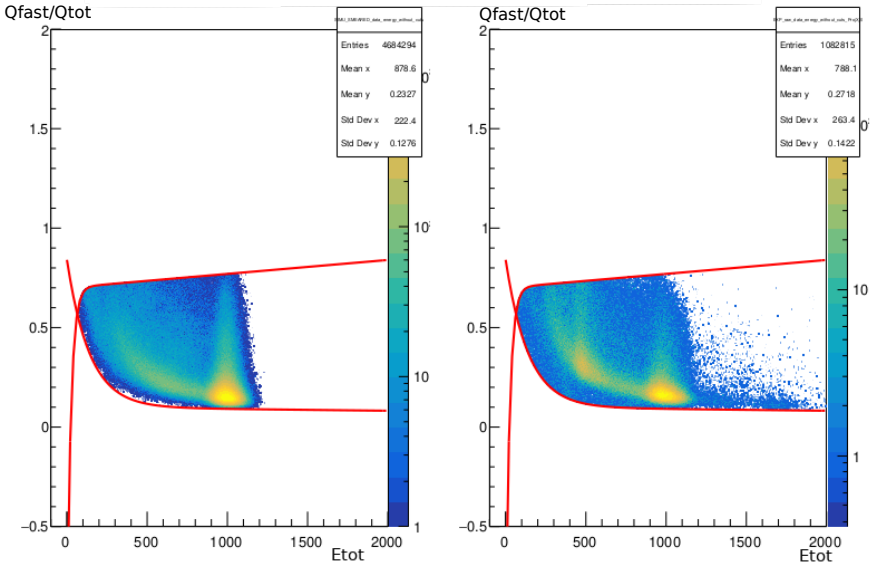

(b) Comparison of the simulated data on the left and the experimental data on the right after the cuts have been applied.

Figure 9.5 – The simulated figures (left panel on both) have been created using of 1.5 µm of Mylar and a thick source support of 1 mm of aluminium.

Bibliography

[Abi+20] B. Abi et al. *Deep Underground Neutrino Experiment (DUNE), Far Detector Technical Design Report, Volume II: DUNE Physics*. 2020. arXiv: 2002.03005 [hep-ex].

[Ago+03] S. Agostinelli et al. "Geant4—a simulation toolkit". In: *Nuclear Instruments and Methods in Physics Research Section A: Accelerators, Spectrometers, Detectors and Associated Equipment* 506.3 (2003), pp. 250–303. ISSN: 0168-9002. DOI: https://doi.org/10.1016/S0168-9002(03)01368-8. URL: https://www.sciencedirect.com/science/article/pii/S0168900203013688.

[Akh+99] E.Kh. Akhmedov et al. "Atmospheric neutrinos at super-Kamiokande and parametric resonance in neutrino oscillations". In: *Nuclear Physics B* 542.1 (1999), pp. 3–30. ISSN: 0550-3213. DOI: https://doi.org/10.1016/S0550-3213(98)00825-6. URL: https://www.sciencedirect.com/science/article/pii/S0550321398008256.

[AIV77] Ennio Arimondo, M Inguscio, and P Violino. "Experimental determinations of the hyperfine structure in the alkali atoms". In: *Reviews of Modern Physics* 49.1 (1977), p. 31.

[Arn+83] G. Arnison et al. "Experimental observation of isolated large transverse energy electrons with associated missing energy at s=540 GeV". In: *Physics Letters B* 122.1 (1983), pp. 103–116. ISSN: 0370-2693. DOI: https://doi.org/10.1016/0370-2693(83)91177-2. URL: https://www.sciencedirect.com/science/article/pii/0370269383911772.

[Ben+20] M. Benali et al. "Geometry optimisation of a transparent axisymmetric ion trap for the MORA project". In: *The European Physical Journal A* 56.6 (June 2020), p. 163. ISSN: 1434-601X. DOI: 10.1140/epja/s10050-020-00168-y. URL: https://doi.org/10.1140/epja/s10050-020-00168-y.

[Ber09] Zurab Berezhiani. "More about neutron–mirror neutron oscillation". In: *The European Physical Journal C* 64.3 (Dec. 2009), pp. 421–431. ISSN: 1434-6052. DOI: 10.1140/epjc/s10052-009-1165-1. URL: https://doi.org/10.1140/epjc/s10052-009-1165-1.

[BJH95] William Ernest Burcham, Melvyn Jobes, and Ernest M Henley. *Nuclear and particle physics*. Longman Burnt Mill, 1995.

[CT67] Curtis G. Callan and S. B. Treiman. "Electromagnetic Simulation of T Violation in Beta Decay". In: *Phys. Rev.* 162 (5 Oct. 1967), pp. 1494–1496. DOI: 10.1103/PhysRev.162.1494. URL: https://link.aps.org/doi/10.1103/PhysRev.162.1494.

[Chr+64] J. H. Christenson et al. "Evidence for the 2π Decay of the K_2^0 Meson". In: *Phys. Rev. Lett.* 13 (4 July 1964), pp. 138–140. DOI: 10.1103/PhysRevLett.13.138. URL: https://link.aps.org/doi/10.1103/PhysRevLett.13.138.

[Cli06] James M Cline. "Baryogenesis". In: *arXiv preprint hep-ph/0609145* (2006).

[Col+] LHCb Collaboration et al. *Observation of particles composed of five quarks, pentaquark-charmonium states, seen in Δ 0 b→ J/ψpK- decays.*

[col20] LHCb collaboration. "Observation of structure in the J/ψ-pair mass spectrum". In: *Science Bulletin* 65.23 (Dec. 2020), pp. 1983–1993. DOI: 10.1016/j.scib.2020.08.032. URL: https://doi.org/10.1016%2Fj.scib.2020.08.032.

[Dav74] H David Politzer. "Asymptotic freedom: An approach to strong interactions". In: *Physics Reports* 14.4 (1974), pp. 129–180. ISSN: 0370-1573. DOI: https://doi.org/10.1016/0370-1573(74)90014-3. URL: https://www.sciencedirect.com/science/article/pii/0370157374900143.

[Deh68] Hans G Dehmelt. "Radiofrequency spectroscopy of stored ions I: Storage". In: *Advances in atomic and molecular physics*. Vol. 3. Elsevier, 1968, pp. 53–72.

[Del+19a] P. Delahaye et al. "The open LPC Paul trap for precision measurements in beta decay". In: *The European Physical Journal A* 55.6 (June 2019), p. 101. ISSN: 1434-601X. DOI: 10.1140/epja/i2019-12777-3. URL: https://doi.org/10.1140/epja/i2019-12777-3.

[Del20] Pierre Delahaye. *Capture, ionisation et piégeage d'isotopes pour la physique fondamentale*. Habilitation à diriger des recherches. Nov. 2020.

[Del+19b] Pierre Delahaye et al. "The MORA project". In: *Hyperfine Interactions* 240 (June 2019). DOI: 10.1007/s10751-019-1611-x.

[Ein22] Albert Einstein. *Die grundlage der allgemeinen relativitätstheorie*. Vol. 49. JA Barth, 1922.

[Fab15] Xavier Fabian. "Precision measurements in the weak interaction framework: development of realistic simulations for the LPCTrap device installed at GANIL". PhD thesis. Université de Caen Normandie, 2015.

[FR22] Adam Falkowski and Antonio Rodríguez-Sánchez. "On the sensitivity of the D parameter to new physics". In: *The European Physical Journal C* 82.12 (Dec. 2022), p. 1134. ISSN: 1434-6052. DOI: 10.1140/epjc/s10052-022-11085-3. URL: https://doi.org/10.1140/epjc/s10052-022-11085-3.

[FER34] ENRICO FERMI. "Radioactivity Induced by Neutron Bombardment". In: *Nature* 133.3368 (May 1934), pp. 757–757. ISSN: 1476-4687. DOI: 10.1038/133757a0. URL: https://doi.org/10.1038/133757a0.

[FG58] R. P. Feynman and M. Gell-Mann. "Theory of the Fermi Interaction". In: *Phys. Rev.* 109 (1 Jan. 1958), pp. 193–198. DOI: 10.1103/PhysRev.109.193. URL: https://link.aps.org/doi/10.1103/PhysRev.109.193.

[FG18] Bartosz Fornal and Benjamin Grinstein. "Dark Matter Interpretation of the Neutron Decay Anomaly". In: *Phys. Rev. Lett.* 120 (19 May 2018), p. 191801. DOI: 10.1103/PhysRevLett.120.191801. URL: https://link.aps.org/doi/10.1103/PhysRevLett.120.191801.

[FGL73] H. Fritzsch, M. Gell-Mann, and H. Leutwyler. "Advantages of the color octet gluon picture". In: *Physics Letters B* 47.4 (1973), pp. 365–368. ISSN: 0370-2693. DOI: https://doi.org/10.1016/0370-2693(73)90625-4. URL: https://www.sciencedirect.com/science/article/pii/0370269373906254.

[Gel64] M. Gell-Mann. "A schematic model of baryons and mesons". In: *Physics Letters* 8.3 (1964), pp. 214–215. ISSN: 0031-9163. DOI: https://doi.org/10.1016/S0031-9163(64)92001-3. URL: https://www.sciencedirect.com/science/article/pii/S0031916364920013.

[GM08] M.C. Gonzalez-Garcia and Michele Maltoni. "Phenomenology with massive neutrinos". In: *Physics Reports* 460.1 (2008), pp. 1–129. ISSN: 0370-1573. DOI: https://doi.org/10.1016/j.physrep.2007.12.004. URL: https://www.sciencedirect.com/science/article/pii/S0370157308000148.

[Goy23] Nishu Goyal. "Detection of beta decay in laser oriented trapped radioactive isotopes for the MORA project". PhD thesis. Université Caen Normandie, 2023. URL: https://www.theses.fr/s227984.

[Hal+84] AL Hallin et al. "Test of Time-Reversal Symmetry in the β Decay of Ne 19". In: *Physical Review Letters* 52.5 (1984), p. 337.

[JTW57] JD Jackson, SB Treiman, and HW Wyld Jr. "Possible tests of time reversal invariance in beta decay". In: *Physical Review* 106.3 (1957), p. 517.

[Jou+23] M. Le Joubioux et al. *Is there a dark decay of neutrons in ^{6}He ?* 2023. arXiv: 2308.16536 [nucl-ex].

[Kuc93] Peter A Kuchment. *Floquet theory for partial differential equations*. Vol. 60. Springer Science & Business Media, 1993.

[LY56] T. D. Lee and C. N. Yang. "Question of Parity Conservation in Weak Interactions". In: *Phys. Rev.* 104 (1 Oct. 1956), pp. 254–258. DOI: 10.1103/PhysRev.104.254. URL: https://link.aps.org/doi/10.1103/PhysRev.104.254.

[Lie70] Sophus Lie. *Theorie der transformationsgruppen*. Vol. 2. P, 1970.

[Lié10] E. Liénard. "Mesures du coefficient de corrélation angulaire B-v dans les transitions B nucléaires". Habilitation à diriger des recherches. Université de Caen, Apr. 2010. URL: https://theses.hal.science/tel-00577620.

[MD68] F. G. Major and H. G. Dehmelt. "Exchange-Collision Technique for the rf Spectroscopy of Stored Ions". In: *Phys. Rev.* 170.1 (June 1968). Publisher: American Physical Society, pp. 91–107. DOI: 10.1103/PhysRev.170.91. URL: https://link.aps.org/doi/10.1103/PhysRev.170.91.

[MGW05] Fouad G Major, Viorica N Gheorghe, and Günther Werth. *Charged particle traps: physics and techniques of charged particle field confinement*. Vol. 37. Springer Science & Business Media, 2005.

[MM06] Ettore Majorana and Luciano Maiani. "A symmetric theory of electrons and positrons". In: *Ettore Majorana Scientific Papers: On occasion of the centenary of his birth*. Ed. by Giuseppe Franco Bassani. Berlin, Heidelberg: Springer Berlin Heidelberg, 2006, pp. 201–233. ISBN: 978-3-540-48095-2. DOI: 10.1007/978-3-540-48095-2_10. URL: https://doi.org/10.1007/978-3-540-48095-2_10.

[MT89] E Mathieu and E Tournier. "Course de physique mathématique, Paris, 1873". In: (1989).

[Mer07] Alain Mery. "Mesure du coefficient de correlation angulaire beta-neutrino dans la decroissance de l'^{6}He à l'aide d'un piege de Paul". PhD thesis. Universite de Caen, 2007.

[MV99] Harold J Metcalf and Peter Van der Straten. *Laser cooling and trapping*. Springer Science & Business Media, 1999.

[MDÄ14] I. D. Moore, P. Dendooven, and J. Ärje. "The IGISOL technique—three decades of developments". In: *Hyperfine Interactions* 223.1 (Jan. 2014), pp. 17–62. ISSN: 1572-9540. DOI: 10.1007/s10751-013-0871-0. URL: https://doi.org/10.1007/s10751-013-0871-0.

[Mui65] H. (Hugh) Muirhead. *The physics of elementary particles*. [First edition]. Oxford ; New York : Pergamon Press, [1965] [©1965], 1965. URL: https://search.library.wisc.edu/catalog/999634258202121.

[Mum+04] H. P. Mumm et al. "emiT: An apparatus to test time reversal invariance in polarized neutron decay". In: *Review of Scientific Instruments* 75.12 (Dec. 2004). Publisher: AIP Publishing, pp. 5343–5355. DOI: 10.1063/1.1821628. URL: https://doi.org/10.1063%2F1.1821628.

[Noe71] Emmy Noether. "Invariant variation problems". In: *Transport Theory and Statistical Physics* 1.3 (Jan. 1971), pp. 186–207. DOI: 10.1080/00411457108231446. URL: https://doi.org/10.1080%2F00411457108231446.

[POF58] Wolfgang Paul, Otto Osberghaus, and Erhardt Fischer. "Versuchsanordnung". In: *Ein Ionenkäfig*. Wiesbaden: VS Verlag für Sozialwissenschaften, 1958, pp. 25–29. ISBN: 978-3-663-04689-9. DOI: 10.1007/978-3-663-04689-9_3. URL: https://doi.org/10.1007/978-3-663-04689-9_3.

[PS53] Wolfgang Paul and Helmut Steinwedel. "Ein neues massenspektrometer ohne magnetfeld". In: *Zeitschrift für Naturforschung A* 8.7 (1953), pp. 448–450.

[Ret21] Blaise-Mael Retailleau. "PILGRIM : un spectromètre de masse par temps de vol pour S3, et brisure de symétrie d'isopin dans le 38K". Theses. Normandie Université, Feb. 2021. URL: https://theses.hal.science/tel-03259311.

[Sak91] AD Sakharov. "Violation of CP invariance, C asymmetry, and baryon asymmetry of the universe". In: *Usp. Fiz. Nauk* 161 (1991), pp. 61–64.

[SGW79] A Salam, SL Glashow, and S Weinberg. "Nobel lectures (1979)". In: *Reprinted as ICTP Preprint* (1979).

[Sch13] Matthew D. Schwartz. *Quantum Field Theory and the Standard Model*. Cambridge University Press, 2013. DOI: 10.1017/9781139540940.

[Sch51] Julian Schwinger. "The Theory of Quantized Fields. I". In: *Phys. Rev.* 82 (6 June 1951), pp. 914–927. DOI: 10.1103/PhysRev.82.914. URL: https://link.aps.org/doi/10.1103/PhysRev.82.914.

[Sev+23] N. Severijns et al. "$\mathcal{F}t$ values of the mirror β transitions and the weak-magnetism-induced current in allowed nuclear β decay". In: *Phys. Rev. C* 107 (1 Jan. 2023), p. 015502. DOI: 10.1103/PhysRevC.107.015502. URL: https://link.aps.org/doi/10.1103/PhysRevC.107.015502.

[Sev04] Nathal Severijns. *Weak Interaction Studies by Precision Experiments in Nuclear Beta Decay*. Ed. by Jim Al-Khalili and Ernst Roeckl. Berlin, Heidelberg: Springer Berlin Heidelberg, 2004, pp. 339–381. ISBN: 978-3-540-44490-9. DOI: 10.1007/978-3-540-44490-9_10. URL: https://doi.org/10.1007/978-3-540-44490-9_10.

[Sol+04] T Soldner et al. "New limit on T violation in neutron decay". In: *Physics Letters B* 581.1 (2004), pp. 49–55. ISSN: 0370-2693. DOI: https://doi.org/10.1016/j.physletb.2003.12.004. URL: https://www.sciencedirect.com/science/article/pii/S0370269303018586.

[Thi+20] C. Thiam et al. "Nuclide++: A C++ module to include DDEP recommended radioactive decay Data in Geant4". In: *Applied Radiation and Isotopes* 156 (2020), p. 108964. ISSN: 0969-8043. DOI: https://doi.org/10.1016/j.apradiso.2019.108964. URL: https://www.sciencedirect.com/science/article/pii/S0969804319303574.

[Wan+12] M. Wang et al. "The AME2012 atomic mass evaluation (II). Tables, graphs and references". In: *Chin.Phys.C* 36 (2012), p. 1603.

[Wig32] E. Wigner. "On the Quantum Correction For Thermodynamic Equilibrium". In: *Phys. Rev.* 40 (5 June 1932), pp. 749–759. DOI: 10.1103/PhysRev.40.749. URL: https://link.aps.org/doi/10.1103/PhysRev.40.749.

[Wika] Wikipedia. URL: https://en.wikipedia.org/wiki/Finite%5C_element%5C_method.

[Wikb] Wikipedia. URL: https://en.wikipedia.org/wiki/Finite%5C_difference%5C_method.

[Wikc] Wikipedia. URL: https://en.wikipedia.org/wiki/Boundary%5C_element%5C_method.

[Wikd] Wikipedia. URL: https://www.nndc.bnl.gov/nudat3/DecayRadiationServlet?nuc=207Bi&unc=NDS.

[Wu+57] Chien-Shiung Wu et al. "Experimental test of parity conservation in beta decay". In: *Physical review* 105.4 (1957), p. 1413.

[WSL04] R. F. Wuerker, H. Shelton, and R. V. Langmuir. "Electrodynamic Containment of Charged Particles". In: *Journal of Applied Physics* 30.3 (June 2004). _eprint: https://pubs.aip.org/aip/jap/article-pdf/30/3/342/7926269/342_1_online.pdf, pp. 342–349. ISSN: 0021-8979. DOI: 10.1063/1.1735165. URL: https://doi.org/10.1063/1.1735165.

[Zee97] Dr. P. Zeeman. “XXXII. On the influence of magnetism on the nature of the light emitted by a substance”. In: *The London, Edinburgh, and Dublin Philosophical Magazine and Journal of Science* 43.262 (1897), pp. 226–239. DOI: 10.1080/14786449708620985. eprint: https://doi.org/10.1080/14786449708620985. URL: https://doi.org/10.1080/14786449708620985.

À la recherche de violation de symétrie CP avec MORA: mise en service du dispositif expérimental et premières expériences.

Résumé:

Cette thèse s'inscrit dans la recherche d'évènement impliquant une violation de symétrie CP. Pour ce faire, on s'intéresse au paramètre de corrélation triple D défini dans le Modèle Standard comme étant nul. D est corrélé au spin du noyau père ainsi qu'aux différentes impulsions des produits de désintégration beta. Une orientation du spin des noyaux pères est nécessaire pour accéder à ce paramètre. Le dispositif MORA est une expérience de piégeage maximisant ainsi cette polarisation. La majeure partie de ce travail de thèse consiste en l'étude du dispositif expérimental et de sa mise en service à l'aide de source d'ions stables. Des simulations SIMION ont été réalisées afin de faciliter la réussite du piégeage des ions. Une mise en service a également été réalisée au sein du hall expérimental du département de physique de l'université de Jyväskylä, là où l'expérience est installée actuellement. Quatre temps de faisceau de ^{23}Mg ont permis d'affiner les performances du dispositif les premières données exploitables de MORA. Les premières données acquises en novembre 2022 ont été analysées mais le degrée de polarisation du nuage n'a pas pu être déterminé en raison d'une trop grande contamination en ^{23}Na. Enfin, ce travail se conclut dans la troisième partie de ce document, par la caractérisation et la calibration des détecteurs β. Après une première calibration expérimentale, une tentative d'amélioration de celle-ci à l'aide de simulations GEANT4 a été menée mais des différences subsistent entre les spectres expérimentaux et simulés. Diverses pistes ont été alors explorées mais bien que prometteuses, elles n'ont pas encore permis de comprendre totalement les différences observées.

Search for CP violation with MORA: Commissioning of the setup and first experiments.

Abstract:

This thesis is part of the search for events involving CP violation. To this end, we are interested in the triple correlation parameter D defined in the Standard Model as zero. D is correlated to the spin of the parent nucleus and to the different momenta of the beta decay products. Spin orientation of the parent nuclei is required to access this parameter. The MORA device is a trapping experiment that maximises this polarisation. The major part of this thesis work consists of studying the experimental setup and its commissioning using a stable ion sources. Simulations were carried out to facilitate successful ion trapping. Commissioning was also carried out in the experimental hall of the physics department at the University of Jyväskylä, where the experiment currently resides. Four ^{23}Mg beam times were used to fine-tune the device, enabling the first usable MORA data to be taken. These first data were analysed but the polarisation degree could not be determined due to a too large contamination of the beam in stable ^{23}Na. Finally, the work concludes in the third part of this document with characterising and calibrating the β detectors. After an experimental calibration, an attempt was made to improve the latter using GEANT4 simulations, but differences remain between the experimental and simulated spectra. Various avenues have therefore been explored but, even if promising, they have not yet allowed a full understanding of these differences.

Mot-clés: Beta decay, CP violation, Ion trap, Simulations, Calibrations, Analysis, Standard Model, Symmetries, Polarisation